UNIVERSITY OF SPLIT

FACULTY OF ELECTRICAL ENGINEERING, MECHANICAL ENGINEERING AND NAVAL ARCHITECTURE

SVEUČILIŠTE U SPLITU

FAKULTET ELEKTROTEHNIKE, STROJARSTVA I BRODOGRADNJE

Željko Penga

COOLANT INDUCED VARIABLE TEMPERATURE FLOW FIELD FOR IMPROVED PERFORMANCE OF PROTON EXCHANGE MEMBRANE FUEL CELLS

POBOLJŠANJE RADNIH ZNAČAJKI MEMBRANSKIH GORIVNIH ČLANAKA INDUCIRANJEM VARIJABILNOG TEMPERATURNOG POLJA RASHLADNIM SREDSTVOM

DOCTORAL THESIS

DOKTORSKA DISERTACIJA

Split, 2017.

The research reported in this thesis was carried out at Department of Mechanical Engineering and Naval Architecture, University of Split, Faculty of Electrical Engineering, Mechanical Engineering and Naval Architecture.

Supervisor: prof. dr. sc. Frano Barbir, FESB, University of Split, Croatia

Thesis No.

Committee for assessment of doctoral dissertation:

1. prof. dr. sc. Gojmir Radica – president of the commitee, FESB, Split
2. prof. dr. sc. Branko Klarin – member, FESB, Split
3. assoc. prof. dr. sc. Zoran Milas – member, FESB, Split
4. assoc. prof. dr. sc. Sandro Nižetić – member, FESB, Split
5. assist. prof. dr. sc. Tea Žakula – member, FSB, Zagreb

Committee for defence of doctoral dissertation:

1. prof. dr. sc. Gojmir Radica – president, FESB, Split
2. prof. dr. sc. Branko Klarin – member, FESB, Split
3. assoc. prof. dr. sc. Zoran Milas – member, FESB, Split
4. assoc. prof. dr. sc. Sandro Nižetić – member, FESB, Split
5. assist. prof. dr. sc. Tea Žakula, – member, FSB, Zagreb

Dissertation defended on:

COOLANT INDUCED VARIABLE TEMPERATURE FLOW FIELD FOR IMPROVED PERFORMANCE OF PROTON EXCHANGE MEMBRANE FUEL CELLS

Abstract:

Proton exchange membrane (PEM) fuel cell efficiency is dependent on water and heat management of the cell. In order to achieve high performance, the membrane hydration must be high. Common practice of maintaining isothermal temperature profile along the flow field of the cell requires external humidification in order to achieve high membrane water content.

This thesis presents the concept of the variable temperature flow field for high performance PEM fuel cell operation without the requirement for external humidification. Internally generated water and heat are used for maintaining relative humidity of the reactants close to 100% along the entire flow field. The desired temperature profile is achieved by gradually increasing the temperature of the coolant during the passage through the PEM fuel cell. The concept is applicable for PEM fuel cell stacks for the first time.

Computational fluid dynamics models of a single cell and five-cell stack were developed in order to investigate the concept. The models were calibrated and thoroughly validated on the newly developed experimental setup with very high level of agreement in all aspects. The results have shown that the PEM fuel cell operated with dry reactants, with applied variable temperature flow field concept, shows superior performance when compared to conventional fully humidified isothermal operation.

Keywords:

PEM fuel cell; Computational Fluid Dynamics; Segmented PEM fuel cell; Variable temperature flow field

POBOLJŠANJE RADNIH ZNAČAJKI MEMBRANSKIH GORIVNIH ČLANAKA INDUCIRANJEM VARIJABILNOG TEMPERATURNOG POLJA RASHLADNIM SREDSTVOM

Sažetak:

Radne značajke membranskih (PEM) gorivnih članaka ovise o upravljanju vodom i toplinom. U svrhu ostvarivanja visoke učinkovitosti, sadržaj vode u membrane tijekom rada treba biti visok. Uobičajeni način rada pri izotermalnim graničnim uvjetima duž čitavog polja strujanja zahtijeva korištenje vanjskih ovlaživača kako bi se mogla ostvariti visoka učinkovitost.

U ovoj disertaciji predstavljen je koncept varijabilnog temperaturnog polja u svrhu ostvarivanja visoke radne učinkovitosti membranskih gorivnih članaka bez potrebe za korištenjem vanjskih ovlaživača. Korištenjem vode i topline, proizvedenih tijekom rada gorivnog članka, moguće je ostvariti relativnu vlažnost u blizini 100% duž čitavog polja strujanja. Željeni temperaturni profil moguće je ostvariti postupnim dogrijavanjem rashladnog sredstva prolaskom kroz membranski gorivni članak. Rezultat istraživanja je koncept primjenjiv na svežanj gorivnih članaka po prvi put.

Primjenom računalnog modeliranja strujanja, razvijeni su modeli jediničnog gorivnog članka i svežnja sačinjenog od pet jediničnih članaka u svrhu istraživanja koncepta varijabilnog temperaturnog polja. Razvijeni modeli su kalibrirani i validirani sa rezultatima mjerenja na novoj eksperimentalnoj instalaciji, pri čemu je ostvarena visoka razina međusobne usklađenosti rezultata. Rezultati istraživanja pokazali su po prvi put da je moguće ostvariti veću radnu učinkovitost primjenom koncepta varijabilnog temperaturnog polja s potpuno suhim reaktantima spram konvencionalnog izotermalnog načina rada s potpuno ovlaženim reaktantima.

Ključne riječi:

PEM gorivni članak; Računalno modeliranje strujanja; Segmentirani PEM gorivni članak; Varijabilno temperaturno polje

Ovaj rad posvećujem svojoj Obitelji.

TABLE OF CONTENTS

LIST OF TABLES

LIST OF FIGURES

xiv

LIST OF SYMBOLS

General symbols

a – water activity

CFD – Computational fluid dynamics

c_r – condensation rate constant, s^{-1}

c_w – specific heat of water, $\text{J kg}^{-1}\text{K}^{-1}$

D_i – gas phase species diffusivity, m^2s^{-1}

D_l – membrane water diffusivity

D_i^0 – species mass diffusivity, m^2s^{-1}

D_{eff}^{ij} – effective gas species diffusivity, m^2s^{-1}

e – electron

F – Faraday constant, C kmol^{-1}

g – gravitational acceleration, m s^{-2}

GDL – gas-diffusion layer

H – hydrogen

h – enthalpy, J

h_L – source term for enthalpy of water phase change, W m^{-3}

h_{react} – electrochemical heat source, W m^{-3}

I – electrical current, A

I_{leak} – leakage current, A

ISO – isothermal

J_w^{diff} – back diffusion flux, kg m^{-3} s^{-1}

j^{ref} – exchange current density per active surface area, A m^{-2}

K – absolute permeability

k^{eff} – thermal conductivity, W m^{-1} K^{-1}

M_m – equivalent weight of the dry membrane, g mol^{-1}

M_i – molar mass of species, g mol^{-1}

MEA – membrane electrode assembly

MPL – micro-porous layer

$\dot{m}$ – mass flow rate, kgs^{-1}

n_d – electro-osmotic drag coefficient

O – oxygen

p – pressure/local pressure, N m^{-2}

PEM – proton exchange membrane

p_c – capillary pressure, N m^{-2}

p_{sat} – water vapor saturation pressure, N m^{-2}

p_{wv} – partial pressure of water vapor, N m^{-2}

PID – proportional-integral-derivative

$\dot{Q}$ – heat flux, W

R – gas constant, K^{-1} mol^{-1}

$R_{\text{an/cat}}$ – overpotential anode, cathode, V; exchange current density anode/cathode, A m^{-3}

$R_{\text{sol/mem}}$ – volumetric transfer current of solid phase/membrane, A m^{-3}

R_{ohm} – ohmic resistance, Ω

RH – relative humidity

RH&T – relative humidity and temperature

r_w – condensation rate, kg m^{-3} s^{-1}

r_s – pore blockage exponent

s – liquid saturation

S_h - source term for heat, W m^{-3}

S_i – species source/sink term, kg m^{-3} s^{-1}

S_{mass} – source term for continuity equation, kg m^{-3} s^{-1}

S_{mom} – source term for momentum equation, kg m^{-3} s^{-1}

S_T – source term for energy equation, W m^{-3}

SHT21 – relative humidity sensor Sensirion

T – temperature, K

TC – thermocouple

V – volume, m^3; electric potential, V

Vol – volume, m^3

VTFF – variable temperature flow field

$\vec{V}$ – velocity vector, m s^{-1}

$\vec{v}$ – velocity vector, m s^{-1}

x – water vapor mass fraction

X_i – species mass fraction

[ ] – local species concentration, kmol m^{-3}

Greek symbols

α – transfer coefficient

β – electrolyte electrical conductivity generalization constant

γ – concentration dependency coefficient; function exponent

Δ – difference

ε – porosity

ζ – specific active surface area, m^2

η – local overpotential, V

$\eta_{an,cat}$ – transition current anode, cathode, $A\ m^{-3}$

θ – contact angle, $°$

λ – membrane water content

μ – dynamic viscosity, $kg\ m^{-1}\ s^{-1}$

ρ – density, $kg\ m^{-3}$

ρ_m – dry membrane density, $kg\ m^{-3}$

σ – electrical conductivity, $\Omega^{-1}\ s^{-1}$; surface tension, $N\ m^{-1}$

ϕ – electric potential, V

ω – absolute humidity, $kg_{H_2O}\ kg_{air}^{-1}$; electrolyte electrical conductivity generalization constant

Mathematical symbols

∂ – partial derivative

∇ – nabla operator

General indexes

an - anode

cat – cathode

i - specie

l – liquid water

p - pressure

ref – reference value

t - temperature

0 – reference value

$(+)$ – positive charge

$(-)$ – negative charge

1   INTRODUCTION

Proton exchange membrane (PEM) fuel cells have gained a lot of attention in the recent years due to their favorable characteristics – simple design, high efficiency, low temperature, environmentally friendly operation due to virtually zero CO_2 emission and the absence of the moving components [1-6]. They are also characterized by a wide range of applications, from primary and auxiliary stationary applications to dynamic applications in road, sea and air vehicles.

However, the commonly used PEM fuel cell system is quite complex. The necessity for external temperature control of the cell via coolant loops and heat exchangers, and the requirement for the relative humidity control of the reactants upon entry to the cell, results in high price and maintenance requirements for the system. The consequences are the requirement for an incubator-like setup for high efficiency PEM fuel cell system operation and limited operating range of the cell.

Limited operating range of PEM fuel cell system is a result of the requirement for external humidifiers. Since the ionomer membrane ionic conductivity is very sensitive to the net water transport through the membrane, i.e. to the water content of the membrane, the reactants are required to be characterized by high relative humidity upon entering the cell in order to achieve highly efficient operation.

The idea of removing the external humidifiers is not new. However, there are only a few commercial manufacturers who have managed to remove the external humidifiers with satisfactory level of performance, while the most advanced automotive fuel cell system without external humidification is currently commercially produced by Toyota [7]. However, Toyota PEM fuel cell stack system requires hydrogen recirculation pump for highly efficient operation, which is also a costly component and has a function similar to the external humidifier, i.e. it recirculates the humidified hydrogen stream from the anode outlet back to the anode inlet to the cell. Therefore it can be concluded that complete removal of external humidification without compromising the high efficiency has not yet been achieved.

There are only a few papers in the literature on this topic, this research of this thesis is rooted on previous studies of Tolj et al. [8], but expands the mentioned work in meanings

of studying different heat management strategies, since the mentioned work was based mostly on studying the water management and the temperature profiles along the cathode side of the cell. The external humidification in the mentioned work is removed, the hydrogen enters the cell dry, while the air has ambient temperature and relative humidity, and the performance of the cell is kept at a high level by prescribing the variable temperature flow field. The idea behind the mentioned, experimentally validated concept, is that the relative humidity of gas is a temperature dependent parameter, and by manipulating the temperature profile across the entire flow field of the cell, it is possible to impose such temperature profile which will result in close to 100% relative humidity along the entire cell for the specified amount of produced water inside the operating cell. However, the variable temperature flow field in the mentioned study is established and maintained by Peltier thermoelements, and it is only applicable for a single cell with simple flow field design, i.e. straight reactant channels. This work investigates the possibility of establishing the variable temperature flow field by other means, applicable on a PEM fuel cell stack system level.

Useful tool for PEM fuel cell analysis which gains more popularity in recent years is computational fluid dynamics (CFD). The CFD modeling enables generation of a virtual model of PEM fuel cell with the capability of including all of different complex physical processes inside an operating cell. Until recently, CFD modeling was only possible on super-computers. However, since the personal computers are quite advanced today, CFD modeling has become available to broad number of users. Once developed and validated, the CFD model can be used for different what-if scenarios, and give a detailed insight in multi-physical processes inside an operating cell. However, since the models are based on experimentally derived expressions for different PEM fuel cell setups, and the experimental results of different authors show high degree of discrepancies, every CFD model must be thoroughly experimentally calibrated and validated.

This thesis investigates the literature recommendations for developing a CFD model which will enable the study of PEM fuel cell performance under different operating conditions. The goal of the CFD analysis is to develop a credible, experimentally validated, robust numerical model where the desired temperature flow field will be established by a coolant fluid. The idea is to use internally generated heat to gradually increase the temperature of

the coolant in the downstream direction in respect to the cell entry. The resulting temperature profile should closely resemble the desired temperature profile, i.e. water vapor saturation temperature profile, and the concept should be applicable for a PEM fuel cell stacks. If such concept proves feasible, it will be the first of its kind, since no one up to date has been able to achieve highly efficient PEM fuel cell operation without external humidification.

2   PROTON EXCHANGE MEMBRANE FUEL CELL

Proton exchange membrane fuel cell is an electrochemical energy conversion device for converting the chemical energy of the reactants to electrical energy. It provides direct and continuous power output as long as the reactants are provided, and produces direct electrical current, with only byproducts being water and heat. The fuel required for PEM fuel cell operation is hydrogen, in pure or in a reformate form, and the oxidizer is pure oxygen or, more commonly, ambient air. The PEM fuel cell system does not have moving components, and there is no combustion. The electrochemical process inside PEM fuel cell is basically a reversed electrolysis of water, and, to a certain extent, similar to the process of galvanostatic electrochemical cell, i.e. battery, since it produces direct current electricity and consists of the anode and cathode with the electrolyte in between. The difference between galvanostatic cell and fuel cell is in the necessity of the fuel cell for constant reactant supply, therefore the fuel cell cannot be depleted, and the electrodes are not prone to rapid changes in chemical composition.

There are different types of fuel cells, named after the type of the electrolyte, or fuel, required for operation. There are alkaline, phosphoric acid, molten carbonate, solid oxide, polymer electrolyte or proton exchange membrane and direct methanol fuel cells. The main advantage of PEM when compared to other types of fuel cells is relatively low operating temperature (usually between 60°C and 80°C), high efficiency and the absence of aggressive chemical byproducts during operation.

2.1   Components

The PEM fuel cell components and their functions are:

Polymer electrolyte or proton exchange membrane (perfluorosulfonated acid polymer, with the most commonly used from the international manufacturer DuPont under the name Nafion) is a ionomer membrane. This type of membrane allows free passage of cations, in PEM fuel cell case the hydrogen protons, but disables the passage of the gas molecules and electrons, hence the name proton exchange membrane.

Catalyst layer is a carbon supported structure coated with platinum nano-particles, it enhances the rate of the electrochemical reactions, without (intentional) change in

composition over time. The catalyst layers are located on the anode and cathode side of the membrane.

Membrane electrode assembly (MEA) consists of the membrane and catalyst layers on the anode and cathode side of the membrane, the MEA is usually provided by the manufacturer in the assembled form, hence the name.

Gas diffusion layer is a porous structure made of carbon paper or carbon cloth, its primary function is to ensure uniform reactant distribution along the entire flow field and to enhance the removal of water generated inside the cathode catalyst layer. Gas diffusion layer is usually doped with polytetrafluorethylene to enhance the hydrophobicity, i.e. increase the contact angle of water, on the gas diffusion layer surface.

Bipolar plate is a solid structure made from chemically inert materials which are relatively passive in the atmosphere of oxygen and hydrogen. Commonly used materials are molded carbon (carbon powder impregnated with epoxy resin), stainless steel and titanium. The function of bipolar plates is to ensure steady supply of the reactants along the entire flow field via flow channels, i.e. commonly referred to as flow field, machined or imprinted in the surface facing the membrane. Its function is also to ensure structural rigidity requirements for the PEM fuel cell stack assembly due to requirement for application of the required compression force The bipolar plate materials must be electrically conductive to minimize the ohmic losses during the passage of the direct current from the gas diffusion layers to the current collector terminals. Most of the commercial stacks also have a coolant loop, therefore the coolant channels are also machined between the adjacent bipolar plates, i.e. commonly referred to as coolant flow field. The coolant is used for heat removal from the stack and for maintenance of the desired temperature profile along the entire flow field. The name bipolar plate is derived from the fact that the anode side of one cell is serially connected to the cathode side of other cell. For a single cell, the bipolar plates can be referred to as monopolar plates.

Gaskets are used to prevent reactant leakage during operation, and ensure uniform distribution of the pressure on the gas diffusion layers, the gaskets are placed between the bipolar plates around the membrane electrode assembly.

End plate is a structural component of the cell to ensure the required uniform compression force along the entire flow field and keep the stack assembled during operation. End plates have specially designed fittings for the inlets and outlets of the reactants and the coolant. Some of the end plates have machined flow fields on the face in the membrane direction, in such cases they can be referred to as monopolar plates.

2.2   Operation principle and governing equations

Fuel cell is an energy conversion device that converts the chemical energy of fuel into electrical energy. Schematic of a PEM fuel cell is shown in Figure 1.
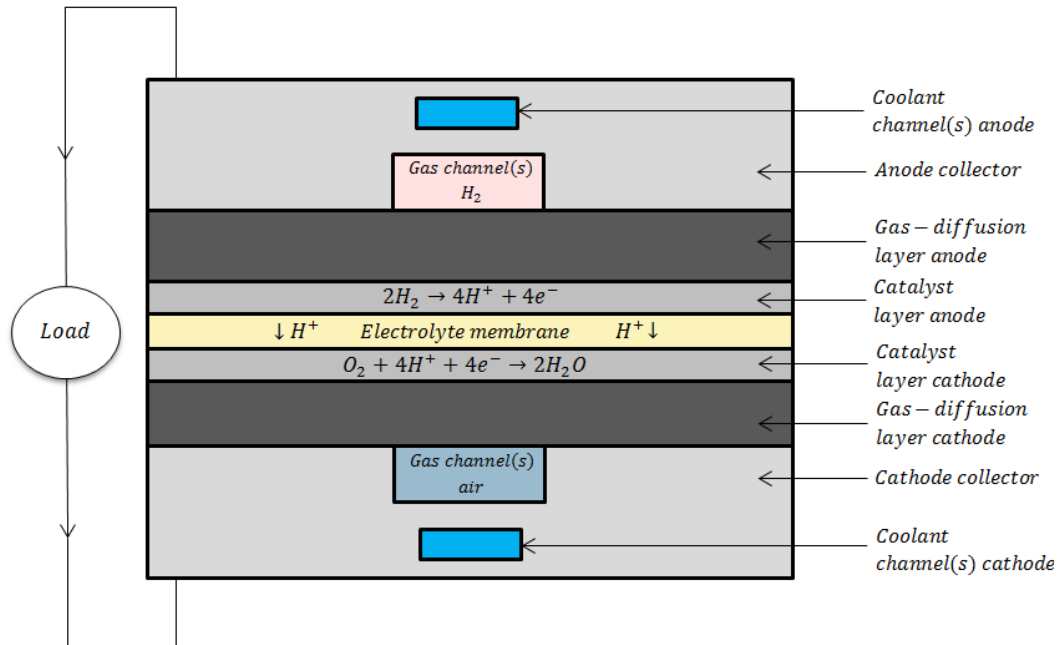
Figure 1. PEM fuel cell cut-through view.

This chapter is dedicated to description of the theoretical basis of PEM fuel cell modeling by using the computational fluid dynamics modeling software ANSYS Fluent, along with brief description of the multi-physical phenomena inside an operating cell.

Hydrogen flows into the fuel cell on the anode side. It diffuses through the porous gas diffusion layers and reaches the catalyst layer, where it forms ions and electrons. The ions diffuse through the polymer electrolyte membrane, and electrons flow through the anode gas diffusion layer to the anode current collector and into the electric load attached. The electrons enter the cathode side through the cathode current collector, and pass through the cathode gas diffusion layer. Upon reaching the cathode catalyst layer, the electrons, hydrogen ions and oxygen combine to form water and release heat.

During the numerical simulation, two electric potential fields are solved. One is solved in the electrolyte and the triple-phase boundary layer, i.e. catalyst layer, while the other is solved in the triple-phase boundary catalyst layer, the porous electrode and the current

collectors. The rates of electrochemical reactions are computed in the triple-phase boundary layers at both the anode and the cathode. Based on the cell voltage prescribed, the current density value is computed – potentiostatic approach. Alternatively, the cell voltage can be computed based on a prescribed average current density – galvanostatic approach.

2.2.1 Overview

Over the last decade, the PEM fuel cell has emerged as a favored technology for automotive transportation and power generation due to its favorable characteristics: compact size, clean energy conversion, the ability to run at low temperatures (<100 °C), ability of an adjustable power output, and the ability for a relatively rapid start up.

Hydrogen is supplied at the anode, and air (or pure oxygen) is supplied at the cathode. The following chemical reactions take place in the anode and cathode triple-phase boundaries, respectively

$$H_2 \Leftrightarrow 2H^+ + 2e^- \text{ (anode)} \tag{1}$$

$$\frac{1}{2}O_2 + 2e^- + 2H^+ \Leftrightarrow H_2O \text{ (cathode)} \tag{2}$$
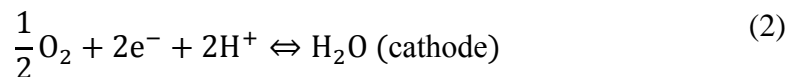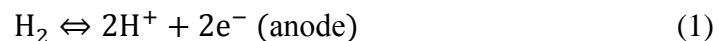
Electrons produced in the anode travel through an external circuit to the cathode, while protons (H^+) travel through the membrane from the anode triple-phase boundary layer to the cathode triple-phase boundary layer, thereby forming an electrical circuit.

As the amount of generated water increases at the cathode, due to the effect of electro-osmotic drag and electrochemical reactions, water vapor pressure exceeds the saturation pressure and liquid water is formed. The occurrence of liquid water in the cathode can strongly influence the performance of PEM fuel cell.

2.2.2 Electrochemistry

The electrochemistry modeling is revolved around the computation of the rates of the anodic and cathodic reactions. The electrochemistry model adopted in ANSYS Fluent is similar to the one used by other research groups [9-11].

The driving force behind the reactions is the surface overpotential – the difference between the phase potential of the solid and the phase potential of the electrolyte/membrane. For this reason, two potential equations are solved within Fuel Cell Module. One potential equation (3) accounts for the electron e^- transport through the solid conductive materials – current collectors and solid portion of the porous media, while the other potential equation (4) represents the ionic transport of H^+ or O^{-2}. The potential equations are

$$\nabla(\sigma_{sol}\nabla\phi_{sol}) + R_{sol} = 0 \qquad (3)$$

$$\nabla(\sigma_{mem}\nabla\phi_{mem}) + R_{mem} = 0 \qquad (4)$$

where σ ($\Omega^{-1}\,m^{-1}$) represents electrical conductivity, ϕ (V) is electric potential and R (A m^{-3}) represents volumetric transfer current.

There are two types of external boundary conditions: those that allow the passage of electrical current, and those that do not. Figure 2. illustrates the boundary conditions used for solving ϕ_{sol} and ϕ_{mem}.

$$\frac{\partial \phi_{mem}}{\partial n} = 0$$

$$\frac{\partial \phi_{sol}}{\partial n} = 0$$

$$\frac{\partial \phi_{mem}}{\partial n} = 0$$

$$\phi_{sol} = 0$$

$$\frac{\partial \phi_{mem}}{\partial n} = 0$$

$$\frac{\partial \phi_{sol}}{\partial n} = 0$$

Coolant channel(s) anode

Gas channel(s) H_2

Anode collector

Gas − diffusion layer anode

$2H_2 \rightarrow 4H^+ + 4e^-$

Catalyst layer anode

$\downarrow H^+$ Electrolyte membrane $H^+ \downarrow$

$O_2 + 4H^+ + 4e^- \rightarrow 2H_2O$

Catalyst layer cathode

Gas − diffusion layer cathode

Gas channel(s) air

Cathode collector

Coolant channel(s) cathode

$$\phi_{sol} = V_{cell} \text{ or} \frac{\partial \phi_{sol}}{\partial n} = \text{constant}$$

$$\frac{\partial \phi_{mem}}{\partial n} = 0$$
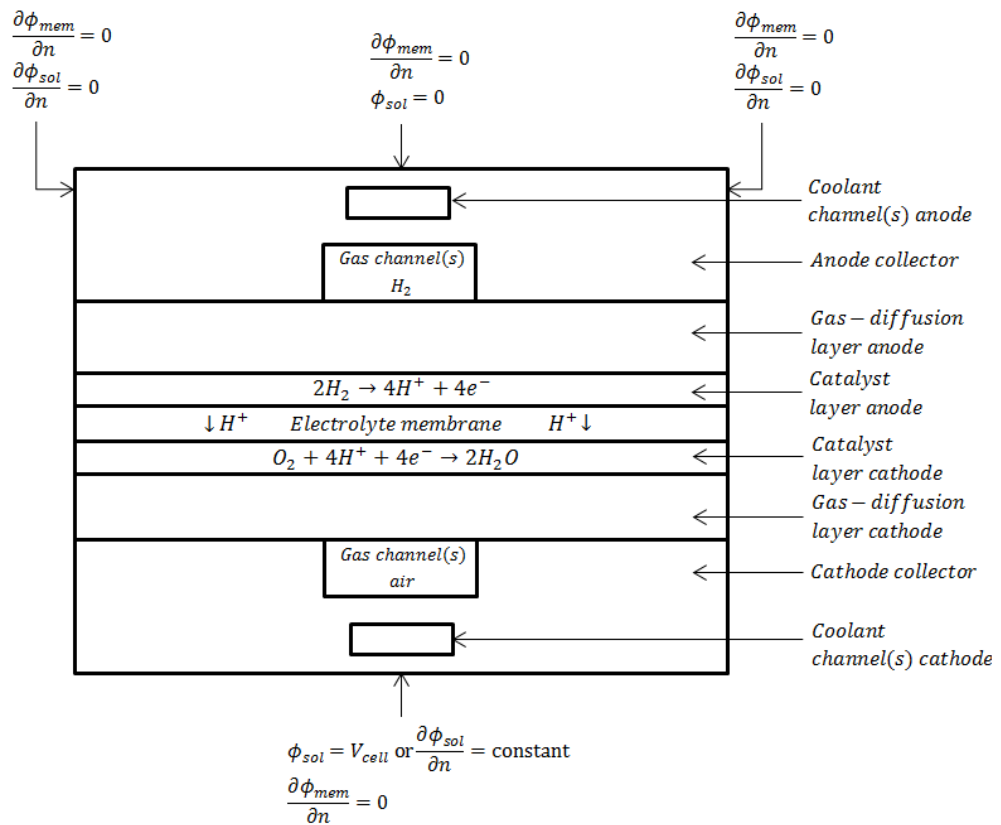
Figure 2. External electrical boundary conditions.

Since ionic current does not leave the fuel cell through external boundaries, all external boundaries have a zero flux boundary condition for the membrane phase potential ϕ_{mem}. For the solid phase potential ϕ_{sol}, the external boundaries on the anode and the cathode side are in contact with the external electric circuit and the electrical current generated by the fuel cell passes only through these boundaries, i.e. current collector terminals. All other external boundaries are defined as zero flux boundary conditions for ϕ_{sol}.

The external boundaries can be defined in two ways. Both ways require definition of zero electric potential on the anode side. The first way is definition of a positive value of electric potential on the cathode terminals, *i.e.* potentiostatic approach. The second is definition of a negative value of current flux density on the cathode terminals (in A m^{-2}). The first approach is recommended by the manual [12], but since the resulting current density is unknown in the first iteration, it requires a couple of steps to achieve the desired current density for a fixed mass flow rate. The first approach enables definition of the

desired electric potential regardless of its value. The second approach is straight-forward, since the mass flow rate of the reactants is easily determined using Faraday's law, but it requires application of a smaller current density in the beginning and step-like increase of the current flux density with a maximal step of 0.2 A cm^{-2} to get to the desired current density, or the solution will diverge.

The transfer currents, *i.e.* the source terms from equations 3 and 4, are non-zero only inside the catalyst layers and are computed as:

For the solid phase, $R_{sol} = -R_{an}(< 0)$ on the anode side and $R_{sol} = +R_{cat}(> 0)$ on the cathode side

For the membrane phase, $R_{mem} = +R_{an}(> 0)$ on the anode side and $R_{mem} = -R_{cat}(< 0)$ on the cathode side

The source terms R_{an} and R_{cat} in equations 3 and 4 are also called the exchange current densities (A m^{-3}), the general definitions of exchange current densities are

$$R_{an} = \left(\zeta_{an} j_{an}^{ref}\right) \left(\frac{[A]}{[A]_{ref}}\right)^{\gamma_{an}} \left(e^{\frac{\alpha_{an} F \eta_{an}}{RT}} - e^{\frac{-\alpha_{cat} F \eta_{an}}{RT}}\right) \tag{5}$$

$$R_{cat} = \left(\zeta_{cat} j_{cat}^{ref}\right) \left(\frac{[C]}{[C]_{ref}}\right)^{\gamma_{cat}} \left(-e^{\frac{\alpha_{an} F \eta_{cat}}{RT}} + e^{\frac{-\alpha_{cat} F \eta_{cat}}{RT}}\right) \tag{6}$$

where j^{ref} represents exchange current density per active surface area, ζ specific active surface area, $[\ ], [\ ]_{ref}$ local species concentration, γ concentration dependency coefficient, α transfer coefficient, F Faraday constant, η local overpotential, *i.e.* activation loss, R gas constant and T temperature. Equations (5) and (6) represent the general formulation of the Butler-Volmer function. A simplified form of the expression is given in the form of Tafel formulation

$$R_{an} = \left(\zeta_{an} j_{an}^{ref}\right) \left(\frac{[A]}{[A]_{ref}}\right)^{\gamma_{an}} \left(e^{\frac{\alpha_{an} F \eta_{an}}{RT}}\right) \tag{7}$$

$$R_{cat} = \left(\zeta_{cat} j_{cat}^{ref}\right) \left(\frac{[C]}{[C]_{ref}}\right)^{\gamma_{cat}} \left(e^{\frac{-\alpha_{cat} F \eta_{cat}}{RT}}\right) \tag{8}$$

By default, the Butler-Volmer function is used inside the ANSYS Fluent Fuel Cell Module for computation of transfer currents inside the catalyst layers. In equations (5–8), $[A]$ and

$[C]$ represent the molar concentration of the species upon which the anode and cathode reaction rates depend, recpectively. For PEM fuel cell, A represents H_2 and C represents O_2.

The driving force for the kinetics is the local surface overpotential η, known as the activation loss, and it generally represents the difference between the solid ϕ_{sol} and membrane ϕ_{mem} potentials. The gain in electric potential from crossing from the anode to the cathode side is taken into account by subtracting the open-circuit voltage V_{OC} on the cathode side

$$\eta_{an} = \phi_{sol} - \phi_{mem} \tag{9}$$

$$\eta_{cat} = \phi_{sol} - \phi_{mem} - V_{OC} \tag{10}$$

Equations 3-10 are used for obtaining the two potential fields.

2.2.3 Current and mass conservation

Species volumetric source terms in the triple-phase boundaries due to electrochemical reactions for the PEM fuel cell are

$$S_{H_2} = -\frac{M_{w,H_2}}{2F} R_{an} < 0 \tag{11}$$

$$S_{O_2} = -\frac{M_{w,H_2}}{4F} R_{cat} < 0 \tag{12}$$

$$S_{H_2O} = \frac{M_{w,H_2O}}{2F} R_{cat} > 0 \tag{13}$$

Since the total electrical current produced in the cathode and the anode triple-phase boundaries is the same, the following equation is considered for current conservation

$$\int_{an} R_{an} dV = \int_{cat} R_{cat} dV \tag{14}$$

2.2.4 Heat source

Additional volumetric sources to the thermal energy equation are present because not all chemical energy released in the electrochemical reactions can be converted to electrical work due to irreversibility of the processes. The total source that sums up the energy equation, *i.e.* enthalpy is

$$S_h = h_{react} - R_{an,cat}\eta_{an,cat} + I^2 R_{ohm} + h_L \tag{15}$$

where h_{react} represents the net enthalpy change due to the electrochemical reactions, $R_{an,cat}\eta_{an,cat}$ the product of the transfer current and overpotential in the anode or cathode triple-phase boundaries, R_{ohm} the ohmic resistance of the conducting media, and h_L is the enthalpy change due to condensation/vaporization of water.

2.2.5 Liquid water formation, transport and its effects

Since PEM fuel cells operate under relatively low temperatures (<100 °C), the water vapor may condense to liquid water, especially at high current densities. While the existence of the liquid water keeps the membrane hydrated, it also prevents the gas diffusion, reduces the diffusion rate and the effective reacting surface area and consequently the cell performance. To model the formation and transport of liquid water, ANSYS Fluent uses a saturation model based on [13,14]. In this approach, the liquid water formation and transport is governed by the following conservation equation for the volume fraction of liquid water, s, or the water saturation

$$\frac{\partial(\varepsilon\rho_l s)}{\partial t} + \nabla(\rho_l \vec{v}_l s) = r_w \tag{16}$$

where the subscript l stands for liquid water, and r_w is the condensation rate that is modeled as

$$r_w = c_r \, max\left(\left[(1-s)\frac{p_{wv} - p_{sat}}{RT} M_{w,H_2O}\right], [-s\rho_l]\right) \tag{17}$$

where r_w is added to the water vapor equation, as well as the pressure correction (mass source). This term is applied only inside the catalyst and gas diffusion layers. The condensation rate constant is hardwired to $c_r = 100 \, s^{-1}$. It is assumed that the liquid velocity v_l is equivalent to the gas velocity inside the gas channel (that is, a fine mist).

Inside the highly-resistant porous zones, the use of the capillary diffusion term allows us to replace the convective term in equation (16), with

$$\frac{\partial(\varepsilon\rho_l s)}{\partial t} + \nabla\left[\rho_l \frac{K s^3 dp_c}{\mu_l ds}\nabla s\right] = r_w \tag{18}$$

Depending on the wetting phase, the capillary pressure is computed as a function of s (the Leverett function)

$$p_c = \begin{cases} \dfrac{\sigma cos\theta}{\left(\frac{K}{\varepsilon}\right)^{0.5}}(1.417(1-s) - 2.12(1-s)^2 + 1.263(1-s)^3) & \theta_c < 90° \quad (19) \\[4em] \dfrac{\sigma cos\theta}{\left(\frac{K}{\varepsilon}\right)^{0.5}}(1.417s - 2.12s^2 + 1.263s^3) & \theta_c > 90° \\ & \quad (20) \end{cases}$$

where ε represents the porosity, σ the surface tension, θ_c the contact angle and K the absolute permeability. Equation (16) is used for modeling various physical processes, such as condensation, vaporization, capillary diffusion and surface tension. The clogging of the porous media and the flooding of the reaction surface are modeled by multiplying the porosity and the active surface area by $(1 - s)$, respectively.

2.3 Physical properties and water transport through the membrane

The following expressions are used for calculation of the physical properties of materials and the water transport across the membrane.

2.3.1 Gas phase species diffusivity

Gas phase species diffusivities can be computed either by using the dilute approximation method, or by using the full multicomponent method. The dilute approximation method is represented by

$$D_i = \varepsilon^{1.5}(1-s)^{r_s}D_i^0\left(\frac{p_0}{p}\right)^{\gamma_p}\left(\frac{T}{T_0}\right)^{\gamma_t} \tag{21}$$

where D_i^0 represents the mass diffusivity of species i at reference temperature and pressure p_0, T_0 (reference 9). The reference values and the exponents, γ_p, γ_t, as well as the exponent of pore blockage r_s are defined in the Fluent Fuel Cell Module user defined functions as

$$p_0 = 101325 \text{ N m}^{-2} \tag{22}$$

$$T_0 = 300 \text{ K}$$

$$\gamma_p = 1$$

$$\gamma_t = 1.5$$

$$r_s = 2.5$$

In addition to equation 20, the Fluent Fuel Cell Module also contains a method for computation of the gas phase species diffusion, *i.e.* a full multicomponent diffusion method with correction for the porous media tortuosity

$$D_{eff}^{ij} = \varepsilon^{1.5} D^{ij} \tag{23}$$

where D_{eff}^{ij} represents the effective gas species diffusivity, ε porosity of the porous medium, and D^{ij} is the gas species mass diffusivity computed by the full multicomponent diffusion method. Properties such as electrolyte phase electrical conductivity, water diffusivity and osmotic drag coefficient are evaluated as functions of the water content, using correlations as suggested by [15]. To capture the relevant physics of the problem, various properties of the membrane are incorporated into the model as default options.

2.3.2 Electrolyte phase (ionic) conductivity

For PEM fuel cell, the electrolyte (membrane) phase conductivity is modeled as

$$\sigma_{mem} = \beta(0.514\lambda - 0.326)^\omega e^{1268(\frac{1}{303} - \frac{1}{T})} \tag{24}$$

where λ represents the membrane water content. The constants β and ω are introduced in ANSYS Fluent for generality. Equation (24) becomes the original correlation from [15] when $\beta = \omega = 1$.

2.3.3 Osmotic drag coefficient

$$n_\mathrm{d} = \frac{2.5\lambda}{22} \tag{25}$$

2.3.4 Back diffusion flux

$$J_\mathrm{w}^\mathrm{diff} = -\frac{\rho_\mathrm{m}}{M_\mathrm{m}} M_{\mathrm{H_2O}} D_\mathrm{l} \nabla \lambda \tag{26}$$

where ρ_m and M_m represent the density and equivalent weight of the dry membrane, respectively, and D_l is membrane water diffusivity.

2.3.5 Membrane water diffusivity

$$D_\mathrm{l} = 3.1 \times 10^{-7}\lambda\left(e^{0.28\lambda} - 1\right)\left(e^{-\frac{2346\,[K]}{T}}\right) \quad \lambda < 3 \tag{27}$$

$$D_\mathrm{l} = 4.17e \times 10^{-8}\lambda\left(1 + 161e^{-\lambda}\right)\left(e^{-\frac{2346\,[K]}{T}}\right) \quad \lambda \geq 3$$

2.3.6 Membrane water content

The expression for the membrane water content λ is obtained using Springer et al. correlation [15].

$$\lambda = 0.043 + 17.18a - 39.85a^2 + 36a^3 \quad a < 1 \tag{28}$$

$$\lambda = 14 + 1.4(a - 1) \quad a \geq 1$$

where a represents the water activity, defined as

$$a = \frac{p_\mathrm{wv}}{p_\mathrm{sat}} + 2s \tag{29}$$

2.3.7 Water vapor pressure

The water vapor pressure is computed from the vapor molar fraction x and the local pressure p

$$p_{\text{wv}} = x_{\text{H}_2\text{O}} p \tag{30}$$

2.3.8 Saturation pressure

The default unit for saturation pressure calculation in ANSYS Fluent is atm, defined by the following expression

$$log_{10}\, p_{\text{sat}} = -2.1794 + 0.02953(T - 273.17) \tag{31}$$

$$-9.1837 \times 10^{-5}(T - 273.17)^2$$

$$+1.4454 \times 10^{-7}(T - 273.17)^3$$

It is noted here that in [15], water activity is defined on the basis of total water or super-saturated water vapor. With phase change being invoked in the present two-phase model, $2s$ is added to the original formulation as suggested by [16].

2.4 Leakage current (cross-over current)

The leakage current, I_{leak}, models the effect of species cross-over from one electrode to another across the electrolyte. In addition to the source terms expressed by equations (11–13), the expressions are

$$S_{\text{H}_2} = -\frac{M_{\text{w,H}_2}}{2F \cdot Vol_{\text{anode}}} I_{\text{leak}} \tag{32}$$

$$S_{\text{O}_2} = -\frac{M_{\text{w,O}_2}}{4F \cdot Vol_{\text{cathode}}} I_{\text{leak}} \tag{33}$$

$$S_{\text{H}_2} = -\frac{M_{\text{w,H}_2\text{O}}}{2F \cdot Vol_{\text{anode}}} I_{\text{leak}} \tag{34}$$

2.5 Fluid dynamics

2.5.1 Continuity

$$\nabla\left(\rho\,\vec{V}\right) = S_{\text{mass}} \tag{35}$$

where S_{mass} represents source term for continuity equation. This term is only applicable for the triple-phase boundary (catalyst) regions. Inside the gas channels, gas diffusion layers and the membrane, the source term S_{mass} is set to zero.

2.5.2 Momentum

$$\frac{1}{s(1-s)}\nabla\left(\rho\,\vec{V}\vec{V}\right) = -\nabla p + \frac{1}{s(1-s)}\nabla\left(\mu\,\nabla\vec{V}\right) + \rho g + S_{\text{mom}} \tag{36}$$

where S_{mom} represents the source term for momentum equation and applies only for the porous medium. For other domains, S_{mom} is set to zero.

2.5.3 Species

$$\nabla\left(\rho\,\vec{V}X_{\text{i}}\right) = -\nabla(\rho D_{\text{i}}\nabla X_{\text{i}}) + S_{\text{i}} \tag{37}$$

where the index i represents different species − oxygen, hydrogen and water vapor. The term S_{i} represents the source and sink term for the species inside the catalyst layers and accounts for the reactant consumption in anode and cathode catalyst layers and water generation inside the cathode catalyst layer. In other domains, the term S_{i} value is set to zero.

2.5.4 Energy

$$\nabla\left(\rho\,\vec{V}T\right) = \nabla\left(k^{\text{eff}}\nabla T\right) + S_{\text{T}} \tag{38}$$

where S_{T} represents the heat source term for the energy equation. The heat source term S_{T} applies only for the cathode catalyst layer, for other domains it is set to zero.

3   REVIEW OF PREVIOUS RESEARCH

PEM fuel cell operation is highly dependent on water and heat management [8,17]. The water management is important because the membrane ionic conductivity is proportional to the membrane water content, i.e. number of water molecules per one perfluorosulfonic acid molecule [18], as previously mentioned. The membrane water content is dependent on relative humidity of the reactants. If relative humidity of the reactants is low, the membrane will be dehydrated, and the ionic conductivity of the membrane will be low, therefore high relative humidity of the reactants is required for high performance operation. To ensure high relative humidity of the reactants, the reactants require humidification before entering the cell. The necessity for external humidification increases the system complexity and economic costs. Humidification is a thermodynamic process based on evaporating liquid water and saturating the reactant gas passing through the humidifier with water vapor at 100% relative humidity for the prescribed temperature, therefore the process requires water and heat. Since water and heat are already produced during PEM fuel cell operation from the electrochemical reaction of hydrogen and oxygen on the triple-phase boundaries inside the cathode catalyst layer, it is logical to presume that the generated water and heat could be used to humidify the reactants and thereby improve the performance of the cell [1,17,19]. The generation of liquid water is especially important at higher current densities, since the reactants are already saturated with water vapor, and cannot evaporate the generated water. This results in pooling of the liquid water inside the porous gas diffusion layers and decreases the active area of the catalyst layers since the reactants are unable to pass through liquid water. Excessive water accumulation in the gas diffusion layers can cause the flooding of the reactant channels and consequently cause starvation of the cell. Starvation of the cell results in catastrophic performance and irreversible degradation of the cell [17] and must therefore be prevented at all times.

The relative humidity of the reactants, fuel (hydrogen) and oxidant (pure oxygen or oxygen from atmospheric air) is one of the most important operating parameters of PEM fuel cell [1]. There are many works dealing with investigation of the influence of relative humidity of the reactants on PEM fuel cell operation and efficiency [19-24]. The idea of keeping the relative humidity of the reactants along the entire flow field near the water vapor saturation profile is beneficial for the cell operation and results in increased life time of the cell.

However, as previously mentioned, the water balance of the cell is a very sensitive topic since it affects the membrane ionic conductivity. The flooding results in unstable polarization curve, while higher amounts of liquid water inside the cell cause mass transport losses, evident from sudden decrease in operating electric potential at higher operating current densities. Operation in membrane dehydration regimes, or cycling between low and high relative humidity of the reactants results in increased degradation of the cell [25].

Heat management of PEM fuel cell is important due to the fact that the relative humidity of reactants is temperature dependent, since the pressure drop is minor. The cell is usually kept at a constant temperature along the entire flow field and regulated with the coolant fluid mass flow rate. The coolant enters the cell at a prescribed temperature with the mass flow rate which will result in uniform temperature distribution (i.e. very small temperature gradient) along the entire flow field. However, since the fuel cell generates heat during operation, the coolant temperature will increase towards the outlet of the cell. If the bipolar plates are made from materials characterized by low thermal conductivity, the temperature along the reactant channels will be higher than the temperature of the coolant liquid. For the same amount of generated water, i.e. for the same generated electrical current, the result is decreased relative humidity of the reactants, and decreased performance of the cell, i.e. decreased electric potential. Therefore, special care must be taken to account for this temperature difference.

Besides water and heat management, there are other parameters influencing PEM fuel cell operation, such as the flow field geometry, i.e. the shape and size of the reactant channels, the clamping force (which is usually prescribed by the manufacturer of the membrane electrode assembly, but not in all cases), temperature and gauge pressure of the reactants, and the microstructure of the membrane, electrodes and the porous gas diffusion layers. One of the most comprehensive approaches for investigating in situ operation of the cell is segmentation of the fuel cell [1,8,26-31]. The segmentation of the cell is basically division of a single cell in a number of electrically and thermally insulated segments, and enables measurement of the operating parameters such as electrical current, temperature and sometimes even relative humidity before and after each segment of the cell. The segments are electrically interconnected in parallel with a common current collector terminal. This

enables investigation of the condensation of water inside the cell during operation, the membrane dehydration, and water transport (if relative humidity is measured before and after each segment). It also enables the study of the current density distribution along the cell, and investigation of the rate of change of operating parameters under dynamic load changes, which is of special importance for automotive applications.

Experimental segmented fuel cell can be used for determination of the optimal operating parameters of the cell and enable development of a robust numerical model which can be later used for different what-if scenarios to determine the parameter sets for high performance of the cell.

The following chapters give insight in the research by different groups of authors in the fields of heat [32-37] and water management of PEM fuel cells [38-48], computational fluid dynamics modeling [49-55] of PEM fuel cells and the design of an advanced model of a segmented PEM fuel cell [8,26] required for in-depth experimental investigation.

3.1   Heat management

Heat management of PEM fuel cells represents the balance of the generated heat by the electrochemical reactions of hydrogen and oxygen inside an operating cell with the adequate methods of heat removal from the system. Most of the research done by different groups of authors in the past is concentrated on establishing a uniform temperature flow field for PEM fuel cell operation, however, some of them indicated the potential of improving the performance of the fuel cell by introducing a spatially variable temperature flow field.

Zhang and Kandlikar [32] investigated the applicability of different coolant strategies for PEM fuel cell stacks. The investigated coolant techniques were (i) cooling with heat spreaders, i.e. passive cooling, (ii) cooling with separate air flow, (iii) cooling with liquid coolant (water or propylene-glycol and water mixture), and (iv) evaporation cooling, i.e. cooling through boiling. The conclusion is that (i) heat spreader cooling requires very expensive materials such as pyrolytic graphite, characterized by extremely high in-plane thermal conductivities to enable sufficient heat dissipation at higher operating loads. Cooling with separate air flow (ii) is inefficient due to very low specific heat of air, and the requirement for high mass flow rates of air in the separate cooling channels, resulting in

requirement for higher overall volume of the stack and only applicable for lower operating current densities. Liquid cooling (iii) is observed to have the most applicability due to the fact that water has very high specific heat and enables sufficient heat removal rates even at high currents, while the propylene-glycol and water mixture enables operation for sub-zero start-up temperatures. The problem with liquid cooling is ionization of the coolant water with operation, and in order to prevent this behavior the water must be deionized after a certain electrical conductivity is reached. This can be prevented by using kerosene instead of water, with roughly half the specific heat of water and required twice higher mass flow rate, but does not require de-ionization during operation of the cell. The problem with liquid cooling is the requirement for a circulation pump, heat exchanger and the temperature control of the coolant water. Evaporation cooling (iv) is an interesting solution for PEM fuel cell cooling, however, it does not enable sufficient cooling of the cell, since the evaporative cooling can roughly dissipate only 10-15% of the required heat for high performance of the cell. Evaporative cooling can however improve the performance of the cell during operation when coupled with liquid cooling. The general conclusions of this work are that the liquid cooling is the only option for higher current densities and PEM fuel cell stack cooling.

Chen et al. [33] investigated the influence of different coolant flow fields on fuel cell performance, in order to optimize the coolant flow field configuration for a PEM fuel cell stack. The criterion for cooling efficiency was the overall temperature variation along the entire area of the cooling flow field, by the self-proclaimed Index of Uniform Temperature. Six different flow fields were investigated and compared, three of the serpentine configuration and three of a parallel configuration, Figure 3. Serpentine coolant flow field resulted in higher Index of Uniform Temperature, meaning that the overall temperature difference was lower when compared to the parallel coolant flow field, however the pressure drop across the serpentine flow field is higher. However, the influence of the temperature non-uniformity on the cell performance was not studied in this work.

(1) (2) (3)

(4) (5) (6)
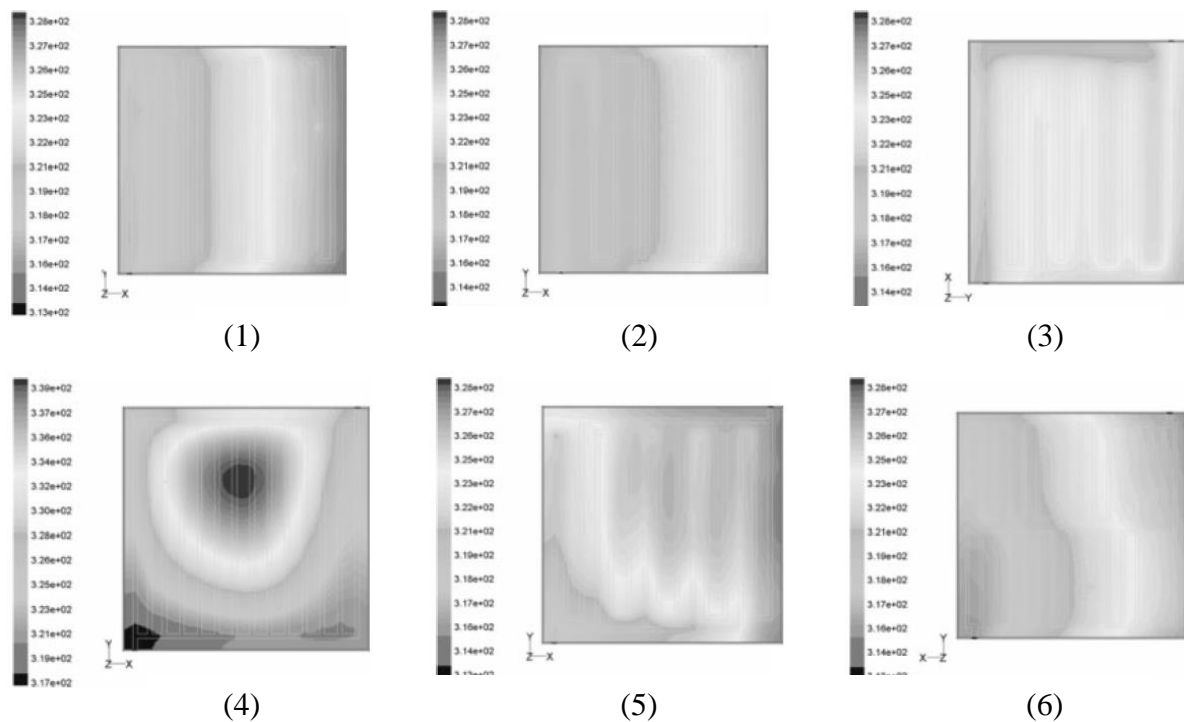
Figure 3. Comparison of temperature distributions along the current collectors for serpentine (1,2,3), and parallel (4,5,6) flow field configurations, adopted from [33].

Mench et al. [34] have proposed that non-uniform cooling could be beneficial for PEM fuel cell performance if optimized for the prescribed reactant gas flow rates and operating parameter configuration. If the coolant channels are designed and flow rates are such that the temperature in the gas channels gradually increases in the downstream direction, it can be used to mitigate the flooding issue, since the water saturation pressure is increasing with the temperature. The concept of non-uniform, i.e. variable, cooling in this work was only proposed on a theoretical basis, and was not tested experimentally.

Wilkinson et al. [35] patented a stack with co-flow configuration of the coolant with the cathode air, while the anode hydrogen was in counter-flow configuration in respect to the coolant and cathode air. Such setup led to non-uniform cooling, as previously theorized by Mench et al. [34]. The experiments were carried out on a 4-cell stack and the performance of the stack was superior for each temperature differential tested (5, 10, 15 and 20°C) compared to the co-flow of reactants with the coolant. However, this work did not determine the optimal temperature profile, but it resulted in credibility of the non-uniform temperature flow field concept for further investigation.

Kang et al. [36] numerically investigated the influence of the anode, cathode and coolant flow field configurations on the performance of PEM fuel cell. The conclusion was that the counter flow configuration of air and hydrogen, and co-flow of air and coolant result in the highest cell performance, as previously seen in an experimental study of Wilkinson et al. [35]. The performance gain was attributed to higher membrane hydration in the reported configuration. Conclusion of this work was that the experimental data is also successfully modeled and validated by using the numerical approach, but further insight in the physical meaning of the non-uniform temperature profile on PEM fuel cell performance was not clear.

Tolj et al. [8] investigated the PEM fuel cell performance for non-uniform temperature flow field prescribed along the cathode flow field by means of Peltier thermoelements. The single cell was divided in five equal parts, and the temperature profile was extracted from Mollier's h-x chart to closely resemble the water saturation profile, i.e. to achieve relative humidity close to 100% along the entire flow field, Figure 4.
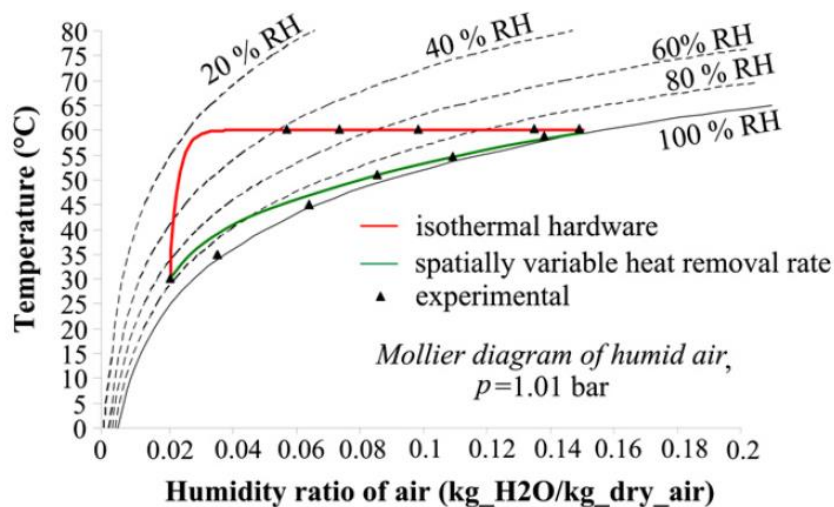
Figure 4. Humidification of air stream along the cathode channel in Mollier's h-x chart, isothermal vs. spatially variable heat removal rate (non-uniform temperature flow field), adopted from [8].

The cell was fed with dry hydrogen and ambient condition air. The experimental results have shown significant improvement in performance when compared to the isothermal case, especially for higher current densities. Establishment of close to 100% relative

humidity along the entire flow field resulted in minimized mass transport losses, a consequence of evaporating the generated liquid water. The relative humidity was measured before and after each segment, and good agreement is achieved with a simple pseudo 2-D model which was also developed in the mentioned work. However, the anode side relative humidity was not measured. Therefore there was no insight in the water transport through the membrane, since it is not possible to determine the balance between the electro-osmotic drag and the back-diffusion flux through the membrane. The requirement for Peltier thermoelements results in non-applicability of the concept for commercial PEM fuel cell stacks.

Ozden et al. [37] developed a three-dimensional computational fluid dynamics numerical model for the experimental setup from Tolj et al. [8]. The single cell was designed with spatially variable heat removal rates, in order to establish the desired temperature profile resulting in close to 100% relative humidity along the entire flow field. The spatially variable heat removal was achieved by introducing aluminum ribs on the cathode side. This work has shown that it is possible to numerically model the non-uniform temperature flow field. However, the relative humidity profile on the cathode side was quite different from the results obtained by Tolj et al. [8] even though it had a similar shape. The concept of using passive cooling was already deemed inefficient for PEM fuel cell stack, as mentioned previously in the work of Zhang and Kandlikar [32], therefore a more robust method of cooling the stack with non-uniform temperature distribution is required.

3.1.1 Conclusions

Investigation of the research by other authors in the field of heat management of PEM fuel cells results in the conclusion that the only feasible cooling system for PEM fuel cell stacks is liquid cooling, which can be used to establish a non-uniform temperature profile along the entire flow field. The coolant channels should be parallel, since they result in non-uniform temperature flow field by default and lower pressure drop when compared to the serpentine flow field. The resulting temperature profile along the flow field should closely resemble the water vapor saturation profile, since the water vapor saturation pressure is temperature dependent. The flow field setup should have cathode air in counter-flow configuration with the anode hydrogen, while the coolant flow should be in co-flow

configuration with the cathode air, since the result is better overall hydration of the membrane. The required temperature profile for high performance PEM fuel cell operation, i.e. water vapor saturation temperature profile, without the requirement for external humidification can be extracted from Mollier's *h-x* chart, based on calculating the amount of generated water inside the cell and the initial conditions of the reactant gases, i.e. temperature and relative humidity of the air and hydrogen upon entry to the cell. It would be very useful to develop a three-dimensional computational fluid dynamics model in order to investigate the cell for different operating conditions. The computational fluid dynamics model should first be calibrated with experimental results for a fixed temperature profile established on the current collector terminals via Peltier thermoelements, and later the temperature profile could be established by the coolant mass flow rate control. The result would be PEM fuel cell setup applicable for commercial stack applications, without the requirement for external humidification.

3.2   Water management

Water management of PEM fuel cells dictates the performance of the cell. The ionic conductivity of the membrane of PEM fuel cell is highly dependent on the membrane water content. If the membrane is dry, the ionic conductivity is low, resulting in poor performance due to high ohmic losses and increased degradation rates. High membrane hydration, resulting from the common application of the external humidification of the reactants, can result in the flooding of the catalyst layers, the gas diffusion layer and the channels at higher current densities, causing a sudden decrease of the cell performance and non-uniform reactant and temperature distribution inside an operating cell, i.e. high mass transport losses. Such operation also results in increased degradation rates, and the requirement for a limited operating range. The liquid water removal is studied in order to determine a simple way to deal with the generated liquid water. One way to improve the performance of the cell without the necessity for external humidification would be to use internally generated water to hydrate the membrane and to evaporate the excess water, but this is possible only under certain operating conditions.

Zawodzinski et al. [18] have experimentally investigated the ionic conductivity of the membrane in relation to the water activity, i.e. relative humidity for commercial Nafion

117 membrane at the temperature of 30°C. They have related the membrane water content with the relative humidity of the reactants by a third degree polynomial expression, which is today commonly used in modeling by various groups of authors. However, the operating temperature of 30°C is quite low, since the PEM fuel cells usually operate at temperatures of 60-80°C, and the membrane thickness is high when compared to currently commercially used membranes. Therefore, the results should be investigated to determine if the expression is valid on higher temperatures.

Hinatsu et al. [38] have investigated the membrane water uptake, i.e. membrane water content for a wide range of operating temperatures, from 25 to 130°C for different membranes, as well as the Nafion 117 membrane. The results of the membrane water content in relation to water activity, i.e. relative humidity of the reactants, show similar trend in regions of lower relative humidity when compared to the results of Zawodzinski et al. [18], however, at higher relative humidity of the reactants, the results are quite different. To conclude, if the results of Zawodzinski et al. [38] at temperature of 30°C are quite different from the results of Hinatsu et al. [38] carried out at higher temperatures, then it is not clear why the expression of Zawodzinski et al. [18] is still widely used today. This suggests that the membrane water uptake should be investigated experimentally for thinner membranes as well.

Yang et al. [39] have studied two Nafion 115 membranes, the first was regular Nafion 115 membrane, and the other one was Nafion 115 membrane with 25%wt zirconium phosphate. Both tests were carried out at 80°C. The results of the membrane water content for the two mentioned membranes at different levels of relative humidity show significant difference between the two. The membrane doped with zirconium phosphate has shown higher membrane water content on high relative humidity levels. This work also shows that different additives in the membrane and temperature also influence the membrane water content, therefore the commonly used membrane water content models deserve further scrutiny.

The water management of PEM fuel cells is directly related to two dominant water transport mechanisms through the membrane. Since high membrane water content is of paramount importance for high efficiency performance of the cell, the water transport through the membrane must be controlled. The water transport through the membrane

consists of the electro-osmotic drag, i.e. the number of water molecules dragged by a single hydrogen proton from the anode to the cathode side of the cell, and diffusion, i.e. water concentration gradient driven flux. The diffusion is usually in the direction from the cathode to the anode side of the membrane, since the water is generated in the cathode catalyst layer, and in that case it is termed back-diffusion. The occurrence of water driven flux from the anode to the cathode side happens only in rare cases where the anode side hydration is high and the cathode is dry. There is also a pressure driven water flux in the case where the anode and cathode side are at different absolute pressures, but in most practical applications this is not the case. The net water transport through the membrane is then basically a balance between the electro-osmotic drag and back-diffusion flux.

Husar et al. [40] have investigated the water transport through the membrane for the three mechanisms specified above. The pressure driven water flux, termed hydraulic permeation in this work, was at least an order of magnitude lower than the electro-osmotic drag and back-diffusion, therefore it is concluded that it is negligible in practical applications. Each of the water fluxes was investigated separately, and good agreement is found between the back-diffusion flux determined experimentally and the data from the literature being used in this work. The electro-osmotic drag, however, was determined to increase with temperature and current density, contrary to other models in the literature, Figure 5.
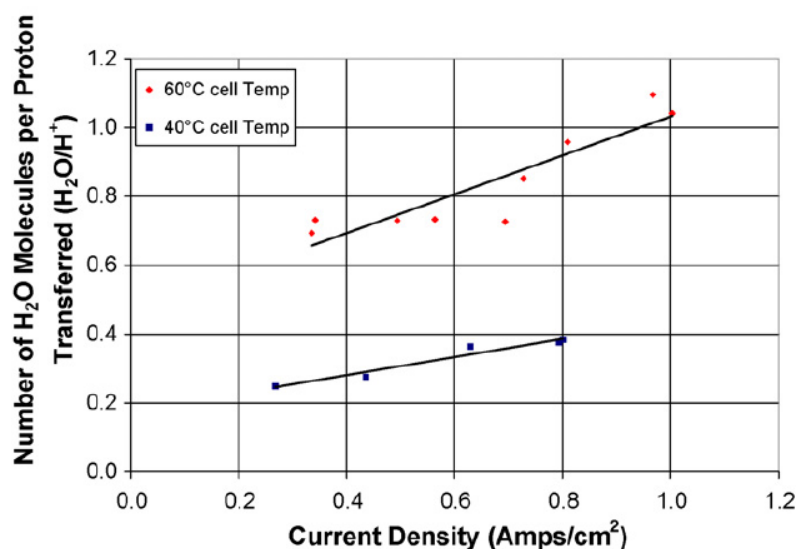
Figure 5. Number of water molecules transferred through the membrane per proton due to electro-osmotic drag at different current densities, adopted from [41].

This work investigated the back-diffusion only on open circuit voltage, at identical operating pressures on the anode and cathode side of the membrane. The open circuit voltage was used to omit the influence of the electro-osmotic drag, however it cannot be seen if the back-diffusion flux changes with the operating current density, therefore a more detailed study should be made.

Jinnouchi et al. [41] have investigated the electro-osmotic drag water flux through Nafion 112 membrane in correlation to the relative humidity, since this was a common approach and most of the models are based on correlating the relative humidity with the electro-osmotic drag coefficient solely. Their conclusion was that the electro-osmotic drag is independent on the relative humidity of the reactants, contrary to most of the models in other works, Figure 6.
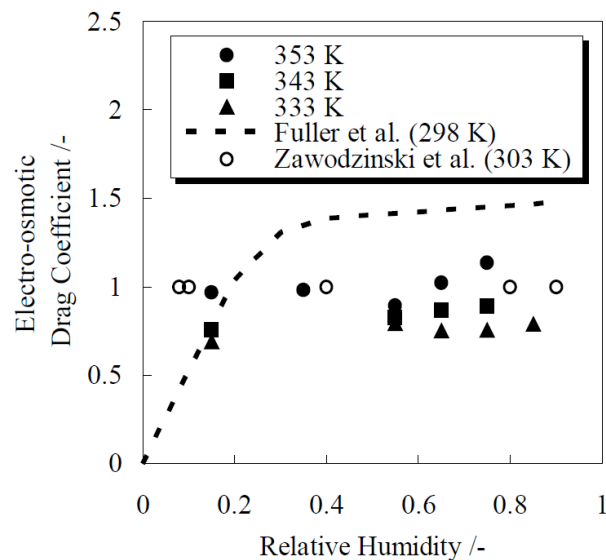
Figure 6. Electro-osmotic drag coefficient of Nafion for various relative humidity and temperature, adopted from [41].

They have also observed that the electro-osmotic drag coefficient proportionally increases with the increase in temperature, similar to the observations of Husar et al. [40]. The two works [40,41] lead to a conclusion that the electro-osmotic drag models commonly used need to be investigated in more detail experimentally.

Olesen et al. [42] have noted that the commonly used back-diffusion model from Motupally et al. [43], correlating the back-diffusion flux to the membrane water content has a peak value of back-diffusion coefficient for the membrane water content value of 3.

The model with the peak back-diffusion value at membrane water content of 3 is also known as Motupally [43] model. The Motupally model is commonly used in various numerical models and shows good agreement with experimental data for higher membrane water content intervals, i.e. higher membrane hydration levels. However, the peak value was not previously explained by other authors. The investigation of the Motupally [43] back-diffusion coefficient model resulted in the conclusion that the peak value at membrane water content value of 3 is simply due to the derivation of the third degree polynomial derived by Zawodzinski et al. [18]. If some other expression is used, for example a higher degree polynomial, or some other function to fit the experimental data point values of Zawodzinski et al. [18], the extreme value at membrane water content value of 3 would not exist. Olesen et al. [42] have derived a new expression for back-diffusion flux which shows good agreement with experimental data from other authors. This work shows that basic mathematical operations used for determining certain operating parameters can cause confusion, and that the models must be first validated experimentally if some unfamiliar phenomenon is observed in the model. Olesen et al. [42] have also noted the difference between the membrane water content at 30°C and 80°C, as previously explained in investigation of works [40] and [41], as seen in Figure 7. They have concluded that the membrane water content must be measured at different temperatures and an expression needs to be derived to determine the correlation of the membrane water content to the temperature, and not solely to the relative humidity of the reactants even though the relative humidity of the reactants is already a function of temperature.
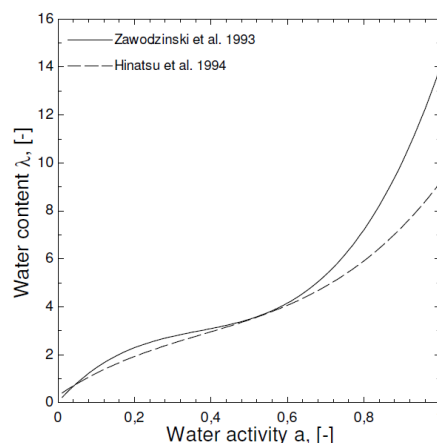
Figure 7. Comparison of membrane water content expressions of Zawodzinski [18] and Hinatsu [38], adopted from [42].

Besides water transport through the membrane, a lot of attention in the literature is recently devoted to the removal of liquid water from the cell. The liquid water is generated in the cell from the electrochemical reaction of the reactants – hydrogen and oxygen, in the cathode catalyst layer. Since the reactants are commonly humidified before the entry to the cell via external humidifiers, the reactants are only able to evaporate small quantities of the generated liquid water. The liquid water is transported through the membrane by the balance of the electro-osmotic drag and back-diffusion, in direction from the anode to the cathode side and vice versa, respectively. The occurrence of liquid water results in pooling of the catalyst layers and the gas diffusion layers from both sides of the membrane. This usually happens at higher current densities, since the amount of generated water is proportional to the operating current density. The pooling of the pores of gas diffusion layers causes un-even reactant distribution along the membrane active area, i.e. the catalyst layer surface, since the reactants are unable to pass through liquid water. A more pronounced pooling can cause channel flooding, i.e. the occurrence of a liquid water plug flow, which can result in starvation of the cell which must be prevented at all times. For this reason, a couple of important works in the literature are outlined to give a better insight in the water removal strategies and the methods for observing the occurrence of the water flooding inside an operating cell.

Hussaini and Wang [44] have designed an operating PEM fuel cell with the cathode side covered by a transparent Lexan plate, thereby enabling in situ visualization of the liquid water occurrence and transport through the cell. They have distinguished three different liquid water two-phase flow patterns inside the micro flow channels – droplets, film flow and slug flow, as seen in Figure 8. Although transparent cell can give a qualitative overview of the liquid water transport through the cell, it is not very useful for analytical study since the perception of the liquid water volume fraction is very poor and cannot be precisely determined from a two-dimensional view. The reflective nature of the gas diffusion layers also hinders the potential of determining the volume fraction of the liquid water inside the cell. Therefore transparent cell methods have limited practical applications.
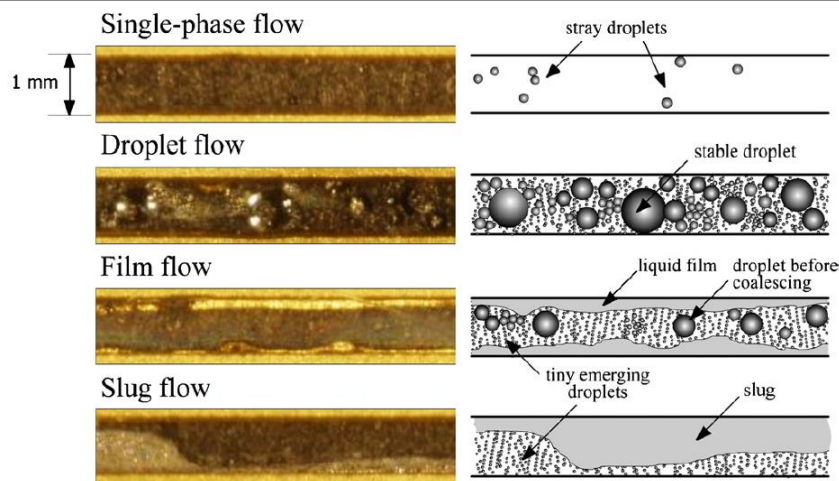
Figure 8. Magnified view of flow patterns in channels and their corresponding line illustrations showing the form and distribution of liquid water, adopted from [44].

Perrin et al. [45] investigated the dynamic water transport for two types of ionomer membranes, Nafion and sulfonated polyimide by field-cycling nuclear magnetic resonance relaxation. The polyimide membrane has shown higher wettability when compared to the Nafion membrane. The nuclear magnetic resonance gives valuable information in regard to the liquid water occurrence in the membrane and the reactant channels, as well as the information on the water transport on a nano-scale level through the membrane pores. However, it shows limited practicality for determining the amount of water inside the porous gas diffusion and the catalyst layers, since the gas diffusion layers are made from paramagnetic carbon. Other drawbacks are the limited temporal and in-plane resolution, and the limited size of the magnet-core for housing a complete PEM fuel cell system.

Mosdale et al. [46] have performed a pioneering work in determining the liquid water distribution inside an operating cell via neutron imaging. The neutron imaging is based on a sensitive response of neutrons to hydrogen-containing compounds, such as water, and insensitivity to commonly used PEM fuel cell structural materials. It is currently the only known tool which meets all three requirements for diagnostics of the liquid water distribution inside PEM fuel cell − localized information on liquid water distribution, minimal invasiveness and in situ applicability. Neutron imaging enables in depth visualization of the dynamic liquid water distribution and transport during PEM fuel cell operation and gives insight in the quantitative values of the liquid water volume and

droplet size spatial distributions. The main drawbacks of the neutron imaging are its high costs and the requirement for radioactive neutron source.

Turhan et al. [47] have employed the neutron imaging in order to investigate the effect of different reactant channels surface hydrophilic/hydrophobic properties on the liquid water transport inside an operating cell, to determine which configuration is more favorable for PEM fuel cell operation. The hydrophilic configuration consisted of gold coated channel walls, while the hydrophobic configuration consisted of polytetrafluorethylene coated channel walls. It was determined that the hydrophilic configuration is more favorable in terms of more stable water transport, since the liquid water is transported in forms of a thin water film on the channel walls, thereby not obstructing the flow of the reactants through the gas diffusion layers and consequently the catalyst, as seen in Figure 9.
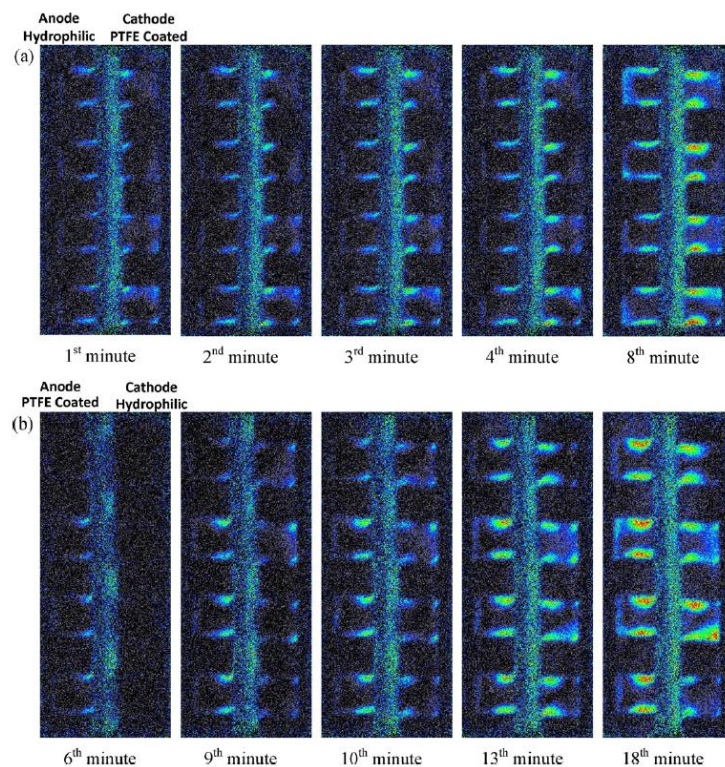
Figure 9. Neutron images of water build-up in gas diffusion layers and water discharge into channels at 0.2 A cm^{-2} operation for (a) anode channel hydrophilic (gold coated)/cathode channel hydrophobic (polytetrafluoethylene coated) and (b) anode channel hydrophobic (polytetrafluorethylene coated)/cathode channel hydrophilic (gold coated), adopted from [47].

However, the water removal was slower with hydrophilic walls since the cross section of the liquid water in respect to the reactants was lower, and the required drag force for pushing the droplets was higher. Also, the accumulation of the liquid water below the land – gas diffusion layer interfaces was higher when compared to the hydrophobic reactant channel configuration. The hydrophobic channel walls resulted in faster water removal from the channels in the form of water droplets, unlike the water film for the hydrophilic case, and higher water removal rates from the land-gas diffusion layer interfaces. However, the hydrophobic walls resulted in water droplet removal across the gas diffusion layer – channel interface, thereby reducing the active area for the reactant passage through the gas diffusion layer. From this work it can be concluded that the optimal combination would be to design the flow field with hydrophilic channel walls and hydrophobic land – gas diffusion layer interfaces. Also, since the geometry of the setup in work [47] of the channels was simple parallel channel design, it would be advisable to also conduct the experiments on more complex flow field geometry, i.e. interdigitated or serpentine type flow fields.

3.2.1 Conclusions

The general conclusion of the water management investigation is that the most fundamental physical property of the membrane, the membrane water content, on which every analytical model is based, deserves further scrutiny. The same conclusion can be drawn from investigation of different experimental results for very similar configurations and operating conditions of PEM fuel cells. The investigation of liquid water transport inside an operating cell is complex and requires costly equipment, such as neutron imaging. The best option would be to develop a new experimental setup which will enable measurement of the water transport through the membrane and development of the membrane water content expression for different temperatures to avoid using potentially erroneous analytical models. Since the investigation of the occurrence of liquid water inside an operating cell results in potentially catastrophic failure of the cell, it would be best to minimize the amount of liquid water inside the cell. For this reason, it would be advisable to investigate the concept of a variable temperature flow field mentioned in the previous chapter, to enable evaporation of the generated liquid water and to use the

generated water vapor to saturate the reactant gases close to 100%. The most suitable tool for investigation of such concept would be a computational fluid dynamics model, which will need to be thoroughly calibrated with some experimental test case.

3.3   Computational fluid dynamics modeling of PEM fuel cells

Computational fluid dynamics (CFD) modeling becomes a common practice in recent years due to development of high performance personal computers, since the application of CFD modeling was only possible on super computers beforehand. CFD modeling enables detailed insight in distributions of local parameters inside an operating cell. However, the CFD model must be validated with experimental data due to very high number of input data required for precise and credible simulations. Even though most of the researchers use commercial software, it is still a challenge to develop a robust PEM fuel cell model due to the requirement for high number of experimental input parameters and the multi-disciplinary knowledge required for explanation of different phenomena inside an operating cell.

Gurau et al. [48] have made the first CFD model of a PEM fuel cell. The model was two-dimensional but it incorporated most of the physical processes inside an operating cell. The work of Gurau et al. [48] resulted in of PEM fuel cell add-ons of commercial CFD softwares. However, the two-dimensional model is a dramatic simplification of PEM fuel cell, since it does not consider the non-uniform distribution of current density, reactant concentration, relative humidity, temperature, etc. The conclusion is that the CFD model of PEM fuel cell must be three-dimensional, even for the simplest flow field geometries. Interesting detail in this work is that the agreement of the simulation results and the experimental data for polarization curve is very good, Figure 10, even though the model is dramatically simplified, leading to a conclusion that in order to have a validated model, one should also compare the local parameters with the experimental data.
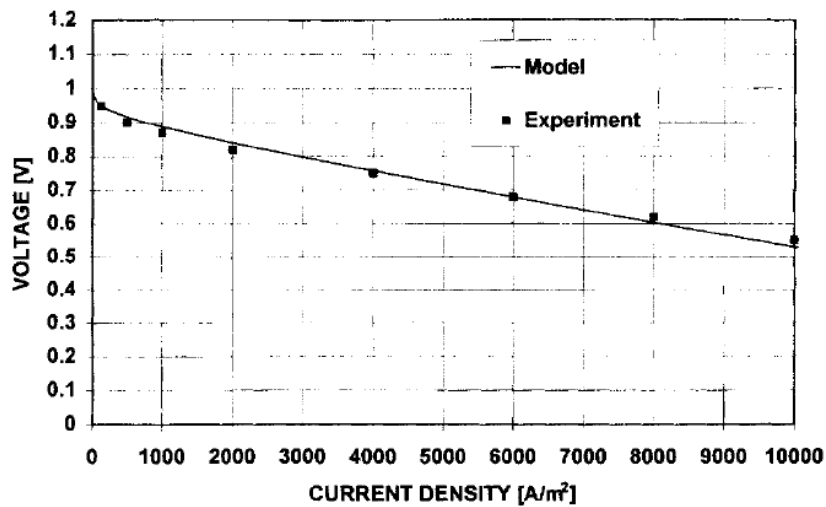
Figure 10. Model and experimental polarization curves, adopted from [48].

Shimpalee et al. [49] have developed first full-scale CFD model of a commercial size PEM fuel cell. The cell had active area of 480 cm^2, the flow field is shown in Figure 11. The results of the simulations carried out in this work show that the operating parameters inside PEM fuel cell, such as temperature, current density and membrane water content are non-uniformly distributed. The non-uniformity of the parameters is strongly influenced by relative humidity of the reactants upon the entry to the cell. Unfortunately, the calibration and experimental validation has not been done in this work, but it was demonstrated that CFD gives valuable insight in multiphysical phenomena inside an operating cell.
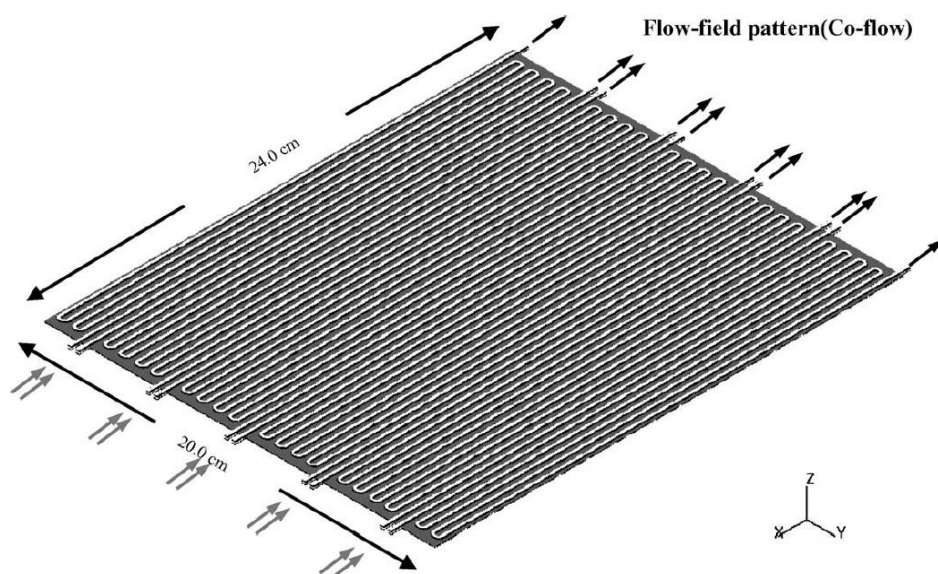
Figure 11. Flow field of a commercial 480cm^2 PEM fuel cell, adopted from [49].

Berning and Djilali [50] have carried out a parametric investigation on their previously developed CFD model, the results are shown in Figure 12. The simulation results have been compared to other experimental data in the literature with good agreement. The conclusion of this work is that in order to simulate the limiting current density occurrence, it is advisable to manipulate the porosity of the gas diffusion layer, i.e. the reduction in the porosity due to accumulation of liquid water inside the gas diffusion layer pores at higher current densities. However, only the global simulation parameters have been compared to the experimental data, such as power curves and polarization curves. The localized data was not compared. Therefore the capability of the model in predicting the local parameter distributions is unclear.
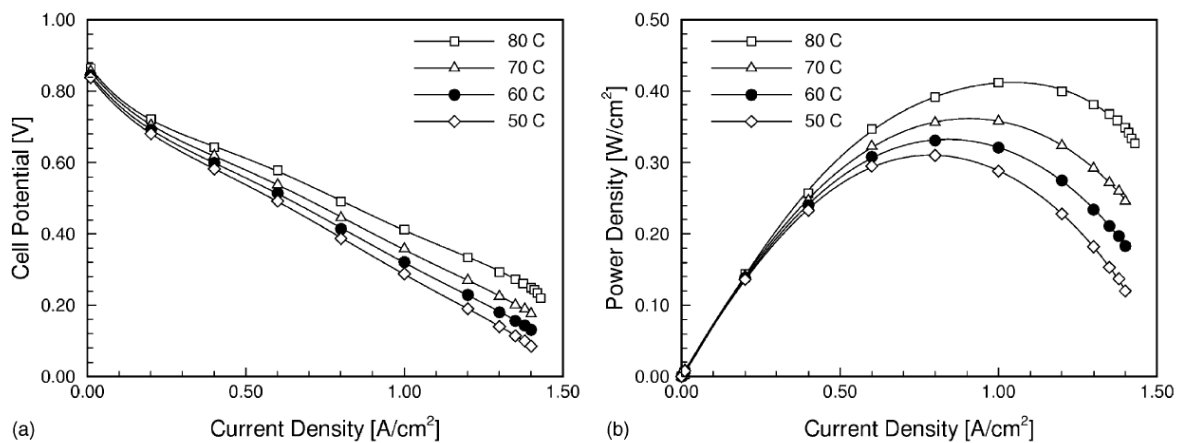
Figure 12. Predicted polarizaton curves (a) and power density curves (b) for different cell temperature, adopted from [50].

Lum and McGuirk [51] have developed a CFD model similar to the one of Shimpalee et al. [49]. They have validated the model on a global and local scale. The global validation was carried out by comparing the polarization and power curves with the experimental data. The local validation is achieved by comparing the current density distribution with the experimental data from a segmented fuel cell, as seen in Figure 13. The model data shows good agreement with the experimental data for global and local comparison. However, the relative humidity profiles along the channel length have not been compared with the experimental data. Therefore it is not clear if the model is credible in terms of water transport through the membrane.
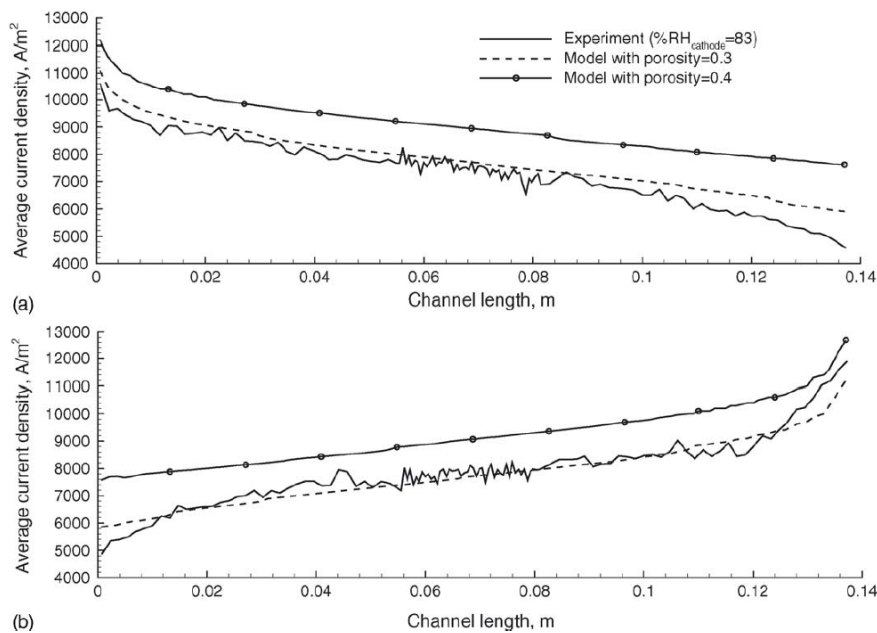
Figure 13. Comparison of local current density distribution along the cathode side of the cell of models with different porosity with experimental data, for (a) co-flow and (b) counter-flow, adopted from [51].

Ozden et al. [37] have developed a CFD model based on geometric and operating parameters from the work of Tolj et al. [8]. The CFD model was used to investigate the capability of simulating the PEM fuel cell operation with prescribed variable temperature flow field which was introduced in terms of spatially variable heat removal rates. The comparison of the modeling and experimental results was carried out for operating current density of 500 mA cm^{-2} with good agreement on a global scale, i.e. polarization curve, for isothermal and variable temperature flow field cases. However, the comparison of the relative humidity profiles along the cathode channel length with the experimental data was different, i.e. the relative humidity profiles appeared similar to the experimental results but were shifted to higher values, and the explanation for this behavior was not clear. This leads to a conclusion that the CFD models need to be verified with relative humidity profiles along the channel length, as well as the current density distribution along the cell to have a credible CFD PEM fuel cell model.

The CFD modeling of PEM fuel cell stacks has only been done by a couple of researchers, due to high computational requirements and convergence issues involved in such simulations.

Liu et al. [52] have published the first work dealing with CFD simulations of a PEM fuel cell stack. However, the whole stack was dramatically simplified and modeled as a porous zone. The reactant depletion and water generation was simulated by sink and source terms, as well as the accompanying heat sources. The results of the simulations are not realistic due to the fact that the lands and channels represent a single porous domain, therefore the relative humidity distribution along the entire flow field is not correct. Since the membrane water content is a function of the relative humidity of the reactants, it is also not correct, as well as the current density distribution along the entire flow field. It is interesting to see that the polarization curve prediction of the CFD model is very good when compared to the experimental polarization curve. This leads to a conclusion that in order to develop a credible model, it is a must to have local parameter validation. This work shows an interesting phenomenon of slight rise in overall temperature in the cathode direction of the stack height, Figure 14.
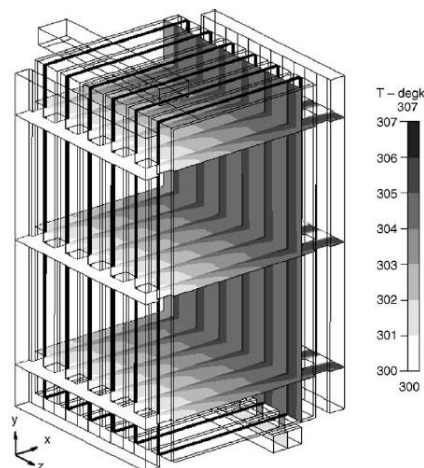
Figure 14. Temperature distribution of the fuel cell stack in yz and zx directions, adopted from [52].

Shimpalee et al. [53] have carried out CFD simulations for a six cell portable, air-cooled PEM fuel cell stack. The results of the simulations have been compared with experimental data on a global scale, i.e. polarization curves, for each of the cells in the stack. The simulation results have shown good agreement with experimental results. It is noted that the top and bottom cell of the stack shows the highest performance, while the cells in the center show lower performance. The stoichiometry of the reactants was quite high, in order of 4-5. Different performance of the cells in the stack is not elaborated in detail. The fact

that the top and bottom cell show the highest performance can be clearly attributed to higher heat removal rates due to the presence of thick aluminum blocks on the experimental installation, however it is unclear how this was achieved numerically since the requirement for such numerical results requires defining heat sinks at the top and bottom of the stack, or prescribing fixed temperature boundary conditions would be non-physical for this case, and the boundary conditions of such types have not been mentioned. The clear indication of this work is that the operating parameters show non-uniformity along the stack height as well as along the flow field of each cell, therefore it is required to simulate operation of more than one single cell to get insight in the performance of the whole stack.

Macedo-Valencia et al. [54] have carried out CFD simulations for a five cell PEM fuel cell stack. The agreement with the experimental results is not as good as in the work of Shimpalee et al. [53]. The temperature gradient is visible along the stack height, with slightly higher temperature in the cathode direction, Figure 15, but the end plates seem to be of similar temperatures, probably due to prescribed fixed temperature boundary conditions along the current collector surfaces, instead of adiabatic walls or a fixed heat flux, since the fixed temperature boundary condition in this case would be non-physical. The boundary conditions on the current collectors are not specified in this work, and it is simply noted that this behavior is less eminent for higher electric potentials, i.e. lower electrical currents.
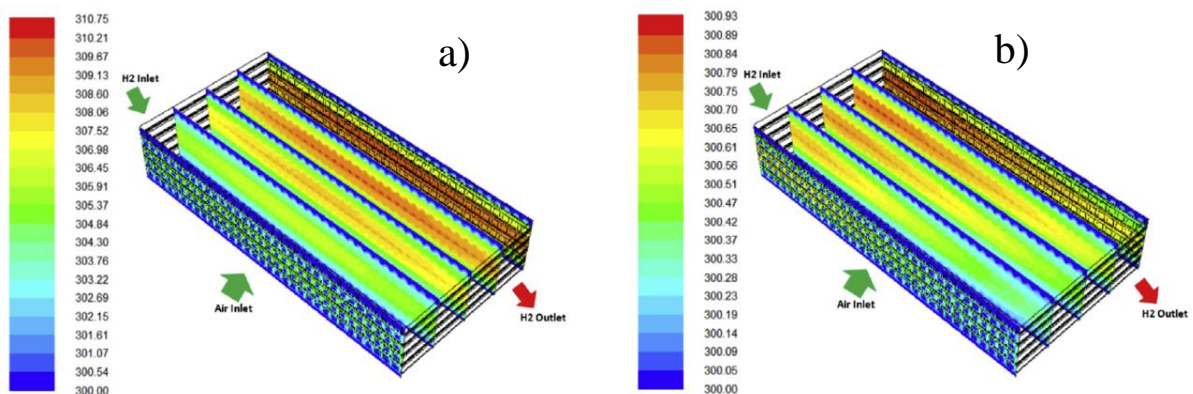
Figure 15. Temperature distributions (K) along the PEM fuel cell stack width at a) 0.6 V and b) 0.8 V, adopted from [54].

3.3.1 Conclusions

Computational fluid dynamics are a very useful tool for insight in the parameter distributions inside the operating PEM fuel cell. The literature survey shows that the various commercially used software have good capability for predicting PEM fuel cell performance, however the main requirement for development of a credible CFD model is to have experimental results which can be used to validation of the model. However, the global parameters commonly used in PEM fuel cell society, such as the polarization curves and power curves, are not sufficient for validation of the CFD model. To validate the model, one must also consider the local parameter distributions, such as current density and relative humidity along the entire flow field. The conclusion is that in order to develop a robust and credible CFD model, a robust experimental installation is required which will enable the measurement of operating parameters locally, namely current density, relative humidity and temperature. This leads to the requirement for development of a segmented PEM fuel cell. It is interesting to see that none of the CFD modeling works in the literature deal with analysis of PEM fuel cell operation under prescribed variable temperature flow field by means of mass flow rate control of the coolant.

3.4   Segmented PEM fuel cell

In order to have insight in the local distribution of operating parameters, such as current density, relative humidity and temperature, it is required to design a segmented PEM fuel cell. Segmented cell represents a single PEM fuel cell which is assembled of a certain number of smaller parts, i.e. segments. Each of the segments is connected in parallel electrically and in series in respect to the flow of the reactants. The total operating current is sum of electrical currents on each segment, while the reactants enter each segment with the species concentration, relative humidity and temperature determined by the inlet parameters of the reactants as well as the electrochemical and thermodynamics aspects which are a consequence of the reactant passage through the previous segment – the one closer to the inlet in respect to the reactant, be it anode or cathode and co-flow or counter-flow configuration. The bipolar plates are composed of a number of segments which are insulated electrically and thermally from the neighboring segments and connected to a data acquisition instrument. The segments are then connected electrically together to a common

current collector in order to enable measurement of electrical current, and in some cases temperature, of each segment. Additionally, relative humidity and temperature sensors can be placed between the neighboring segments to give insight in the temperature and relative humidity of the reactants from both sides of the membrane, the anode and the cathode. If such segmented fuel cell is assembled, it can be used for thorough validation of a developed CFD model for different sets of input parameters. Once the CFD model is developed and validated with high credibility, i.e. good agreement of global and local parameters, it can be used for studying the effect of using different flow field configurations, gas diffusion layers, catalyst layers and membranes and operating parameters on PEM fuel cell performance. Since there are many works dealing with segmented PEM fuel cells, only a few of them will be addressed in this chapter, since the goal of the research is to design a segmented fuel cell which will enable measurement of relative humidity profiles, temperature profiles and current density along the entire flow field. Also, since variable temperature flow field is of interest in this work, a method for establishing a variable temperature flow field in such setup will be discussed.

Tolj et al. [8] have developed a segmented PEM fuel cell with capability of measuring the relative humidity distributions along the cathode side of the cell. The segmented cell consisted of five single cells connected electrically in parallel, and in series in respect to the reactant flow, Figure 16.
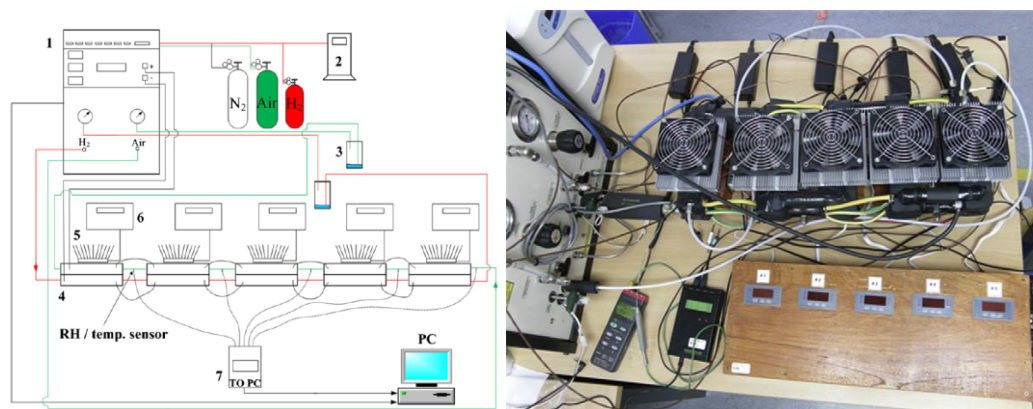
Figure 16. Left - Schematic setup of experimental segmented fuel cell: (1) fuel cell test station; (2) hydrogen generator; (3) water trap; (4) fuel cell segment; (5) Peltier thermoelement; (6) temperature controller; (7) data acquisition for relative humidity and temperature sensors. Right – Experimental setup, adopted from [8].

The reactants enter the first segment with prescribed conditions: stoichiometry, absolute pressure, temperature and relative humidity. After passing through the segment, a part of the reactants will be depleted, and a certain amount of water will be generated. This will result in different relative humidity and temperature of the reactants, as well as different concentration of the oxidant and fuel on the outlet from the segment. Reactants with such composition enter the next segment, etc. The interesting detail about this work is the study of influence of a variable temperature flow field on PEM fuel cell performance. The temperature of each segment was regulated by Peltier thermoelements placed on the cathode side of the cell. The prescribed temperature profile was adjusted to resemble water vapor saturation temperature from Mollier's h-x chart for the calculated amount of generated water. The experimental results have shown that it is possible to achieve high performance of the cell without the necessity for external humidification, with dry hydrogen supply on the anode and ambient air supply on the cathode. However, the relative humidity along the anode side was not measured, and the temperature on the anode side was not regulated by Peltier thermoelements, therefore the water transport through the membrane could not be investigated. The experimental setup with five separate cells also resulted in condensation of the water vapor between each of the segments since the insulation was not sufficient to avoid this problem. The condensation of water vapor created problems during measurements since the relative humidity and temperature sensors had to be dried before and after each set of measurements.

Yin et al. [26] have developed a segmented PEM fuel cell recently with capability of measuring current density, relative humidity and temperature along the cell with parallel channels, Figure 17. The copper current collectors are gold plated and of a printed circuit board type, and the temperature profile is regulated by the mass flow rate control of the coolant fluid.
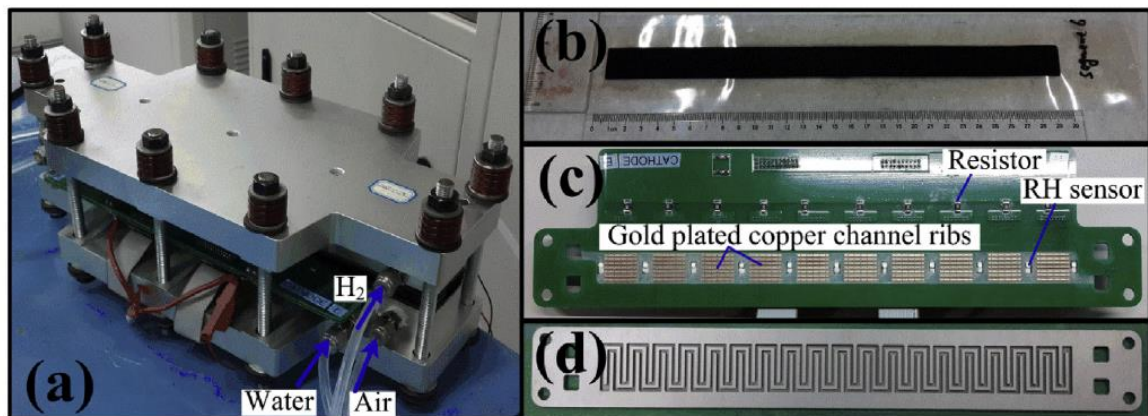
Figure 17. Segmented fuel cell with its main components: (a) segmented fuel cell assembly; (b) MEA; (c) reactant distribution plate based on multi-layered printed-circuit board plate with current and relative humidity sensors; (d) coolant water graphite plate with serpentine flow channels, adopted from [26].

The flow configuration in their study is co-flow between the reactants and the coolant. This design would be very suitable for developing a robust and credible CFD model, since it also gives insight in the membrane water transport, therefore the effort of this work is to develop similar concept. However, to maximize the performance of the cell in the work of Yin et al. [26] it would be advisable to set the reactants in counter-flow, and the coolant in co-flow with the cathode air, to use parallel channels for the coolant instead of serpentines, and to prescribe the temperature profile using Mollier's *h-x* chart, as done in the work of Tolj et al. [8].

3.4.1 Conclusions

Segmented PEM fuel cell is the most suitable experimental setup for developing a robust CFD model with capability of predicting PEM fuel cell performance for various configurations of operating and structural parameters. The segmented PEM fuel cell will need to have capability of measuring the current density, relative humidity and temperature distribution along the entire flow field. The segmented cell can then be used to develop a CFD model for variable temperature flow field to maximize the performance of the cell fed with dry hydrogen and ambient air, where the temperature profile can be prescribed for different operating current densities. The desired temperature profile can be extracted from Mollier's *h-x* chart for the calculated amount of generated water.

4 HYPOTHESIS

It is possible to establish and maintain variable temperature flow field along the active area of PEM fuel cell which will closely resemble the water vapor saturation temperature profile extracted from Mollier's *h-x* chart.

The temperature profile will be established and maintained by gradually increasing the temperature of the coolant fluid during the passage through the cell. In such manner, the heat generated as a result of the electrochemical reaction of hydrogen and oxygen in the cathode catalyst layer, will be used for gradually increasing the temperature of the coolant in the cathode downstream direction, while the generated water will be used for internal humidification of the reactants.

If the concept proves feasible, the variable temperature flow field will be applicable for PEM fuel cell stacks, thereby broadening the operating range of the stack, minimizing the mass transport losses and significantly reducing the complexity and economic price of the PEM fuel cell stack system.

5 COMPUTATIONAL FLUID DYNAMICS MODEL OF PEM FUEL CELL WITH SEGMENTED CURRENT COLLECTOR TERMINALS

5.1 Introduction

Water and heat produced during an electrochemical reaction inside a fuel cell can be used for internal humidification of reactant gases, without the need for external humidifiers. However, if non-humidified ambient air is introduced in an isothermal fuel cell operating at 60°C or higher, it would be heated very quickly which would result in extremely low relative humidity throughout the cathode channel, thus causing drying of the polymer in the catalyst layer and the membrane. This, in turn, would have adverse effects on fuel cell performance and durability [17]. Tolj et al. [8] proposed and investigated a concept of an imposed variable temperature profile along the cathode channel which resulted in 100% relative humidity of reactant gas throughout the most of the cathode channel without external humidification. Toyota also relied on internal water and heat management to operate the fuel cell stack in their Mirai vehicle without external humidification [7].

High relative humidity along the cathode channel results in higher ionic conductivity of the polymer membrane, as demonstrated in studies by Zawodzinski et al. [18] and Hinatsu et al. [38]. However, too much water inside the fuel cell may result in flooding of the catalyst layers, the gas diffusion layers and the channels. It would therefore be beneficial to keep relative humidity slightly less than 100% inside the fuel cell. This is only possible with adequate internal water and heat management. Water management means balancing various water fluxes, namely water generated in the electrochemical reaction on the cathode side, electroosmotic drag, *i.e.*, water flux from the anode to the cathode, and water diffusion through the membrane as a result of water concentration and pressure gradients.

Electro-osmotic drag is defined as a number of water molecules $N(H_2O)$ dragged by a single hydrogen proton passing through the membrane. Water flux induced by electro-osmotic drag is always from the anode to the cathode side of the membrane. There have been numerous studies carried out over the years to determine the correlation between

electro-osmotic drag coefficient and various operating parameters for Nafion membranes [43,55-64].

However, results of parameter correlation from different authors show high level of disagreement, although most of them follow similar trends when the dependency on different operating conditions is considered. Model predictions from various authors are considerably different in lower membrane water content (λ) intervals. Almost every numerically implemented model for determining electro-osmotic drag coefficient is dependent upon λ, which is in defined as a function of water activity, *i.e.* relative humidity. However, results from a study by Jinnouchi et al. [41] showed that electro-osmotic drag coefficient is not dependent on λ, and that it increases only slightly with increase in operating temperature. For this reason, further investigation of electro-osmotic drag coefficient in an operating PEM fuel cell is required.

Water flux resulting from a water concentration gradient across the membrane is defined as diffusion if the flux direction is from the anode to the cathode side of the membrane, and back-diffusion if the flux is in the opposite direction. In most practical applications, during the flow of an electric current, only back-diffusion is considered, because water concentration on the cathode side of the membrane is always higher. Large number of studies have been carried out in order to determine diffusion coefficient by different groups of authors [43,61,62,65-70]. Models of water diffusion through the membrane are also show significant disagreements between authors using similar initial operating parameters.

Although most of measurement results show monotonic dependency of water diffusion on λ, some models predict a relatively large spike in water diffusion for λ value of 3, which has not been physically explained so far. In work of Olesen et al. [42] this phenomena was attributed to a purely mathematical nature of derivation of fraction of natural logarithms of water activity versus natural logarithm of membrane water content – because membrane water content dependency on water activity was assumed to be a third degree polynomial with origin in zero. This is not valid after PEM fuel cell break-in procedure, because the membrane will retain a certain amount of water even if the reactants are completely dry for some period of time. Experimental methods used during the investigations were nuclear

magnetic resonance [62,65,66], transient sorption kinetics [67,68], steady-state permeation [43,61,69,70], and other non-conventional methods [15,71].

Almost every author referenced so far, when considering membrane water content, has implemented empirical expression for λ derived by Zawodzinski et al. [18]. Zawodzinski et al. have carried out experiments at operating temperature of 30 °C, which is unreasonably low when considering common PEM fuel cell operating temperatures (in ranges of 60 °C-80 °C). From this approach, one would suggest that λ would be the same for different temperatures since it has temperature already incorporated in terms of water vapor saturation pressure, which is used to calculate water activity, *i.e.* relative humidity. However, in work of Hinatsu et al. [38], λ has been measured for an operating temperature of 80 °C. The results of Hinatsu et al. [38] differ significantly for higher intervals of water activity when compared to results from Zawodzinski et al. [18], and subsequently requires further investigations.

Considering the above mentioned, altering the temperature on boundaries of a CFD model in order to achieve the desired relative humidity profile along the reactant channels (resulting in higher PEM fuel cell efficiency), has a high potential for error. In order to determine the reliability of the implemented models for water transport, in this chapter the CFD model is validated with local and global operating parameters from experiments of Tolj et al. [8], while later in chapter 7 the new experimental setup is developed and the model is thoroughly validated in chapter 8.

The major outcome of this chapter is outlining the fact that the temperature difference between reactant channels and current collector terminals is quite significant and that improper definition of higher temperature boundary conditions during the CFD analysis leads to under-prediction of the polarization curve at higher current densities.

The common CFD modeling approach is defined by prescribing a uniform temperature field on anode and cathode terminals, based on defining a single parameter of operating temperature. The temperature of an operating PEM fuel cell is higher inside the reactant channels than along the current collector terminals, and non-uniformly distributed due to

heat release induced by the electrochemical reaction of hydrogen and oxygen in the cathode catalyst layer.

Although this temperature difference is of minor importance for relatively low current densities and fully humidified reactants, in cases where higher current density is considered and where partially humidified reactants are used, this must be considered. One way of minimizing this error would be to measure the temperature along the anode and cathode terminals in more physical points. This would result in a temperature profile boundary condition and lead to a more realistic boundary condition setup, as demonstrated in this work. All of these findings led to the development of the new experimental setup in chapter 7.

5.2   Methodology

5.2.1   Experimental setup

In a previous study by Tolj et al. [8], measurements of polarization curves and relative humidity profiles along the cathode reactant channel were done using 5 single cell fuel cells (segments) connected electrically in parallel, with counter-flow setup. The results have been used to calibrate and validate the developed CFD model.

5.2.2   Domains

Geometry for the CFD model has been developed from one single cell used by Tolj et al. [8]. In order to implement segmented temperature boundary condition, and represent the experimental setup consisting of five segments, current collector terminals from anode and cathode side have been divided into five equal parts (segments), Figure 18.
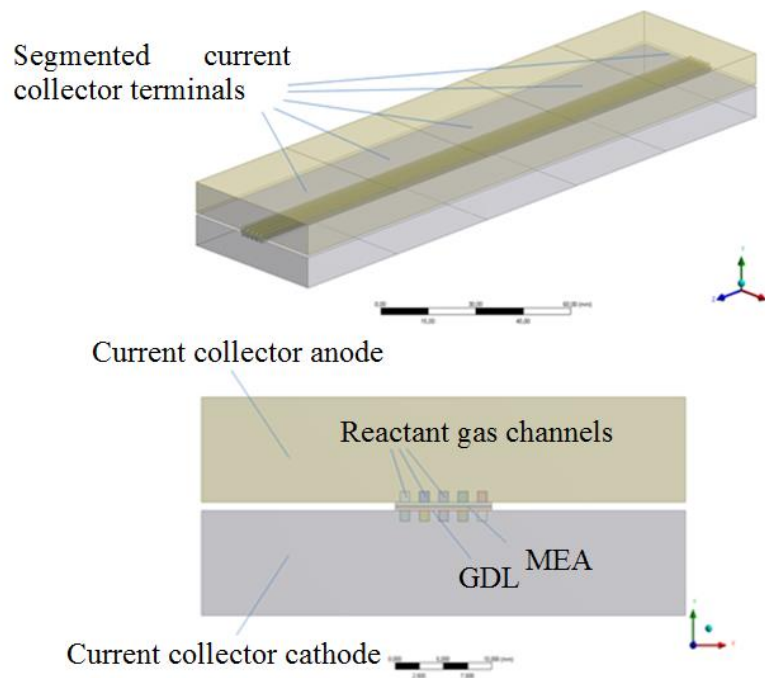
Figure 18. Numerical domains.

5.3   Mesh

In order to enable study of different physical processes inside PEM fuel cell, a grid dependency study was carried out for various mesh configurations by varying mesh type and number of finite volumes. Since the geometry is simple, and has large difference in scale size (edge length span from 10 μm – catalyst layer thickness, to 0.2 m – axial length of PEM fuel cell), it was most convenient to use a structured hexahedral mesh, *i.e.* Cartesian grid.

During the calculations, convergence monitors have been defined to give insight in the convergence history of average current density on the cathode terminals, as well as the average relative humidity on anode and cathode inlets and outlets. In order to achieve a grid independent solution, the number of mesh sub-divisions has been varied considerably. After achieving a grid independent solution for an average current density close to 500 mA cm^{-2}, the relative humidity profile along the cathode channel length has been compared to

experimental results with good agreement. Total number of finite volumes was 1.547 million.

A comparison of mesh setup with the one used in work by Arvay [72] showed a similar number of edge sub-divisions for all domains besides the reactant channels. In this work, a higher number of finite volumes in the channels have been used to give a better representation of the relative humidity profiles along the cathode channel.

5.4   Governing equations and boundary conditions

Numerical calculations were carried out using ANSYS Fluent 16.2 PEM fuel cell Module. The operating parameters used in the setup are shown in Table 1. The parameters used for the model calibration were open-circuit voltage of 0.91 V, implemented from the work of Tolj et al. [8], and the cathode reference current density for the operating current density of 500 mA cm^{-2}. The resulting value for cathode reference current density used during the simulations was 0.0155 A m^{-2}. The remaining material parameters are retained on the default values in PEM Fuel Cell Module, because the data was not provided by the MEA manufacturer. Solution control and recommended parameters are implemented from the manual [12]. The novelty of this work is the implementation of segmented temperature profiles which enables the study of PEM fuel cell operating parameters for different applied temperature profiles, *i.e.* temperature gradients.

Table 1. Operating parameters

Parameter	Value
Cathode stream abs. pressure	1.01325 bar
Anode stream abs. pressure	1.01325 bar
Cathode stream inlet temperature	30 °C
Anode stream inlet temperature	25 °C
Fuel cell hardware temperature	60°C or variable
Relative humidity of cathode stream inlet	75%
Relative humidity of anode stream inlet	dry
Current density	500 mA cm^{-2}
Stoichiometry, cathode	2.15
Stoichiometry, anode	1.2
Reactant straight channel length	200 mm
Channel width at anode and cathode	1 mm
Channel height at anode and cathode	1 mm
Membrane thickness (Nafion 212)	0.05 mm and 0.01 mm
Catalyst layer thickness	0.01 mm
Platinum loading	0.5 mg cm^{-2}
Gas-diffusion layer thickness	0.38 mm
Effective area	2000 mm
Membrane dry density	2 g cm^{-3}
Membrane molecular weight	1100 g mol^{-1}

The governing equations are based on mass, momentum, energy and species conservations including appropriate source terms described in the manual [12]. The type of analysis used was steady-state and single-phase, including equations for Joule heating, reaction heating, electrochemistry sources, Butler-Volmer rate and membrane water transport. Water transport equations consist of an equation for electro-osmotic drag coefficient by Springer et al. [15] and diffusion equations by Motupally et al. [43] for different membrane water content intervals. The membrane water content equation used in the software was adopted from Zawodzinski et al. [18].

The governing equations of Fluent PEM fuel cell module are based on energy, mass, momentum and species conservation including appropriate sink and source terms [12]. For

steady-state simulations, time dependent parameters are omitted from the equations. The resulting equations, as shown previously in chapter 2.3, are:

5.4.1 Continuity

$$\nabla\left(\rho\vec{V}\right) = S_{\mathrm{mass}} \tag{35}$$

Where S_{mass} represents the source term for the continuity equation. This term is only applicable for the triple-phase boundary (catalyst) regions. Inside the gas channels, gas-diffusion layers and the membrane, the source term S_{mass} is set to zero.

5.4.2 Momentum

$$\frac{1}{s(1-s)}\nabla\left(\rho\,\vec{V}\vec{V}\right) = -\nabla p + \frac{1}{s(1-s)}\nabla\left(\mu\,\nabla\vec{V}\right) + \rho g + S_{\mathrm{mom}} \tag{36}$$

Where S_{mom} represents the source term for momentum equation and applies only for the porous medium. For other domains, S_{mom} is set to zero.

5.4.3 Species

$$\nabla\left(\rho\,\vec{V}X_{\mathrm{i}}\right) = -\nabla(\rho D_{\mathrm{i}}\nabla X_{\mathrm{i}}) + S_{\mathrm{i}} \tag{37}$$

where index i represents different species – oxygen, hydrogen and water vapor. S_{i} represents the source and sink term for the species inside the catalyst layers and accounts for the reactant consumption in anode and cathode catalyst layers and water generation inside the cathode catalyst layer. In other domains, S_{i} is set to zero.

5.4.4 Energy

$$\nabla\left(\rho\,\vec{V}T\right) = \nabla\left(k^{\mathrm{eff}}\nabla T\right) + S_{\mathrm{T}} \tag{38}$$

where S_{T} represents the heat source term for the energy equation. S_{T} applies only for the cathode catalyst layer, for other domains it is set to zero.

5.4.5 Water transport through the membrane

Electro-osmotic drag represents the water flux from the anode to the cathode side, and is defined by expression

$$n_\text{d} = \frac{2.5\lambda}{22} \tag{25}$$

where n_d represents electro-osmotic drag coefficient, and λ represents membrane water content, defined as

$$\lambda = 0.043 + 17.18a - 39.85a^2 + 36a^3 \quad a < 1 \tag{28}$$

$$\lambda = 14 + 1.4(a - 1) \quad a \geq 1$$

Where a represents water activity, defined as

$$a = \frac{p_\text{wv}}{p_\text{sat}} + 2s \tag{29}$$

Where p_wv represents water vapor pressure, and p_sat represents water vapor saturation pressure. Since the model is single phase, the Leverett function term $2s$ is set to zero.

Back-diffusion flux J_w^diff is defined as

$$J_\text{w}^\text{diff} = -\frac{\rho_\text{m}}{M_\text{m}} M_{\text{H}_2\text{O}} D_\text{l} \nabla \lambda \tag{26}$$

Where ρ_m and M_m represent density and the equivalent weight of the dry membrane, respectively. The term D_l represents membrane water diffusivity, defined as

$$D_\text{l} = 3.1 \times 10^{-7}\lambda\left(e^{0.28\lambda} - 1\right)\left(e^{-\frac{2346\,[K]}{T}}\right) \quad \lambda < 3 \tag{27}$$

$$D_\text{l} = 4.17e \times 10^{-8}\lambda\left(1 + 161e^{-\lambda}\right)\left(e^{-\frac{2346\,[K]}{T}}\right) \quad \lambda \geq 3$$

5.4.6 Domain boundary conditions

The domain type for all domains is defined as fluid bodies, except for current collectors which are defined as solid bodies. In work of Tolj et al. [8] the current collector material was stainless steel 316L, therefore this material was selected in this study as well.

It has been shown that the thermal conductivity of the current collector material has a significant influence on relative humidity profile along the channel. Thermal conductivity affects the heat transfer rate between the reactant channels which are at higher temperature, and the current collector terminals, which are at lower temperature. Application of current collector materials with low thermal conductivity results in a higher temperature difference between the channels and terminals. Reduction in heat transfer between the channels and terminals results in a temperature gradient and reduced relative humidity profile along the entire channel length. The temperature along the channel length determines the water vapor saturation pressure. Therefore it has a direct influence on relative humidity distribution along the channel, as well as PEM fuel cell efficiency.

5.4.7 Inlet boundary conditions

The mass flow inlet boundary condition is defined for anode and cathode inlets. The anode inlet hydrogen temperature was set to 25 °C, with a relative humidity of 0%. Cathode inlet air temperature was set to 30 °C, with a relative humidity of 75%. The anode mixture of gases consisted of hydrogen and water vapor (while the mass fraction of water vapor was set on zero on the anode inlet), the cathode mixture of gases consisted of nitrogen, oxygen and water vapor.

5.4.8 Outlet boundary conditions

On the anode and cathode reactant channel outlets, the pressure outlet boundary condition is applied with a zero gauge pressure and backflow total temperature set according to the temperature field setup.

5.4.9 Wall boundary conditions

Non-slip boundary conditions were applied to the walls. The temperature was fixed on segmented terminals of the anode and cathode current collectors for isothermal and non-uniform temperature field. The electric potential on the anode terminals was set to zero. On the cathode terminals different values of electric potential are defined in order to extract the polarization curve. The remaining surfaces are defined as walls by default.

5.5 Results and discussions

Isothermal case experimental results for the polarization curve and relative humidity profile along the cathode channel are used for model calibration. The calibration consisted of achieving grid independent solution and defining appropriate material properties of current collectors.

In the work of Ozden et al. [37], the analysis was done for similar isothermal setup, with difference from experimental setup by Tolj et al. [8] by using aluminum as current collector. In that work, the analysis was done for an electric potential of 0.548 V, resulting in a current density close to 500 mA cm^{-2}. The simulated operating point has shown good agreement compared with experimental results of polarization curve from Tolj et al. [8], while the difference in the relative humidity profile along the cathode channel was notably contrasted.

The first step during the calibration of the developed model was to compare the operating point and the relative humidity profile with the results reported in [37] when aluminum is used as current collector. It was found that the results are in good agreement.

5.5.1 Influence of thermal conductivity of current collectors on relative humidity distribution along the reactant channels

After altering the current collector material properties to represent stainless steel 316L, the numerical simulation results have shown higher level of agreement of relative humidity profile along the cathode channel when compared with experimental data from Tolj et al. [8]. It is found that the thermal conductivity has significant influence on the relative humidity distribution. Since the thermal conductivity of the current collector material used by Tolj et al. [8] was not measured experimentally, and knowing that the thermal conductivity of 316L ranges from 12-17 W m^{-1} K^{-1}, the best agreement with experimental data is achieved with a thermal conductivity of 13 W m^{-1} K^{-1}, as shown in Figure 19. The relative humidity profiles, shown in Figure 19., represent the area-weighted average values for the cathode channel cross sections. The values of relative humidity from CFD simulations are extracted for cross sections defined every 5% of the channel length.
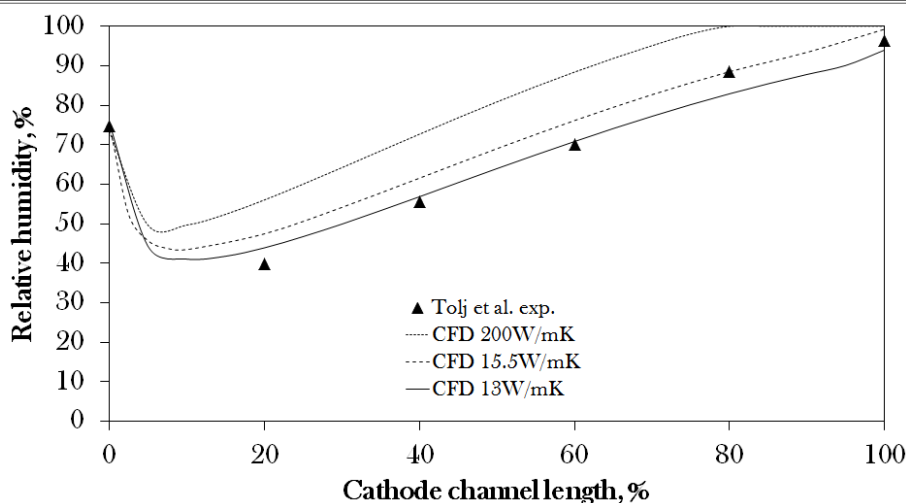
Figure 19. Effect of different thermal conductivity of current collectors on relative humidity distribution along the cathode channels.

In order to explain this behavior, several things must be considered. Aluminum has a higher thermal conductivity than stainless steel (200 W m^{-1} K^{-1} for aluminum, vs. 12-17 W m^{-1} K^{-1} for stainless steel). The relative humidity for a fixed mass flow and pressure depends only on temperature, since water vapor saturation pressure is only a function of temperature. For a fixed mass flow and pressure, increasing the temperature along the reactant channels results in a reduction of relative humidity profile along the channel, and vice versa.

If the temperature is fixed on the terminals, it is clear that higher temperature along the reactant channels must be primarily caused by heat release during electrochemical reactions inside the cathode catalyst layer. This leads to a conclusion that in order to determine the relative humidity profile along the channel length properly during CFD analysis, it is important to apply realistic boundary conditions for temperature on the anode and cathode terminals. In order to define realistic temperatures on terminals, they would need to be measured experimentally. Measuring the terminal temperature is especially important when current collector materials with low thermal conductivity are used (*e.g.* stainless steel, graphite, titanium). In this chapter, it is shown that the temperature, for isothermal boundary condition setup, is higher inside reactant channels from 3-5 K when compared to the terminal temperature for current density close to 500 mA cm^{-2}. The

temperature difference between the current collectors and channels increases proportionally with the increase in the operating current density.

5.6   Model validation

In order to determine the influence of different temperature flow field configurations on PEM fuel cell performance, two fixed temperature flow fields on anode and cathode terminals are studied (anode and cathode side have identical configuration). The first was uniform temperature field, or the so-called isothermal, and the other was non-uniform temperature field. The non-uniform temperature flow field is different from the variable temperature flow field in terms that the non-uniform temperature flow field represents segmented current collectors with prescribed fixed temperatures on each segment, while the variable temperature flow field is slightly different along the entire length of the cell, *i.e.* the current collectors are not segmented. To determine how accurately the model predicts PEM fuel cell performance, the simulation results were compared with the experimental ones from the study of Tolj et al. [8], since at the time the new experimental setup was not available.

5.6.1   Polarization curves

The comparison of the simulated operating points with the associated experimental polarization curves is done for two different temperature fields. During the simulation setup, potentiostatic boundary conditions were applied by defining electric potential of 0 V on the anode and a fixed electric potential for each calculation on the cathode terminals. In Figure 20. It can be seen that CFD prediction of polarization curve for isothermal case for the 50 μm membrane is quite good. At higher current densities it can be seen that CFD slightly under-predicts current density when comparing to the experimental results for both temperature fields.
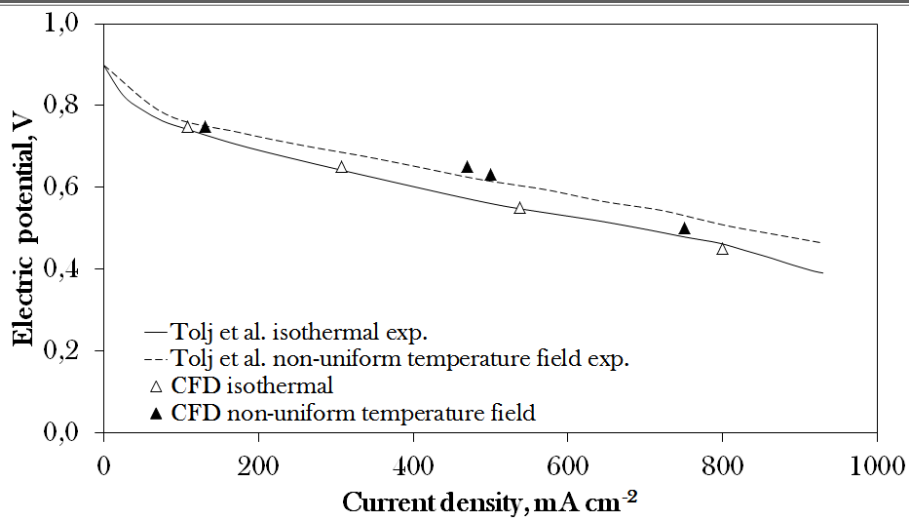
Figure 20. Polarization curve comparison.

The reason for this is that at higher current densities, more heat is released during the electrochemical reaction inside the cathode catalyst layer. This results in a higher temperature along the reactant channels than that defined on the current collector terminals. With an increase in temperature, for fixed mass flow and ambient pressure, the relative humidity is decreased, resulting in decreasing of the membrane water content (λ). Since the membrane ionic conductivity is proportional to λ, decrease in relative humidity results in a decrease of ionic conductivity of the membrane, *i.e.* higher ohmic losses.

The temperature difference between the channels and current collector terminals is more pronounced in non-uniform temperature field case, where fixed temperature of terminals is overall lower (35 °C-59 °C) when compared to isothermal case. Heat release inside the cathode catalyst layer in non-uniform temperature field case has a higher relative influence on PEM fuel cell performance drop at higher current densities – resulting in increased heat release, since higher temperature results in lower relative humidity of the reactant gases. This can be accounted for by slightly lowering the terminal temperature on higher current densities to prescribe the desired temperature profile along the channels.

Additionally, for non-uniform temperature field there is a difference between the temperatures of the anode and cathode reactants along the entire channel length. This is due to much higher mass flow rate of air, compared to hydrogen, resulting in slower heating of the cathode air. The cathode air temperature consequently increases at a lower

rate than the temperature of the anode hydrogen. Therefore, the temperature along the anode channel is higher. Since the heat is released inside the cathode catalyst layer, it would be expected that the cathode channel has higher temperature, but not in this case.

5.6.2 Relative humidity distribution

The relative humidity distribution along the reactant channels directly influences PEM fuel cell performance. In the work of Tolj et al. [8], the relative humidity distribution and temperature were measured at the inlet and outlet of cathode channels of each segment, making a total of six measurements along the entire channel length. Measurements for anode side of PEM fuel cell and the current density distribution along the cell length were not performed in the work of Tolj et al. [8]. However, these measurements were later carried out on a new experimental setup, chapter 7.

In Figure 21. it can be seen that the CFD results show good agreement with experimental ones for the relative humidity distribution along the cathode channel for a 50 μm membrane.
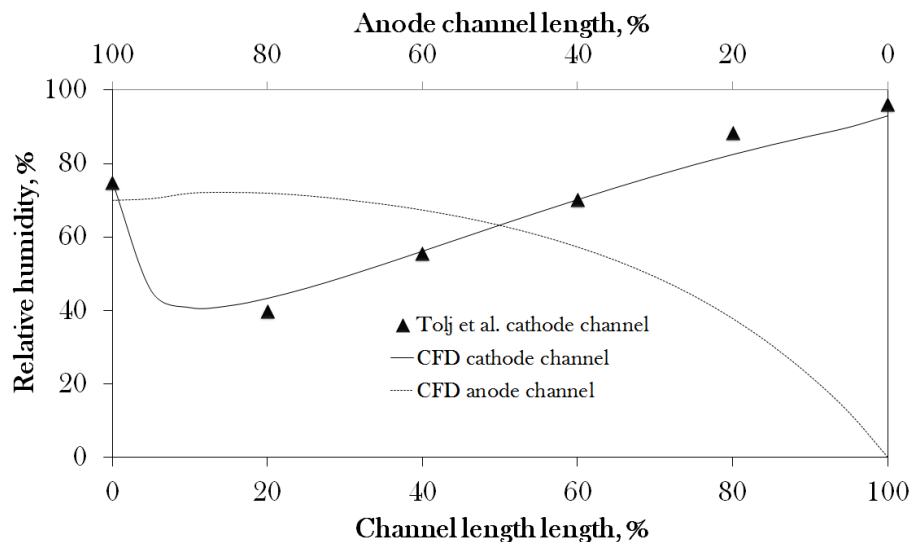
Figure 21. Relative humidity distribution along anode and cathode channel length, isothermal case for current density of 550 mA cm⁻².

In Figure 22. the relative humidity distributions are shown for non-uniform temperature field case. In order to maintain the temperature profiles inside the channels close to the

experimental ones presented in [8], proper boundary conditions for the temperature were applied. As a result, the CFD results of the relative humidity in the cathode channel are in accordance with the experimental data.
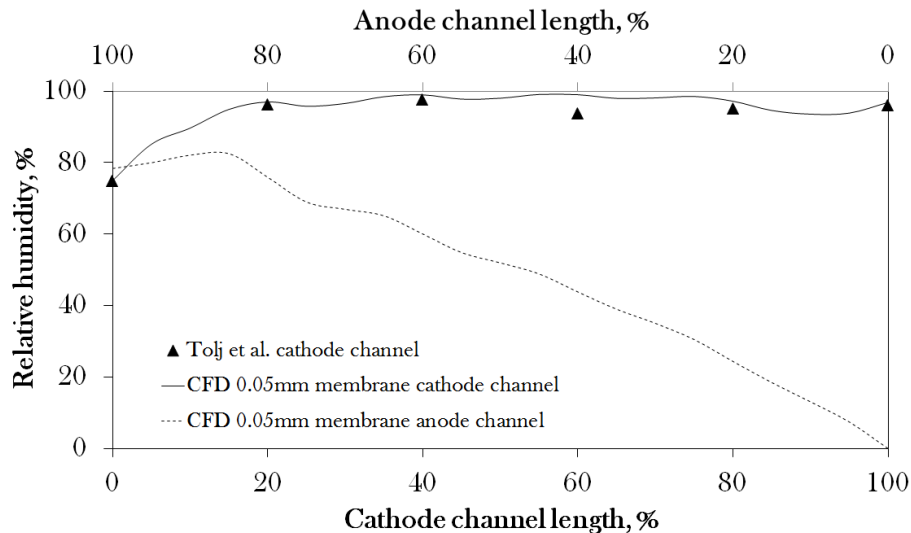
Figure 22. Relative humidity distribution along anode and cathode channel length, non-uniform temperature field case for current density of 550 mA cm^{-2}.

5.6.3 Temperature distribution along the reactant channels

It is not clear what the term operating temperature of PEM fuel cell represents, especially if the term "isothermal" setup is being used. Most informative way to define PEM fuel cell temperature would be to define a temperature profile along the reactant channels. However it is difficult to measure the temperature along the reactant channels because the method is intrusive.

For this reason, some authors define the temperature of the fuel cell as the averaged outlet temperature of coolant fluid. This is justified if the coolant is characterized by a high specific heat and mass flow rate, and its temperature gradient over the entire flow field is relatively small. The coolant outlet temperature approach is relatively simple and gives some overall definition of PEM fuel cell temperature. The problem with coolant outlet temperature is that this temperature is close to an averaged value between the channel and terminal temperature, which is not very useful for CFD applications.

Measuring temperature on terminal boundaries would be more effective for CFD modeling applications. It enables setting up proper boundary condition values. However, the temperature profiles along the reactant channels are still uncertain. Since the commonly used materials for current collectors have low thermal conductivity, temperature along channels is always higher than on the terminals if the outer walls are defined as adiabatic during the CFD model setup.

In order to gain insight in prediction capabilities of CFD model analysis, it would be most convenient to measure temperature on the terminals, as well as relative humidity and temperature inside the reactant channels. This would resolve large number of uncertainties regarding setup of proper temperature boundary conditions and give a more detailed insight in water transport through the membrane. This is later resolved on a new experimental setup, presented in chapter 7.

In this chapter, terms isothermal and non-uniform temperature field are used to describe temperature boundary conditions on anode and cathode segmented terminals, since temperature field inside an operating fuel cell is certainly not isothermal. During the CFD analysis, temperature was fixed on anode and cathode terminals, and the rest of the temperature field was calculated numerically.

In Figure 23., it can be seen that for fixed terminal temperature of 60 °C or 333 K on the anode and the cathode terminals for the so-called isothermal setup, temperature along reactant channels is overall higher than terminal temperature, except in vicinity of the inlets.
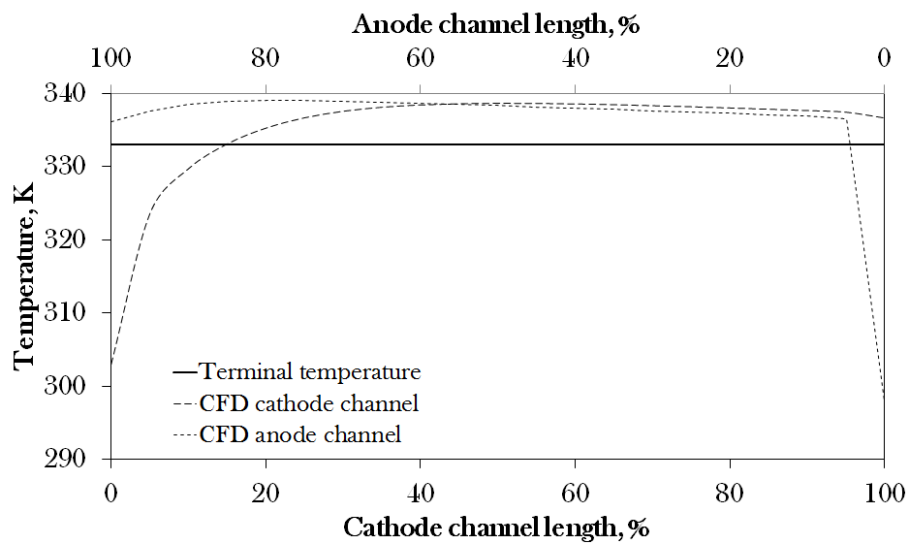
Figure 23. Temperature distribution along terminals and reactant channels for current density of 550 mA cm^{-2}, isothermal case.

This leads to difficulties during proper setup of CFD analysis which would represent realistic operating parameters of PEM fuel cell from which experimental data has been extracted. During the CFD setup, terminal temperature or terminal heat flux must be defined, which is unknown in this case because temperature has only been measured along the cathode channel length.

In Figure 23. it can be seen that hydrogen temperature almost instantly increases to approximately constant value along the entire channel, while temperature of air increases more slowly, due to the fact that air mass flow is much higher (even though hydrogen has a much higher specific heat).

Definition of terminal segment temperature during non-uniform temperature field setup consisted of setting up initial temperature field and gradually reducing temperature on each segment to a certain extent and double-checking the resulting temperature profile versus temperature profile defined by Tolj et al. [8] along the cathode channel length. In Figure 24. it can be seen that the terminal temperature profile is overall lower by up to 5 K when compared to Tolj et al. [8] segmented temperature profile (derived from Mollier's *h-x* chart).
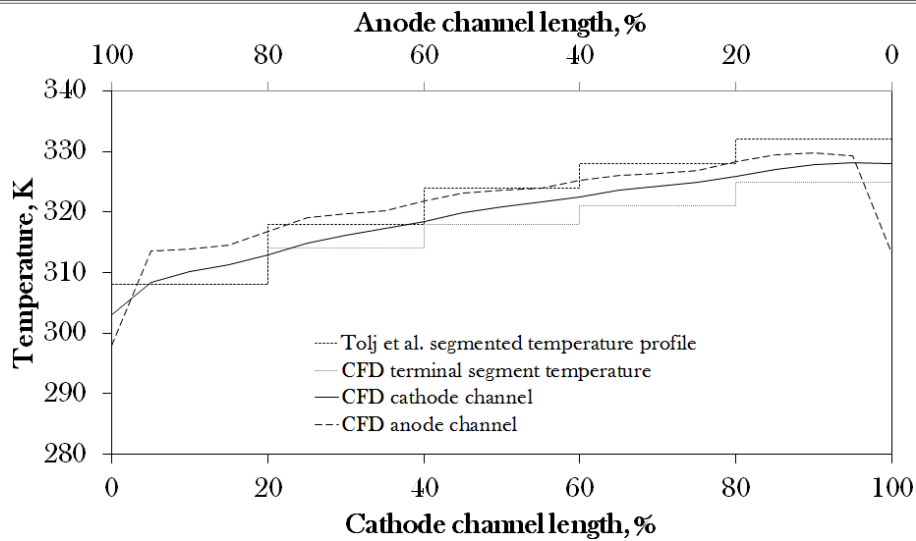
Figure 24. Temperature distribution along terminals and reactant channels for 50μm membrane, non-uniform temperature field case for current density of 550 mA cm^{-2}.

From non-uniform temperature field CFD study, it can be seen that there is an overall difference between temperatures of anode and cathode reactant gases due to a large difference in mass flow rates. Since air mass flow rate is much higher than mass flow rate of hydrogen, temperature of air increases slower than temperature of hydrogen along the entire channel length, even though heat is released during electrochemical reaction inside the cathode catalyst layer.

Temperature difference between anode and cathode reactant gases, as well as terminals, leads to a conclusion that in order to study water and heat transfer in detail, both anode and cathode temperature and relative humidity must be measured along the channels and on terminals as well.

It is clear that setting up non-uniform temperature profile is challenging both numerically and experimentally. Practical way of setting up non-uniform temperature profile on a single cell, or a stack, would be by defining sufficiently low mass flow rate of the coolant fluid, which would enter the fuel cell at certain temperature and gradually heat up during the passage through the cell. This is done in chapter 6.

5.7 Investigation of a thinner membrane

In order to determine the influence of thinner membrane (10 μm) on PEM fuel cell performance, simulations are carried out for identical operating conditions used in the 50 μm membrane study. Figure 25. shows that thinner membrane results in notably higher operating voltage for isothermal and non-uniform temperature field setups, thereby improving overall performance of the cell.
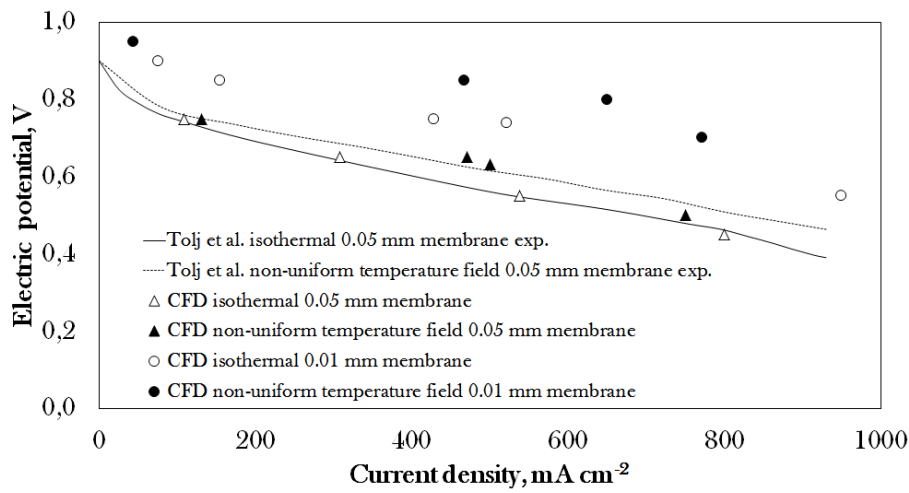
Figure 25. Polarization curve comparison for different membranes.

The performance gain is a result of lower ohmic resistance of the thinner membrane, as well as better hydration of the anode hydrogen due to increased back-diffusion.

In Figure 26. it can be seen that relative humidity profile for the thinner membrane along the reactant channel length is notably different. Thinner membrane results in higher back-diffusion, therefore the relative humidity profile along the anode channel is higher. For the same operating conditions and temperature profile on terminals used in the 50 μm simulations, it would be expected to see a slight decrease of relative humidity profile along the cathode channel. However, relative humidity profile along the cathode channel is higher for the thinner membrane for this particular isothermal case.
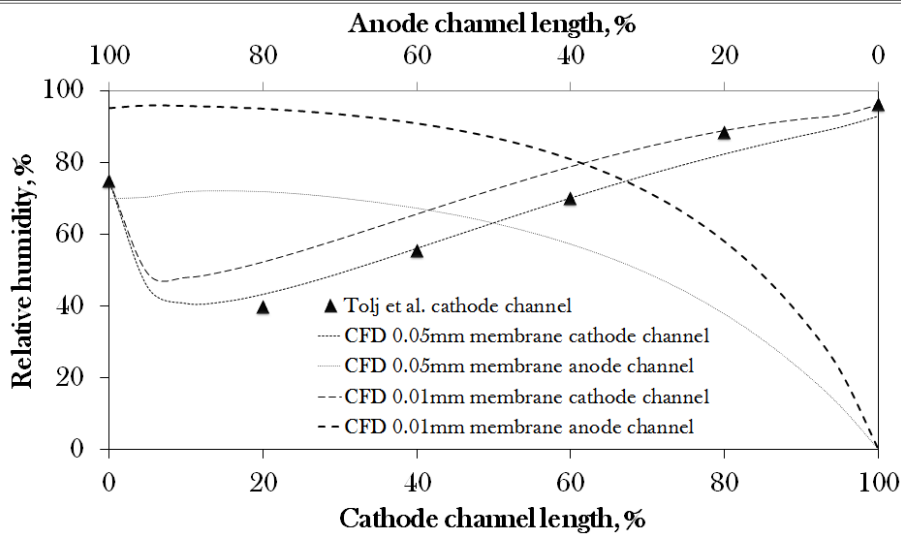
Figure 26. Relative humidity distribution along anode and cathode channel length, isothermal temperature field case, different membranes, for current density of 550 mA cm⁻².

The reason for this can be seen in Figure 27., which shows that this is simply caused by lower temperature profile along the channels for the thinner membrane case. Even though the back-diffusion results in higher water flux from the cathode to the anode side, lower temperature profile results in overall higher relative humidity profiles for both sides. For this reason reduction in the actual water content on the cathode side cannot be seen from relative humidity profile shown in Figure 28. Lower temperature profile along the channels is a result of higher operating voltage for the thinner membrane, *i.e.* lower waste heat generation.
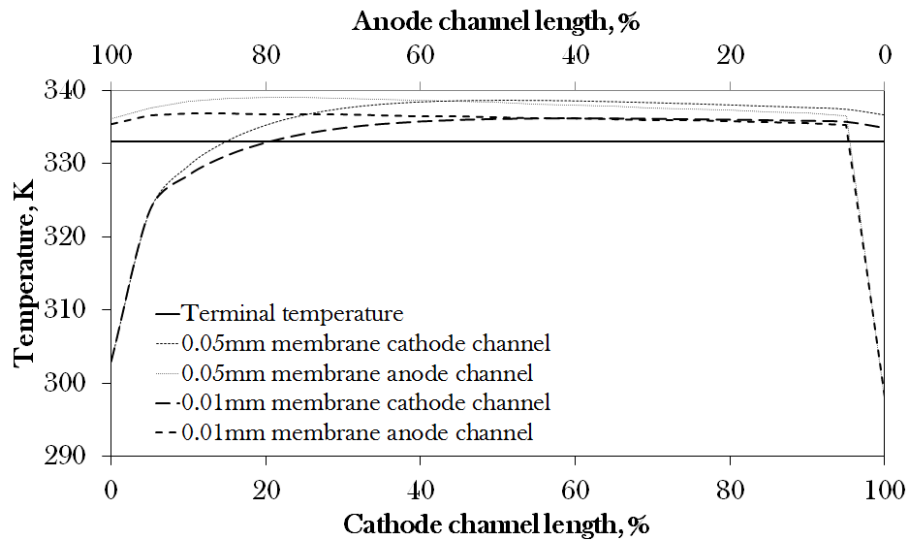
Figure 27. Temperature distribution along terminals and reactant channels for current density of 550 mA cm^{-2}, different membranes, isothermal case.

The effect of back-diffusion on relative humidity profile is more pronounced in non-uniform temperature field case. Figure 28. shows that relative humidity profile along the anode channel is higher, and along the cathode channel is lower, as expected to be. In order to establish close to 100% relative humidity along the cathode channel, the temperature profile on cathode terminals has to be slightly reduced.

Decrease in temperature profile along the cathode channel results in increased relative humidity along the anode channels as well. Since relative humidity along the anode channel was already 100% in regions close to the anode outlet, the temperature profile along the anode terminals was slightly reduced to keep the relative humidity profile along the anode channel close to the initial one.
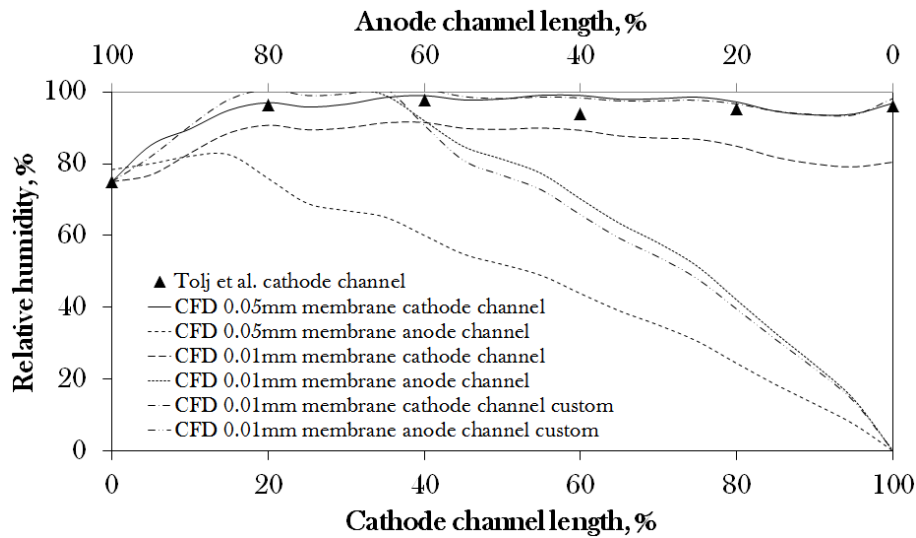
Figure 28. Relative humidity distribution along anode and cathode channel length, non-uniform temperature field case, different membranes, for current density of 550 mA cm^{-2}.

Temperature profiles for this setup are shown in Figure 29. It can be seen that difference between anode and cathode terminal temperature is up to 15 K for this configuration, which is impractical. For this reason, temperature profile along the anode and cathode terminals was kept the same during the simulations.
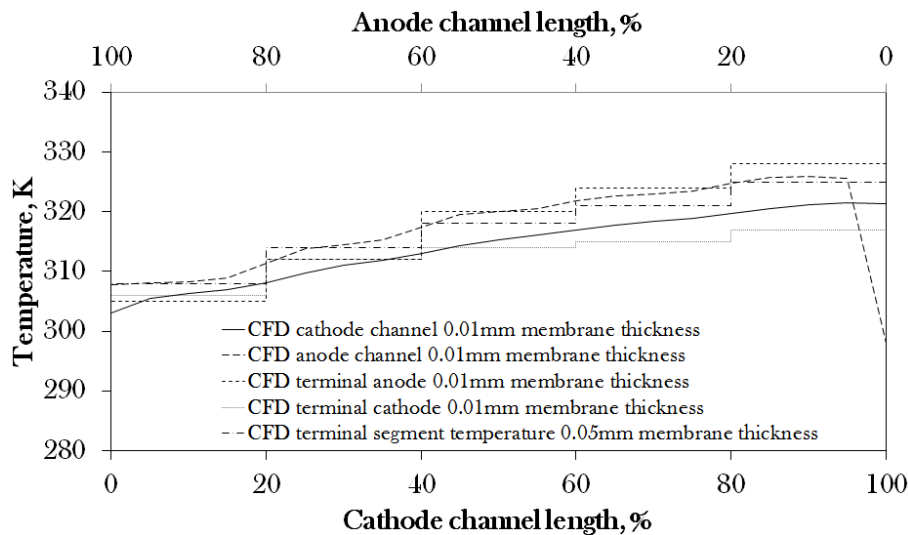
Figure 29. Temperature distribution along terminals and reactant channels for 10 μm membrane, non-uniform temperature field case for current density of 550 mA cm^{-2}.

Practical solution for establishing a non-uniform temperature profile with coolant can be done by introducing coolant channels where the flow direction is co-flow with the cathode reactant. Since the desired temperature profile is close to linear, it can be achieved with constant mass flow rate of the coolant, where the slope of the temperature profile, *i.e.* temperature gradient can be controlled by altering the mass flow rate of the coolant, as shown in chapter 6.

5.8   Conclusions

The CFD model shows good agreement with experimental results from Tolj et al. [8] and outlines details which need to be studied experimentally. The temperature distribution inside an operating fuel cell is of critical importance when partially humidified/dry reactants are considered, and needs to be experimentally studied in more detail. It is shown that the temperature inside an operating fuel cell is highly non-uniform, and the temperature inside the reactant channels is in overall higher than that of the current collectors. In order to have a robust CFD model with good prediction capacity for various operating parameters, the temperature must be measured during experiments in more points, and cannot be simply defined as one operating parameter. The temperature difference between the reactant channels and terminals increases with the current density, and the CFD model must be calibrated to account for this temperature difference at all times.

Non-uniform temperature field study has shown that there is an additional difference between the temperature of reactants along the anode and cathode channels, due to significantly higher air mass flow rate. The result is a lower temperature profile along the cathode channel compared to that of the anode channel, even though the heat is being primarily generated inside the cathode catalyst layer. This further complicates proper temperature field setup on terminals of the numerical model, since experimental data for temperature was available only along the cathode channel length in the work of Tolj et al. [8]. It is demonstrated that the membrane thickness also influences the temperature inside reactant channels, dictating the relative humidity distributions and the PEM fuel cell efficiency. Using thinner membrane is beneficial for fuel cell operation without external

humidification, as it results in higher hydration of the anode side due to the increased back-diffusion and lower temperature along the channels.

The main contribution of the CFD analysis shown in this chapter is the design of a new experimental setup, shown in chapter 7, which resolves the problem regarded to the temperature difference between the terminals and inside the channels, enables measurements of the relative humidity profiles along the anode and cathode channels, as well as the current density distribution.

6 COMPUTATIONAL FLUID DYNAMICS MODEL OF COOLANT INDUCED VARIABLE TEMPERATURE FLOW FIELD FOR PEM FUEL CELLS

6.1 Introduction

One of the main barriers for PEM fuel cell commercialization are its high specific cost and high system complexity [73,74]. The effort for cost reduction is primarily focused on reducing the cost of the membrane-electrode assembly (MEA), primarily by reducing the cost of the catalyst layer, in order to compete with internal combustion engines [74]. Besides the cell components, some automotive manufacturers have managed to decrease the cost of the PEM fuel cell system by omitting the external humidifiers, although they still require hydrogen recirculation pump in order to keep the anode side hydration on a high level [7,75].

Reactant humidification has a significant effect on the fuel cell performance [17,76-79], as well as the generated heat, since it affects the performance and durability of the cell [32,80-83]. The amount of generated heat inside an operating cell is proportional to the electrical power output. Insufficient heat removal results in accelerated membrane and catalyst layer degradation, and consequently reduces the performance of PEM fuel cell stack [17,84,85]. Excessive liquid water generation at higher current densities also hinders the performance of the cell [17], and numbers of research studies have been carried out in order to gain insight in liquid water generation, transport and removal from the cell during operation [32,47,80-94].

Combination of internal humidification of the cell and sufficient heat removal would result in decreased mass transport losses, since the liquid water would be absorbed by the upcoming stream of reactants. Commercial PEM fuel cells are also characterized by limited operating range, a consequence of using a complex system for PEM fuel cell temperature regulation and external humidification. Since the performance of the cell is dependent on the membrane water content, which corresponds to membrane's ionic conductivity, majority of commercial systems implement external humidifiers to achieve

high membrane hydration. This results in high specific cost and increased complexity of the system, but it enables high performance operation for a limited operating range.

However, the problem with implementing the external humidification into the PEM fuel cell system is that the reactants have high relative humidity upon entering the cell, while the internally generated liquid water will not be able to evaporate since the reactants are already saturated with water vapor. The occurrence of liquid water inside the gas diffusion layers (GDL) and the reactant channels causes the so-called mass transport losses. The term mass transport losses describes the amount of performance decrease due to different mechanisms of liquid water blocking the passage of the reactants through the GDL, as well as the reduction of the channel cross section due to formation of liquid water droplets. Liquid water droplets result in an increased pressure drop along the channels where they accumulate, and since the common flow fields usually have higher number of channels parallel to each other (*e.g.* serpentine flow field). This results in non-uniform reactant distribution among the neighboring channels. At higher current densities, channel blockage can occur due to a formation of plug flow (continuous water droplet across the entire channel cross-section), resulting in starvation of the cell and sudden decrease of the cell performance.

The occurrence of liquid water can also cause GDL pore blockage, resulting in non-uniform current density distribution along the membrane. The result of pore blockage is reduced active area of the catalyst, since the reactants are unable to flow through liquid water. It is easy to conclude that liquid water, *i.e.* the external humidification, results in a high number of difficulties and hinders the performance of the cell. Therefore, the commercial systems are usually designed for a limited operating range and avoid operation at high current densities.

The main objective of this chapter is development of the method of establishing high performance of the cell, modeled using CFD, without the necessity for external humidification. This is done by using internally generated water and heat, and enables wide range of operation. Internally generated water is used for reactant humidification, while internally generated heat is used for establishment of the desired temperature profile by regulation of the mass flow rate of the coolant. Since water vapor saturation profile is

temperature dependent, the two are combined to achieve high relative humidity of the reactants along the entire flow field, resulting in high performance of the cell for wide range of operating conditions.

The method shown in this chapter enables:

i)   Keeping the membrane water content on a high level without the necessity for external humidification or hydrogen recirculation pump for a wide range of operating parameters

ii)   High level of internal humidification of the anode side where the inlet hydrogen is completely dry, due to high back-diffusion along the entire flow field

iii)   Wide operating range due to simple control of the temperature field by mass flow rate control of the coolant

iv)   Prevention of flooding on higher current densities, *i.e.* minimization of the mass transport losses by evaporating the generated liquid water in the stream of reactants

v)   Application of the method for PEM fuel cell stacks by using already a standard stack system component – the coolant loop

6.2 Methodology

6.2.1 Domains

The flow field is based on a single cell from work of Tolj et al. [8]. The difference between the cell designs of this chapter vs. the previous chapter is in the end plate thicknesses. In this work end plate thickness is reduced to 2.5 mm, while in the previous studies it was 10 mm. The end plate thickness is reduced for two reasons. The first reason is that there is a significant temperature difference between the current collector terminals and the reactant channels due to poor thermal conductivity of stainless steel. This temperature difference between the terminals and the channels is problematic for proper boundary condition setup during CFD simulations. The second reason is that the reduced thickness of the end plates requires less finite volumes for the simulations, since the mesh quality criteria for PEM fuel cells are rigorous and require a fully structured mesh. Therefore, by reducing the end plate thickness, the simulation time is significantly reduced, as well as the complexity for boundary condition setup. The geometry of the cell is shown in Figure 30. Two setups are considered for the simulations, the first is for isothermal boundary condition setup, Figure 30., above, while the second one, Figure 1., below, represents the geometry with the coolant channels of equal cross section as the reactant channels, at a distance of 0.25 mm from the middle channels. For simplicity, only one coolant channel is placed along the anode and cathode side. The reactant channels are straight and parallel. The reactants are in counter-flow setup, while the coolant flow is in co-flow setup with the cathode air. The geometry specifications are shown in Table 2.
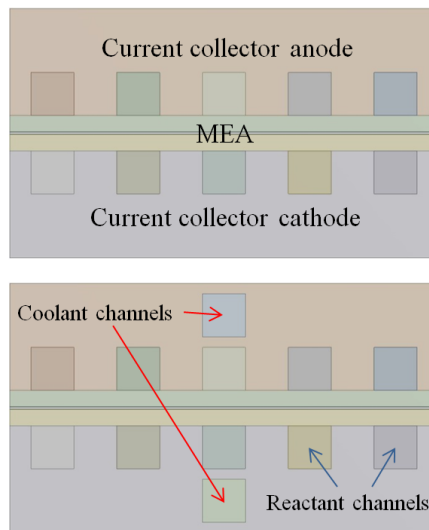
Figure 30. CFD model geometry for isothermal boundary condition setup (above) and coolant induced variable temperature field setup (below).

6.2.2 Mesh and experimental data

The computational grid, *i.e.* mesh uses the same number of divisions and element sizes as the one in the previous chapter. The experimental data is adopted from a study of Tolj et al. [8].

6.3 Governing equations and boundary conditions

For governing equations please refer to the Chapter 6.4. The operating parameters are shown in Table 2.

Table 2. Operating parameters

Parameter	Value
Cathode stream abs. pressure	1.01325 bar
Anode stream abs. pressure	1.01325 bar
Cathode stream inlet temperature	30 °C
Anode stream inlet temperature	25 °C
Coolant inlet temperature	30 °C
Fuel cell temperature	60 °C or coolant induced
Relative humidity of cathode stream inlet	0.75
Relative humidity of anode stream inlet	dry
Current density	500 mA cm^{-2}
Stoichiometry, cathode	2.15
Stoichiometry, anode	1.2
Flow configuration anode vs. cathode	Counter-flow
Flow configuration cathode vs. coolant	Co-flow
End plate thickness	2.5 mm
Channel length	200 mm
Channel width at anode and cathode	1 mm
Channel height at anode and cathode	1 mm
Membrane thickness (Nafion 212)	0.05 mm
Catalyst layer thickness	0.01 mm
Platinum loading	0.5 mg cm^{-2}
Gas-diffusion layer thickness	0.38 mm
Effective area	2000 mm^2
Membrane dry density	2 g cm^{-3}
Membrane molecular weight	1100 g mol^{-1}

6.3.1 Domain boundary conditions

The domain type for all domains is defined as fluid bodies, except for current collectors which are defined as solid bodies.

6.3.2 Inlet boundary conditions

The mass flow inlet boundary condition is defined for anode and cathode inlets. The anode inlet dry hydrogen temperature was set to 25 °C. Cathode inlet air temperature was set to

30 °C, with a relative humidity of 0.75. The anode mixture of gases consisted of hydrogen and water vapor (while the mass fraction of water vapor was set to zero on the anode inlet). The cathode mixture of gases consisted of nitrogen, oxygen and water vapor. The mass flow rate of the coolant is prescribed to result in a temperature profile close to the water vapor saturation profile. The coolant is deionized water, and the mass flow rate of the coolant was calculated to result in the desired temperature profile for each current density separately.

6.3.3   Outlet boundary conditions

On the anode and cathode reactant and coolant channel outlets, the pressure outlet boundary condition is applied with a zero gauge pressure and backflow total temperature set according to the temperature field setup.

6.3.4   Wall boundary conditions

Non-slip boundary conditions were applied to the walls. The temperature was fixed on terminals of the anode and cathode current collectors for isothermal temperature field study. For coolant induced variable temperature field case, the walls are defined as adiabatic surfaces, and the resulting temperature profile is defined by the coolant mass flow rate. The electric potential on the anode terminals was set to zero. On the cathode terminals different values of electric potential are defined in order to extract the polarization curve. The remaining surfaces are defined as walls by default.

6.3.5   Prescribing the desired temperature profile

Prescribing the desired temperature profile is achieved by prescribing the mass flow rate of the coolant liquid – deionized water, flowing in the co-flow direction with the cathode air. The mass flow rate $\dot{m}$ of the coolant is determined by expression

$$\dot{m} = \frac{\dot{Q}}{c_{\mathrm{w}} \Delta T} \tag{39}$$

where $\dot{Q}$ represents the total generated heat and water phase change enthalpy, c_w represents specific heat, and ΔT represents the desired temperature difference between the outlet and inlet of the coolant liquid.

The generated heat is defined by a heat source term S_h by expression

$$S_h = h_{\text{react}} - R_{\text{an,cat}}\eta_{\text{an,cat}} + I^2 R_{\text{ohm}} + h_L \tag{40}$$

where h_{react} is heat released from electrochemical reaction of hydrogen and oxygen on the triple-phase boundaries inside the cathode catalyst layer, while $R_{\text{an,cat}}$ represent anode/cathode over-potential, $\eta_{\text{an,cat}}$ transition current, I is the total electrical current, R_{ohm} are ohmic losses, and h_L is the phase change enthalpy of water evaporation/condensation. The term h_L is neglected during the simulations, since the CFD model is single-phase. Nomenclature and symbols are adopted from the software manual [12].

6.4 Results and discussion

The desired temperature profile resulting in high performance of the cell without the necessity for external humidification is extracted from Mollier's *h-x* diagram. The desired temperature profile corresponds to water vapor saturation profile, *i.e.* the goal is to keep the relative humidity along the cathode channel close to 100% while taking into consideration the amount of generated water inside the cell.

The temperature distribution along the flow field dictates the water vapor saturation pressure, different relative humidity profiles can be achieved just by manipulating the temperature distribution, *i.e.* temperature gradient. In the previous chapter, the CFD model was used to establish a segmented temperature profile. The temperature profile was established by segmenting the current collector terminals into five equal surfaces, where the prescribed temperature was averaged from the desired temperature profile. In this chapter, the desired temperature profile is established by regulating the mass flow rate of the coolant liquid − deionized water. The deionized water enters the cell at ambient temperature, equal to the temperature of the cathode air (30 °C), in co-flow with the cathode air. For a prescribed current density, the mass flow rate of the coolant is calculated to establish the temperature difference between coolant inlet and outlet from the cell. The required temperature difference, *i.e.* temperature gradient for this case is calculated using Mollier's *h-x* chart and equals 30°C for current density of 500 mA cm^{-2}. The resulting temperature distribution is shown in Figure 31.
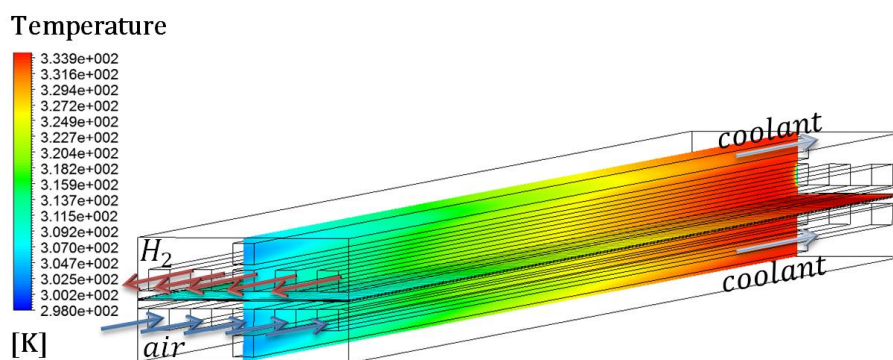
Figure 31. Contours of temperature along the cell cross-sections.

In Figure 31., it can be seen that the anode hydrogen is in counter-flow configuration in respect to the cathode air and coolant. Counter-flow configuration of the anode hydrogen is chosen to result in higher overall relative humidity along the anode channels.

6.4.1 Temperature profiles

Dry hydrogen enters the cell at temperature of 25 °C, *i.e.* 298 K, while the cathode air with relative humidity of 0.75 enters the cell at temperature of 30°C, *i.e.* 303 K, the reactants are in counter-flow configuration, as shown in Figure 32.
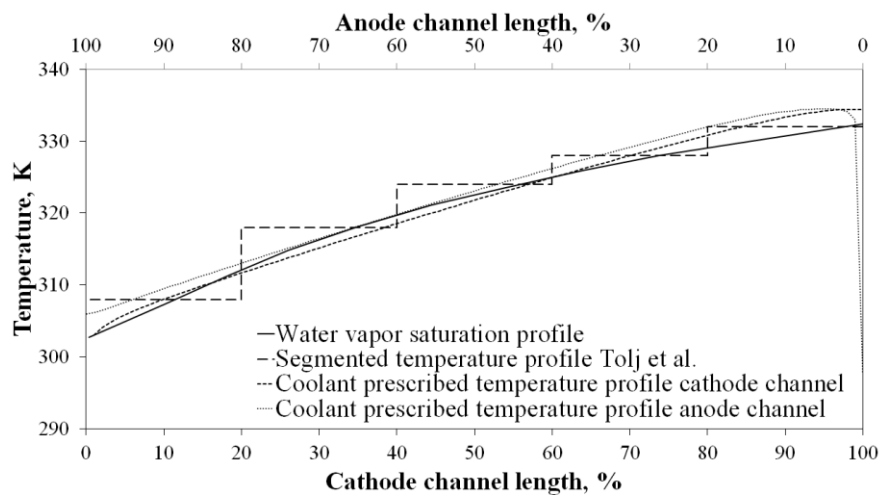
Figure 32. Comparison of temperature profiles.

The resulting temperature profile of the cathode air very closely resembles the desired temperature profile extracted from Mollier's *h-x* diagram. The segmented temperature profile from study of Tolj et al. [8] shows less agreement with the desired temperature profile, compared to the temperature profile established with coolant mass flow rate control. This is due to the fact that the temperature profile was previously segmented into five equal parts, where the temperature of each segment was kept on a uniform value via Peltier thermoelements. The anode channel temperature is overall higher than the cathode channel temperature, as seen in the previous chapter, due to much lower mass flow rate of hydrogen when compared to the mass flow rate of air (even though hydrogen has significantly higher specific heat).

6.4.2 Relative humidity

Figure 33. shows relative humidity profiles along the anode and cathode channels, as well as the relative humidity profile along the cathode channel measured experimentally by Tolj et al. [8] for isothermal boundary conditions (60 °C) at current density of 500 mA cm^{-2}.
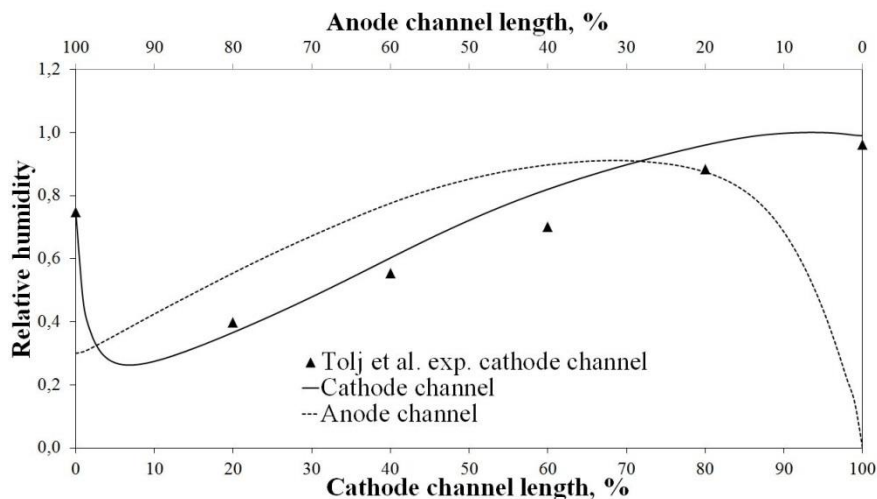
Figure 33. Relative humidity distribution along the reactant channel mid-planes for isothermal (60°C) boundary conditions of current collectors at current density of 500 mA cm^{-2}.

Since the experimental data was not available along the anode channel, the comparison could not be made in this stage of research. However, after the new experimental setup was developed, chapter 7, complete validation is done later in chapter 8. Similar relative humidity profiles are shown in the previous chapter. Since the thickness of stainless steel current collectors is reduced in this work to 2.5 mm, compared to 10 mm in a previous chapter, the heat transfer is different. In the previous chapter, where 10 mm end plates are used, there is a temperature difference between the reactant channels and the current collectors of 6-8 K. The temperature difference, *i.e.* higher temperature along the channels than on current collector terminals, is proportional to end plate thickness, due to poor thermal conductivity of stainless steel (13 – 17 W m^{-1} K^{-1}). In this work, since the thickness of end plates is 25% of the previous one, the resulting temperature profiles are also slightly different, as well as the resulting relative humidity profiles along the reactant channels. There is a good agreement with relative humidity profile along the cathode channel with

experimental results of Tolj et al. [8], suggesting that the computational model is well calibrated.

Relative humidity profiles for coolant induced variable temperature field case at current density of 500 mA cm^{-2} are shown in Figure 34.
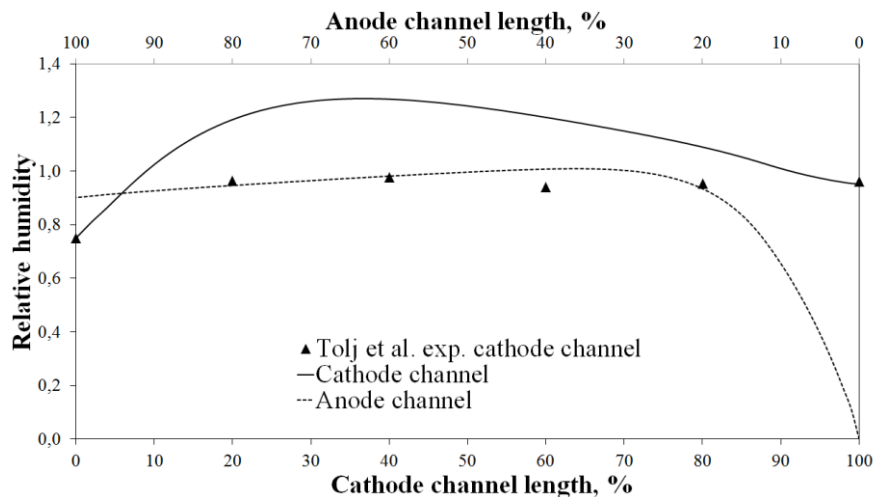
Figure 34. Relative humidity distribution along the reactant channel mid-planes for coolant induced variable temperature field at current density of 500 mA cm^{-2}.

Since the model is single phase, the relative humidity along the cathode channel exceeds value of 1. However, since the relative humidity profile measured experimentally by Tolj et al. [8] is practically 100% along most of the channel length, this suggests that the desired relative humidity profile is reached, and a small portion of water vapor will condense along the channel. Anode channel relative humidity profile is significantly higher when compared to the relative humidity profile achieved in the previous chapter with segmented temperature profile, which is beneficial for PEM fuel cell operation, since the membrane hydration in this case is higher, *i.e.* the ionic conductivity of the membrane is higher for coolant induced variable temperature field. For other current densities, the coolant mass flow rate was calculated to result in close to 100% relative humidity on the cathode outlet.

Since the mass flow rate of hydrogen is significantly lower than the temperature of the cathode air and coolant, the anode hydrogen heats up very quickly to temperature of 60 °C

immediately after entering the cell. Hydrogen is the gradually cooled in the downstream direction by the coolant.

6.4.3 Membrane water content

The membrane water content λ distribution along the membrane mid-plane is shown in Figure 35.
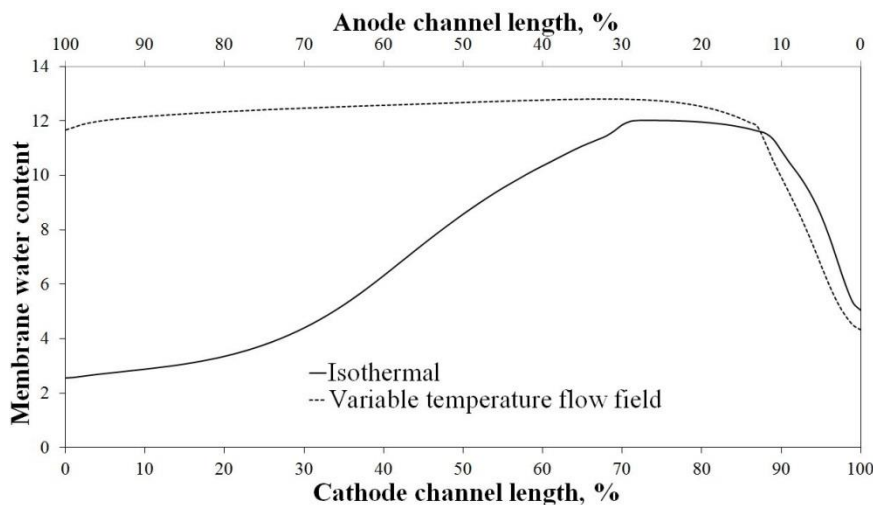
Figure 35. Membrane water content (λ) distribution along the membrane mid-plane for isothermal and coolant induced variable temperature flow field at current density of 500 mA cm⁻².

It can be seen that the membrane water content for coolant induced variable temperature flow field case is much higher and quite uniform along the most part of the flow field. This is due to high relative humidity profiles along the anode and cathode side in variable temperature flow field case. Around 88% of the cathode channel length the λ value is suddenly decreased because the anode hydrogen relative humidity is low in this region, *i.e.* it is dry at the inlet to the cell, as seen previously in Figure 33.

Considering the back-diffusion peak, mentioned in the previous chapter for coolant induced variable temperature flow field case, occurring for intervals in vicinity of $\lambda=3$, the value of λ around 88% of the cathode channel length, in Figure 35.,is much higher so intuitively there should be no peak in this region. However, it must be noted that the λ

value is extracted for the membrane mid-plane, and it is significantly lower on the anode side. This is due to the supply of dry hydrogen at the cell inlet.

6.4.4 Current density

Current density distributions are shown in Figure 36. They are extracted at the membrane mid-plane. It can be seen that the coolant induced variable temperature flow field has quite uniform current density distribution, when compared to the isothermal case.
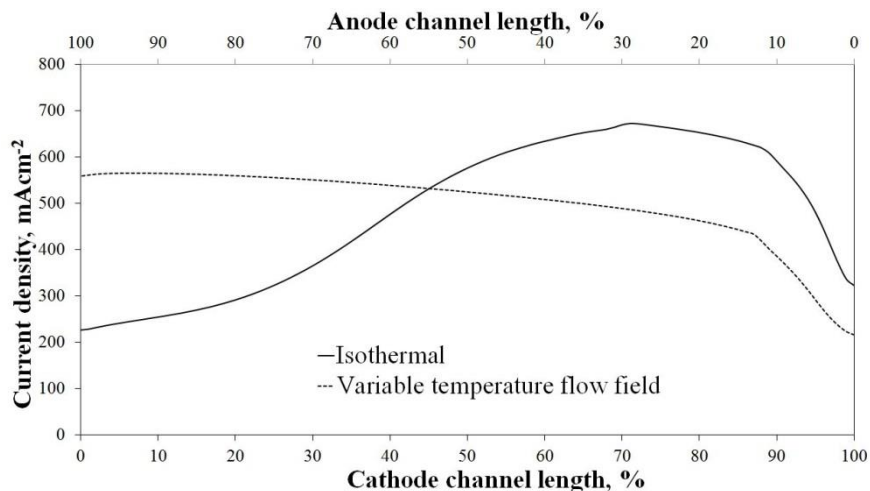
Figure 36. Current density distribution along the membrane mid-plane for isothermal and coolant induced variable temperature field at current density of 500 mA cm^{-2}.

This is a reflection of uniform membrane water content λ distribution along the entire flow field, caused by high relative humidity along the entire flow field. Uniform current density distribution along the entire flow field is beneficial for PEM fuel cell operation because it results in uniform reactant consumption and uniform heat release along the entire flow field, and has potential for improving the PEM fuel cell durability.

6.4.5 Polarization curves and coolant mass flow rate

Polarization curve is extracted for the coolant induced variable temperature flow field, Figure 37., and compared with results of Tolj et al. [8].
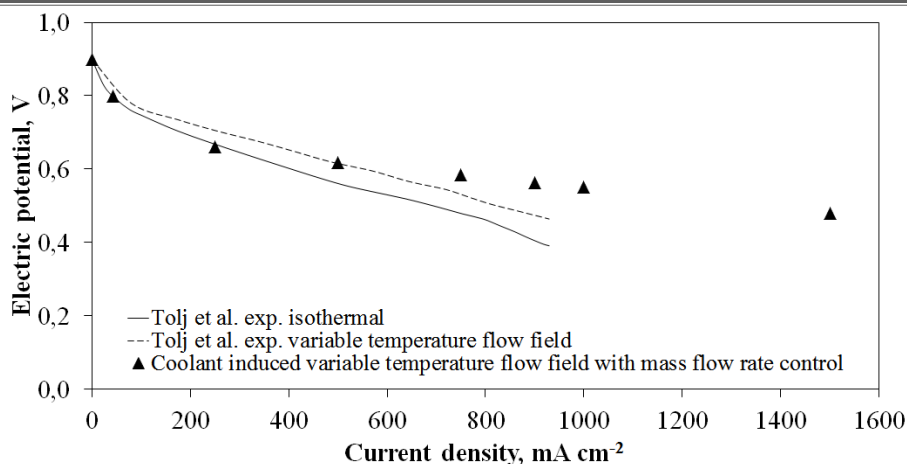
Figure 37. Polarization curve comparison.

Since the mass flow rate of the coolant required for establishing the desired temperature profile for low currents was very low, and PEM fuel cell operation at low currents, *i.e.* high voltage results in higher membrane degradation, the threshold value for mass flow rate was chosen to establish the desired temperature profile for current density of 500 mA cm^{-2}. At lower currents, the polarization curve shows good agreement with isothermal results of Tolj et al. [8]. This is due to small temperature gradient caused by relatively high mass flow rate of the coolant for the specified currents. At current densities higher than 500 mA cm^{-2} another detail can be seen. The operating electric potential at higher currents is greater in the case for coolant induced variable temperature field when compared to variable temperature field case of Tolj et al. [8]. The reason for this is that Tolj et al. [8] have kept the same temperature profile at the current collector terminals, while the temperature along the reactant channels was significantly higher due to a combination of heat release from the electrochemical reactions and low thermal conductivity of 10 mm stainless steel end plates. Coolant induced variable temperature field solves this problem, because the coolant channels are in close proximity to the reactant channels, so the temperature difference between the two is low. Since the liquid water generated from the electrochemical reaction inside the cathode catalyst layer is absorbed by the reactants, the mass transport losses are minimized at higher currents, resulting in wide operating range of the cell with minimized danger of flooding.

The mass flow rate of the coolant dependent on the operating current density is shown in Figure 38.
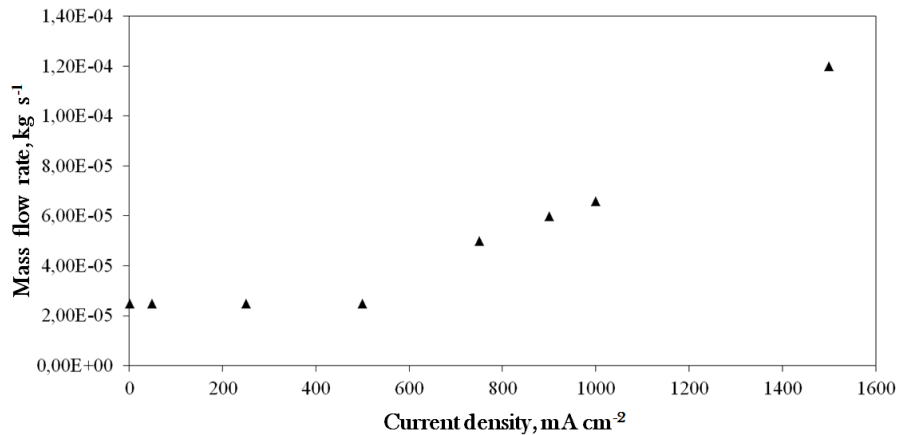
Figure 38. Mass flow rate vs. current density for establishing the desired relative humidity profile along the cathode channel.

As already mentioned, the mass flow rate was fixed to a minimum value of $2.5 \cdot 10^{-5}$ kg s^{-1}, required to establish the desired temperature profile at current density of 500 mA cm^{-2}. At higher current densities, the mass flow rate of the coolant was calculated to result in relative humidity of 1 on the cathode outlet. Mass flow rate dependency on current density is close to linear, because the dominant heat source is heat released from electrochemical reactions, resulting in slightly parabolic trend of the curve at higher current densities.

The method for establishing the desired temperature profile by coolant mass flow rate control is applicable for different ambient conditions of air, *e.g.* relative humidity and temperature. Input temperature and relative humidity of air can be used to determine the initial point in the Mollier's *h-x* diagram. The desired profile can be easily calculated using Mollier's diagram based on prescribed current density, *i.e.* the amount of generated water inside the cell, and the desired relative humidity of the end point equal to 1. Since the desired temperature profile is linear-wise, the coolant mass flow rate can be easily determined using elementary thermodynamics. In this way, the system can be adapted for different ambient conditions. The components for required for such operation would consist of thermocouple on the coolant outlet, and feedback to a valve or a pump to increase or reduce the coolant mass flow rate based on the calculated function. The starting

point in the diagram would require measurement of inlet air temperature and relative humidity. In such way, the system could be fully automatized and would be able to cover wide range of ambient conditions. For low temperature applications, the deionized water could be replaced by a mixture of deionized propylene-glycol and water. The concept will be investigated experimentally in a future study.

6.5   Conclusions

The concept of establishing the desired variable temperature flow field for PEM fuel cells by coolant mass flow rate control is analyzed numerically and shows very positive results for further potential commercial development and application. By using internally generated water and heat, many common problems of PEM fuel cells are resolved, such as water removal and omitting the costly external humidification systems. The application of variable temperature flow field is adaptable for different current densities, and shows significant improvement in performance at higher current densities, since the generated water is evaporated in the reactant gases and the mass transport losses at higher currents are minimized. Since the reactant relative humidity is high along the entire flow field, the current density distribution along the flow field is quite uniform, unlike in the isothermal study, resulting in more stable operation. Another benefit from the concept is very good humidification of the anode side, fed at the inlet with dry hydrogen. This is due to high back diffusion, combined with decreasing the temperature of the anode hydrogen downstream.

7 EXPERIMENTAL INVESTIGATION OF THE VARIABLE TEMPERATURE FLOW FIELD FOR PEM FUEL CELLS

7.1 Introduction

The new experimental setup is designed in order to calibrate and thoroughly validate the developed CFD models, presented previously in chapters 5 and 6. The new experimental setup enables:

i)   measurement of the net local water transport through the membrane by measuring the relative humidity and temperature profiles directly inside the channels before and after each segment in total of 12 points, 6 along each side of the membrane

ii)   measurements of temperature on each segmented current collector terminal, total of 10 measurements, 5 on each side of the cell

iii)   measurements of the current density distributions along the cell, with the capability of adjustment of the contact resistances of each segment separately.

iv)   regulation of the temperature of each segment separately along the anode and cathode side via ten Peltier thermoelements driven by the relay PID control

v)   very close resemblance of the temperature distribution along the cell to the actual water vapor saturation temperature profile due to a compact design

All measurements are in-situ, operando. This also enables the investigation of the transient phenomena of the cell, but this is a topic for a future study.

7.2 Experimental setup

The exploded view of the cell is shown in Figure 39. (above) The cell consists of five linearly placed molded graphite segments, insulated electrically and thermally from the neighboring segments via polycarbonate matrix. The five parallel, straight channels are machined in the polycarbonate matrix and the molded graphite plates. The total length of the channels is 250 mm, the channels and lands are of rectangular (1×1) mm cross-section. The dimensions of the molded graphite segments are (L×W×H = 40 mm × 40 mm × 5 mm).
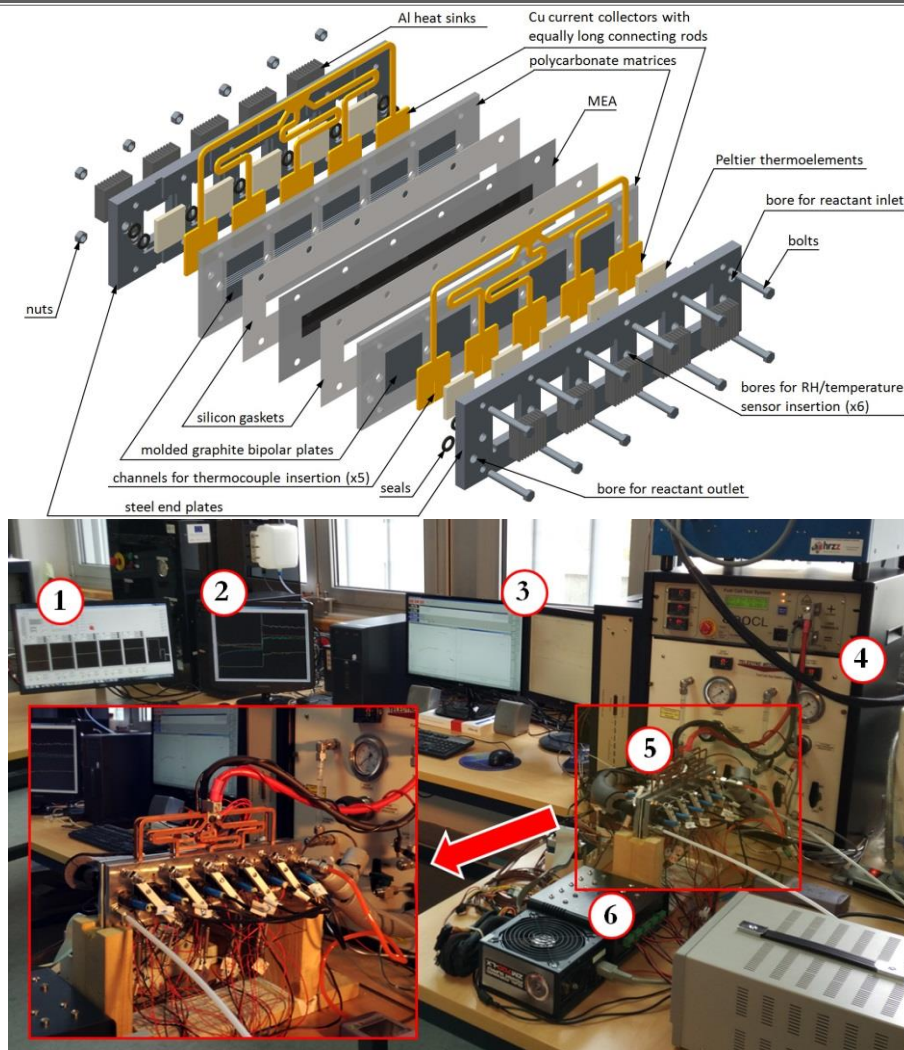
Figure 39. Exploded view of the new experimental setup with annotated elements (above) and the overall experimental setup assembly (below): 1 – PID temperature regulation of Peltier thermoelements on each segment and RH&T inside the channels monitor; 2 – current density monitor of each segment; 3 – fuel cell test station monitor; 4 – fuel cell test station; 5 – segmented fuel cell; 6 – Peltier thermoelement's power supply and in-house built relay control system; red rectangle – segmented cell detail.

The molded graphite segments are connected in parallel via copper current collectors, the copper is chosen because it has high thermal and electrical conductivity. Silver paste is applied between the copper and molded graphite segments in order to reduce the contact resistance between the components. Peltier thermoelements are individually attached on each copper current collector. The channels for thermocouple insertion are machined in each copper segment, since it was seen in the previous chapters that the temperature of the

current collector terminals was visibly different when compared to the temperature inside the channels. Each Peltier thermoelement has an attached aluminum heat sink and a fan for improved heat removal rates.

The structural components are fixed between two stainless steel end plates with 12 nuts and bolts. Bores for insertion are placed between the neighboring segments in order to enable insertion of fittings with RH and temperature sensors directly inside the reactant channels. Silicone gaskets and O-ring seals are used to prevent the reactants from leaking into the surrounding atmosphere. The connecting rods of the current collectors are of equal length in order to achieve similar ohmic losses of each segment. Current shunts are soldered on each connecting rod and calibrated to enable spatially resolved in-situ current density monitoring.

The overall experimental setup is shown in Figure 39. (below). The temperature of each Peltier thermoelement can be prescribed independently via PID control from a personal computer, giving the setup high flexibility. As noted in previous chapters dealing with computational fluid dynamics analysis of the variable temperature flow field concept, the temperature along the entire cell is non-uniform inside the reactant channels. Also, the temperature is always different on the anode vs. the cathode side if the reactant inlet temperature is lower than the temperature of the cell.

7.3   Calibration

Since the temperature is of paramount importance for this work, the temperature is directly measured on the current collector terminals as well as inside the channels. The current collector temperature data is relevant for Peltier thermoelement PID control, while the temperature inside the channels is relevant for the case studies. The temperature is measured inside the channels via relative humidity and temperature sensors (RH&T). Since the temperature measured via RH and temperature sensors was quite different when compared to the temperature of the current collector terminals, *Figure 40*. (left), the additional measurements of the temperature were also carried out on 1 mm distance from the gas diffusion layer (GDL) substrate by inserting T-type thermocouples (TC) through the fittings, mounted in a specially designed cap. The temperature measured via TCs is considered to be the relevant temperature for the experimental measurements since it

represents the actual operating temperature inside the channels. Along the entire length of the channel, the temperature of the anode hydrogen was higher when compared to the temperature of the cathode air, as already seen in the CFD analysis in chapters 5 and 6, since the mass flow rate of hydrogen was significantly lower, even though hydrogen has roughly 14 times higher specific heat when compared to air (for comparison, the mass flow rate of air is roughly 64 times higher at current density of 500 mA cm^{-2} for the prescribed stoichiometry seen in Table 2.). The desired temperature profile in *Figure 40.* (left) represents the temperature of the cathode channel, *i.e.* the cell temperature. The term „isothermal" is used in this work in respect to the setup of Peltier thermoelement temperature, since clearly the temperature distribution is inhomogeneous regardless of the fine-tuned PID regulation with a total of 10 Peltier thermoelements over the total cell length of 250 mm.
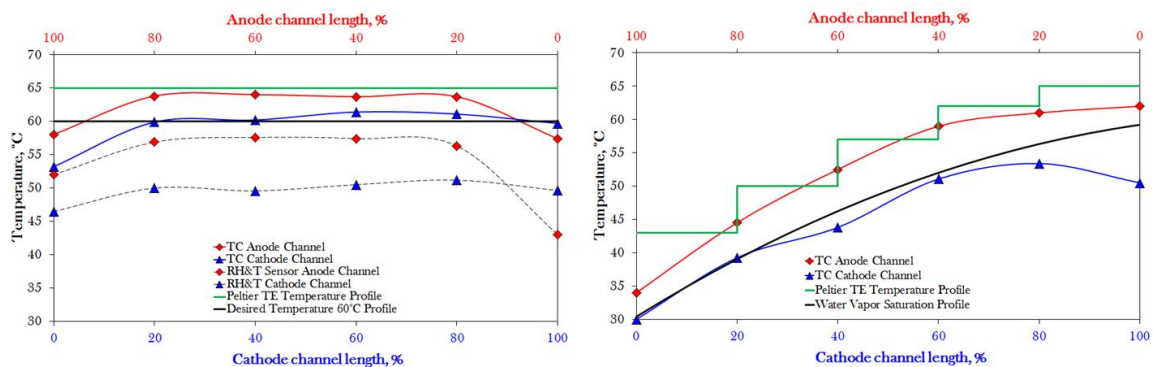
Figure 40. Temperature distributions along the operating cell, representing „isothermal 60 °C" (left) and VTFF (right) case at current density of 500 mA cm^{-2}, operating parameters are shown in Table 3.

The observed inhomogeneous temperature distributions inside the isothermal cell are more pronounced in the variable temperature flow field case, as seen in *Figure 40.* (right)

The definition of the proper temperature on Peltier thermoelements for establishment of the desired temperature profile inside the channels was iterative. Since the flow configuration was counter-flow, the cathode outlet, *i.e.* the anode inlet, temperature was lower than the rest of the cell. This is a result of high heat losses of the first and last segment, since the segmented cell could not be insulated because the Peltier thermoelements require high heat removal rates for proper operation.

The measurement of RH&T was carried out using Sensirion™ SHT21 sensors. During the measurements, there were high discrepancies between the temperatures measured by the RH&T sensors compared to the temperatures inside the channels measured with TCs. The difference in temperature is a result of using fans, mounted on aluminum heat exchangers for Peltier thermoelements, and the distance of 5 mm of the sensor cap from the channel outer surface. Since the Peltier thermoelements were actually heating the cell during operation, the outer surface of the thermoelement was cold (because Peltier thermoelements heat on one side, and cool on the opposite side). The fans mounted on the outer surface of the Peltier thermoelemens were cooling the fittings with mounted RH&T sensors. In order to solve this problem, the original stainless steel fittings were removed and replaced with quick-change fittings with removable caps to enable external pre-heating of the RH sensors and the fans have been turned off, resulting in much slower establishment of the desired temperature profile. The sensors were pre-heated to temperature of 75-80 °C and quickly inserted inside the quick-change fittings during operation in order to prevent starvation of the cell. This also served to prevent condensation of liquid water on the sensors. The RH&T data was monitored and the values have been recorded.

Current shunts have been soldered on each current collector rod (total of 5 current shunts) and double-calibrated. The first calibration consisted of soldering the shunt ends on equal distance from each other on each current collector rod on one side of the cell. The voltage drop was measured and the goal was to achieve a similar value on each shunt. However, after cooling of each rod, the values have been slightly altered due to different ohmic resistance of the copper rods at different temperatures. This required second calibration in the data acquisition software by introducing the correction coefficients.

Since the cell was assembled from different components, the contact resistance of each segment was different, therefore to ensure equal pressure force on each segment, specially designed pressure rods have been introduced, the pressure rods are shown in Figure 39. (below) in red rectangle – white rectangular rods positioned diagonally across each segment. The pressure rods have served to fix each Peltier thermoelement, heat sink and the fan on the construction, but the primary function was to achieve uniform pressure force on each segment by tightening the nuts of each segment with the same momentum. The

pressure force was uniformly applied on the copper current collector segments by directly applying force with two bolts protruding from the pressure rods on the rectangular aluminum heat sink of the Peltier thermoelements which are directly mounted on the copper current collectors.

7.4   Results and discussion

The focus of this paper is comparison of the variable temperature flow field operation with conventional isothermal operation of the cell in regard to the spatially resolved water transport and current density distributions along the segments of each case. The water transport of the fully humidified case was not studied since the RH is 100% along the entire flow field. The studied cases represent:

i)   Fully humidified (reactants 100% RH at 60 °C) isothermal (ISO) operation at 60 °C

ii)   Partially humidified (dry hydrogen and 75% RH air at 30 °C) ISO operation at 60 °C

iii)   Variable temperature flow field (VTFF) operation without external humidification (dry reactants at 30°C)

The operating parameters are shown in Table 3. The operating parameters are similar to the ones used in study of Tolj et al [8]. The difference is that this work also investigated the operation for completely dry reactants, and operation for isothermal study with fully humidified reactants, while the Tolj et al. [8] study considers only operation with dry hydrogen and ambient air under isothermal and variable temperature flow field operating conditions. The membrane-electrode assembly (MEA) used in this work has a micro-porous layer (MPL), unlike the one used in [8], slightly thinner catalyst layer (0.00085 mm vs 0.001 mm), and slightly different GDL substrate thickness (0.33 mm vs. 0.38 mm).

Table 3. Operating parameters.

Parameter	Value
Cathode stream abs. pressure	1.01325 bar
Anode stream abs. pressure	1.01325 bar
Cathode stream inlet temperature	30 °C/60 °C
Anode stream inlet temperature	25 °C/60 °C
Fuel cell temperature	60 °C or VTFF
Relative humidity of cathode stream inlet	0.75/1/0
Relative humidity of anode stream inlet	0/1
Stoichiometry, cathode	2.15
Stoichiometry, anode	1.2
Flow configuration anode vs. cathode	Counter-flow
Molded graphite segment thickness	5 mm
Channel length	250 mm
Channel width at anode and cathode	1 mm
Channel height at anode and cathode	1 mm
Membrane thickness (Nafion 212)	0.05 mm
Catalyst layer thickness	0.0085 mm
Platinum loading	0.5 mg cm^{-2}
Gas-diffusion layer thickness	0.41 mm
Gas-diffusion layer substrate thickness	0.33 mm
Micro-porous layer thickness	0.08 mm
Effective area	2500 mm^2
Membrane dry density	2 g cm^{-3}
Membrane molecular weight	1100 g mol^{-1}

7.5   Fully humidified (reactants 100% RH at 60°C) ISO operation at 60 °C

The main objective of the experimental study is to compare the performance of the VTFF operation with commercially used ISO operation with fully humidified reactants. Fully humidified case polarization curve is shown in Figure 41. The overall performance of the cell is quite poor, due to high ohmic losses from the contact resistances, and the custom made MEA.
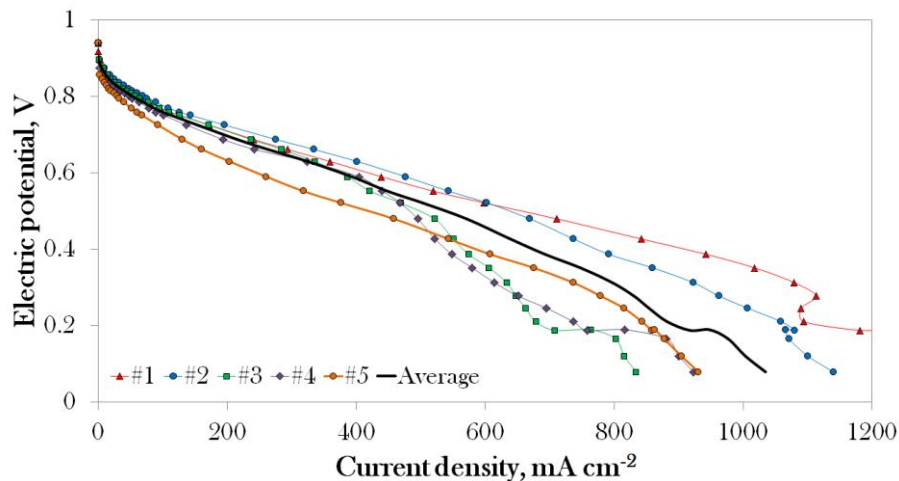
Figure 41. Polarization curve of each segment for ISO fully humidified case, #1 represents the cathode inlet/anode outlet, #5 represents the cathode outlet/anode inlet, measured via current shunts, operating parameters shown in Table 3.

Additional problem encountered during the measurements was the lower mass flow rate limit of the test station of 0.1 sl min^{-1}, and since the cell active area was only 2500 mm^2, the actual stoichiometric flow was achieved at current density around 500 mA cm^{-2}. This caused higher water accumulation inside the cell for the fully humidified isothermal case, and more pronounced dehydration of the cell for the partially humidified case, and VTFF case in lower current regions. The highest performance is achieved on segments #1 and #2. Segments #3 and #4 and #5 show high mass transport losses due to excessive water accumulation caused by the constant mass flow operation at lower currents. As a result, the liquid water accumulated in the cathode downstream direction, hindering the performance of the cell. The oscillations seen in the polarization curve at higher current densities are due to the expelling of liquid water from the cell induced by higher mass flow rate of the reactants. The RH distribution along the cell is not shown because all values are 100%, therefore they could not be measured using RH&T sensors.

7.6   Partially humidified (dry hydrogen and 75% RH air at 30 °C) ISO operation at 60 °C

The partially humidified case, similar to the one in the study of Tolj et al. [8], polarization curve is shown in Figure 42. It can be seen that the performance is quite low due to high ohmic losses induced by the membrane dehydration in the low current regions, as

previously mentioned. The mass transport losses are hardly visible, since the highest quantity of liquid water is evaporated in the stream of under-saturated reactants.
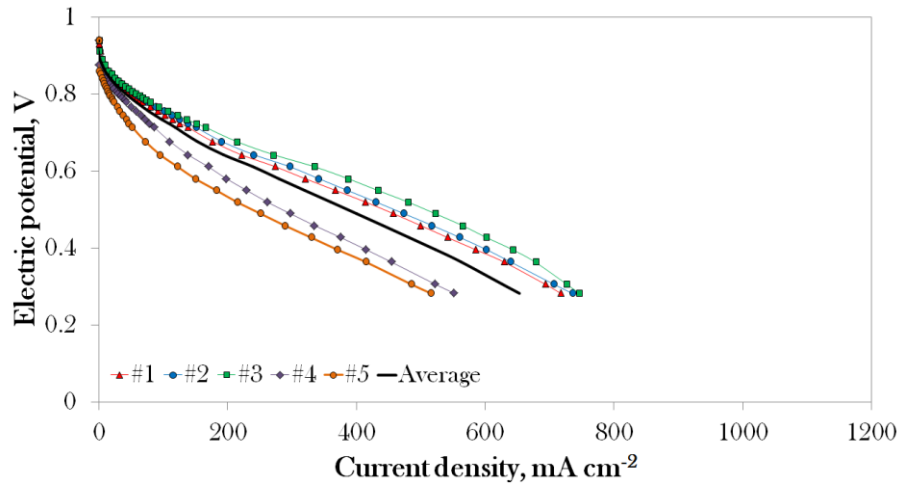
Figure 42. Polarization curve of each segment for ISO partially humidified case, #1 represents the cathode inlet/anode outlet, #5 represents the cathode outlet/anode inlet, measured via current shunts, operating parameters shown in Table 3.

The relative humidity profiles along the anode and cathode channels are shown in Figure 43. The cathode side relative humidity, Figure 43. (above), decreases from the initial value of 75% at 30 °C, to around 43% (point 2) due to sudden increase in the temperature of the air from 30 °C to the cell temperature of 60 °C, i.e. the temperature along most part of the cathode channel, as seen previously in *Figure 40*. (below). The RH of cathode air increases in the downstream direction due to evaporation of the generated water and it reaches a value of around 100% on the cathode outlet. However, the membrane hydration, i.e. water content, is very low along almost the entire flow field.
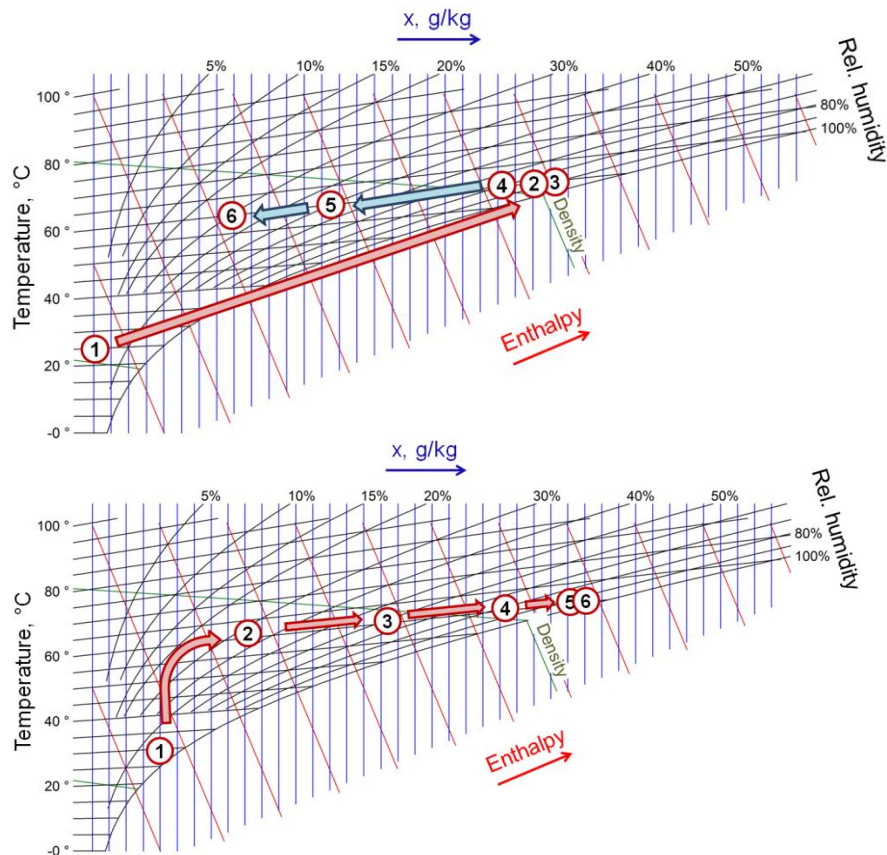
Figure 43. Mollier chart display of relative humidity distribution along the cell length for the anode (left) and cathode (right) side of the cell, ISO partially humidified case, at current density of 500 mA cm^{-2}. Point 1 represents the inlet of the anode/cathode, point 6 represents the outlet of the anode/cathode side, measuring points are before and after each of the five segments. Red arrow – increase in absolute humidity, blue arrow – decrease in absolute humidity.

The anode side, Figure 44, shows the trend of increasing RH between points 1, 2 and 3, and decreasing RH between points 3, 4, 5 and 6. Since the anode side is fed with dry hydrogen, the water flux between points 1 and 2 is indication of the dominating back-diffusion water flux in the direction from the cathode to the anode side of the cell, while the remaining decrease in RH results from the dominant electro-osmotic drag water flux in the direction from the anode to the cathode. Mollier's *h-x* chart is a useful tool for determining the dominant mechanism of water transport through the membrane, because it also gives insight in the absolute humidity, temperature and enthalpy distributions along the cell, unlike the conventional RH vs. channel length diagram, and it directly enables

determination of the optimal VTFF profile by linearly connecting the first point in the diagram to the last one and plotting the temperature profile.

7.7   VTFF operation without external humidification (dry reactants at 30°C)

The VTFF without external humidification case polarization curves are shown in Figure 44. It can be seen that the performance is significantly higher when compared to the partially humidified ISO operation, evident from the decreased slope of the polarization curves. On higher current densies there are minor mass transport losses, which give evidence of the evaporation of the generated water. For comparison, the commonly used ISO fully hydrated case, Figure 41., shows very high mass transport losses. The VTFF case performance would certainly be overall higher for a cell with higher active area, since the minimal mass flow rate constraint would not affect the performance at lower currents as much as it does on a cell of this size. The severe dehydration caused by very high stoichiometry is very pronounced on segment #5, since it is closest to the anode inlet which is severely dehydrated on lower currents due to the very high stoichiometry in the mentioned regions, as well as the highest temperature, i.e. lowest RH, as seen in Figure 45. (left), between points 1 and 2.
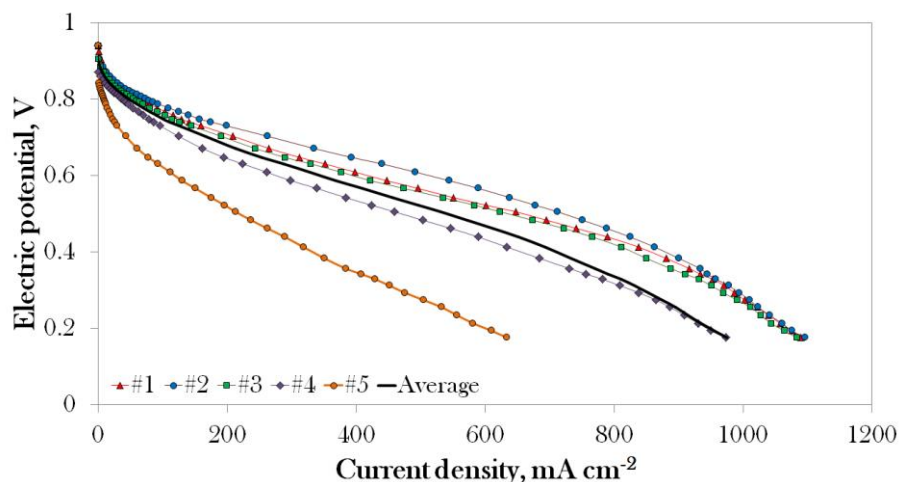
Figure 44. Polarization curve of each segment for VTFF dry reactants case, #1 represents the cathode inlet/anode outlet, #5 represents the cathode outlet/anode inlet, measured via current shunts, operating parameters shown in Table 3.

The RH profiles are shown for the anode and cathode side in Figure 45. The cathode side, Figure 45. (below), RH profile closely resembles the water vapor saturation profile, therefore the RH is almost 100% along the entire flow field, even though the dry air enters the cell.
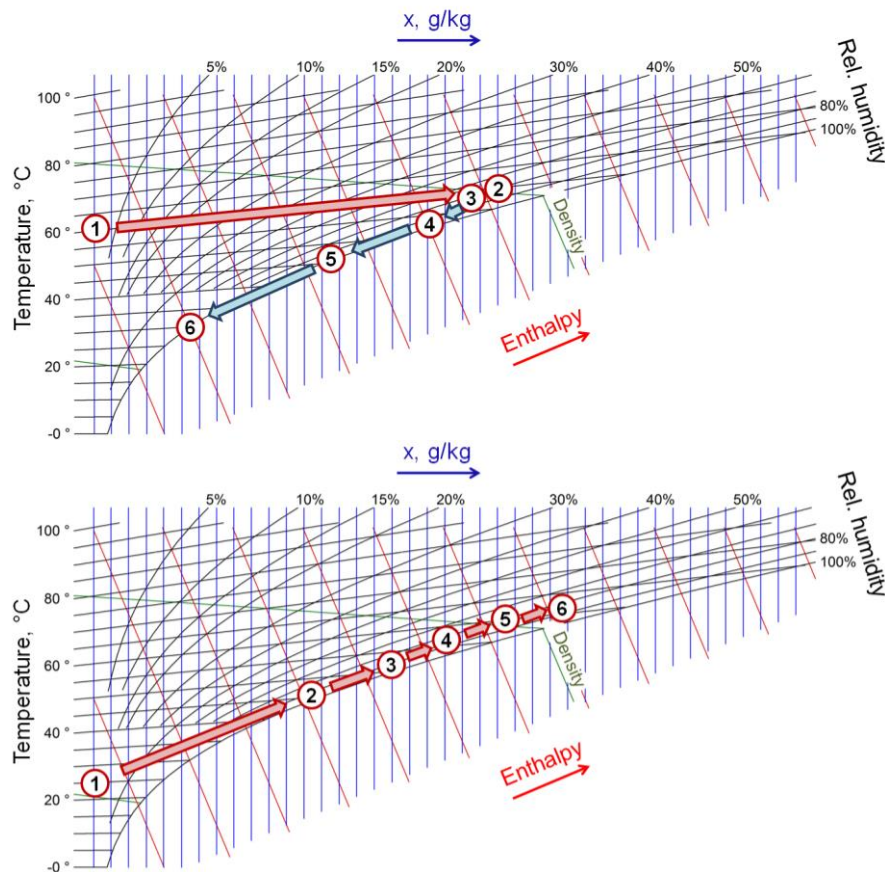
Figure 45. Mollier chart display of relative humidity distribution along the cell length for the anode (left) and cathode (right) side of the cell, VTFF dry reactants, at current density of 500 mAcm^{-2}. Point 1 represents the inlet of the anode/cathode, point 6 represents the outlet of the anode/cathode side, measuring points are before and after each of the five segments. Red arrow – increase in absolute humidity, blue arrow – decrease in absolute humidity.

The anode side RH, Figure 45. (above), shows similar trend in the absolute humidity increase and decrease, i.e. the net water flux through the membrane, to the ISO partially humidified case. However, since the temperature profile along the anode side is decreasing in the downstream direction, the relative humidity of the anode side is very close to 100%

along the entire flow field, as mentioned in the study of Kang et al. [36]. The anode side RH is strongly influenced on the back-diffusion, i.e. water transport mechanism from the cathode to the anode side of the cell. The back-diffusion water flux is inversely proportional to the membrane thickness. Therefore it can be manipulated by choosing the appropriate membrane thickness for establishment of close to 100% RH profile along the anode side as well. For this case, the RH close to 100% has been established along both sides of the membrane unintentionally, since the anode side RH was not previously measured for the VTFF case, and apparently the membrane used in this work (0.05 mm) thickness had just the right properties to achieve optimal performance of the cell, even superior than the fully humidified ISO case.

7.8   Comparison

The polarization curves for the 3 cases are shown in Figure 46. The polarization curves are slightly different when compared to the polarization curves in Figs. 3., 4. and 6. simply because the mentioned polarization curves are represented the averaged values of the polarization curves of each segment, measured via current shunts and prone to the temperature dependency of the ohmic resistance to the temperature of each segment, while the polarization curves shown in Figure 46. are measured by the fuel cell test station. Both cases show that the performance of the VTFF case is similar or superior to the performance of the fully humidified ISO case.
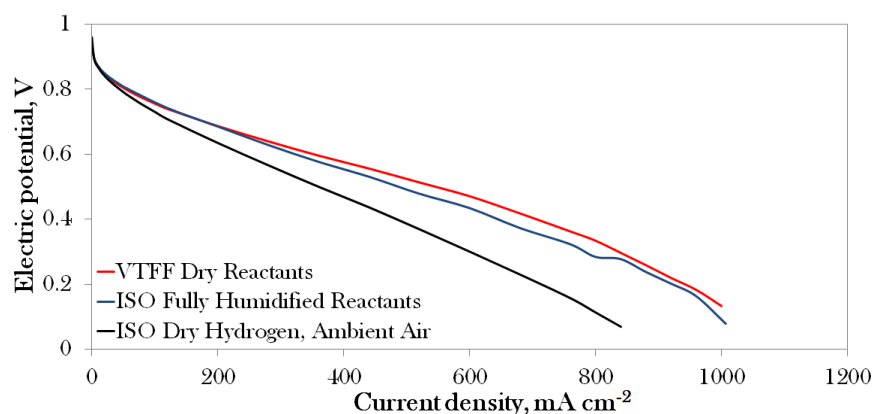
Figure 46. Polarization curve comparison.

Due to the limitations of the small active area of the cell, and the minimal mass flow rate of the test station, the VTFF setup will be investigated on a cell with higher active area and

more complex flow field in the future studies, while the desired temperature profile will be established by coolant mass flow rate control, thereby using internally generated heat as well as the generated water for achieving optimal performance of the cell without external humidification.

7.9   Conclusions

Variable temperature flow field PEM fuel cell operation without external humidification is compared to the fully humidified isothermal operation in this work for the first time. Regardless of the limitations of the experimental installation, the main conclusions of this work are:

The temperature distribution inside an operating PEM fuel cell is highly non-uniform and it cannot be defined by just one parameter. The measurement of the temperature and relative humidity should be done directly inside the reactant channels, because the temperature measured by the RH&T sensors placed on distance of 5 mm from the GDL substrate surface is significantly different. The temperature distribution along the anode and cathode channels is different in all cases. This shows agreement with the numerically obtained data in the previous chapters. However, in the experimental study the temperature inside the channels was lower when compared to the temperature of the current collectors due to the requirement for external heating of the cell since the active area was only 2500 mm^2.

It is possible to achieve 100% RH along the entire flow field with dry reactants at the cell inlet. Such operation along the cathode side can be achieved by prescribing the variable temperature flow field profile extracted from Mollier's *h-x* chart, and on the anode side by choosing the appropriate membrane thickness, thereby manipulating the back-diffusion water flux.

VTFF operation without external humidification is similar, or superior to the fully hydrated ISO operation. The variable temperature flow field temperature profile is basically linear, and therefore it can be easily achieved with coolant mass flow rate control, incorporating the use of internally generated water and heat for optimal cell performance. The increase in the performance when compared to fully humidified isothermal operation is a consequence

of the minimized mass transport losses, since the VTFF concept is based on evaporating the internally generated water for reactant humidification and achieving high membrane water content along the entire flow field.

The main conclusion is that the external humidifiers could be completely removed from the system, without compromising the cell performance. However, the application of the concept must be further experimentally investigated on a cell with higher active area with a more complex flow field.

8   VALIDATION   OF   THE   COMPUTATIONAL   FLUID DYNAMICS MODELS

8.1   Introduction

In order to validate the CFD models, the current density distributions along the cell length and relative humidity profiles along the anode and cathode side of the cell are compared with the experimentally obtained data, for isothermal and variable temperature flow field case.

The developed CFD models are studied for different membrane water content equations and water diffusion equations. The membrane water content models used in the simulations are Zawodzinski [18] and Scholz [95], while the diffusion models are Motupally [43] and Wu [96]. The electro-osmotic drag coefficient equation used in all cases is Springer [15].

8.2   Thorough validation

The complete validation is carried out using ANSYS Fluent 16.2. The CFD polarization curve comparison is carried out for three different current densities, 250, 500 and 750 mA cm^{-2}, shown in Figure 47. The CFD setup is very similar to the setup shown in chapter 6, with slightly altered membrane electrode assembly dimensions, as shown in Table 3., altered open-circuit voltage and the cathode reference exchange current density for each studied case.
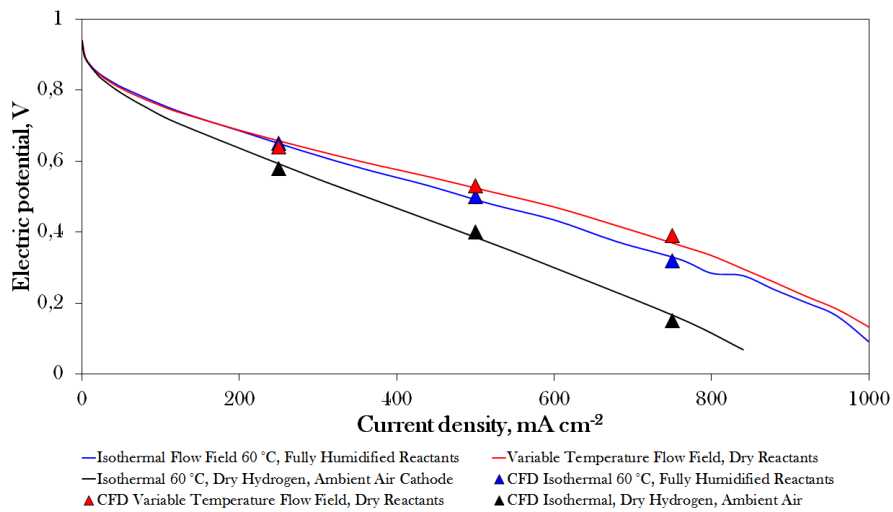
Figure 47. Polarization curve comparison, Fluent 16.2 vs exp. data.

It can be seen that there is a good agreement of the CFD data with experimentally obtained data for all studied cases.

In order to have insight in the current density distributions, the comparison is done for the isothermal 60 °C case, fed with dry hydrogen and ambient air and the variable temperature flow field case, at current density of 500 mA cm^{-2}. The comparison is not carried out for the isothermal 60 °C fully humidified case, because the relative humidity profiles could not be measured due to the overall relative humidity of 100%. The comparison is shown in Figure 48.
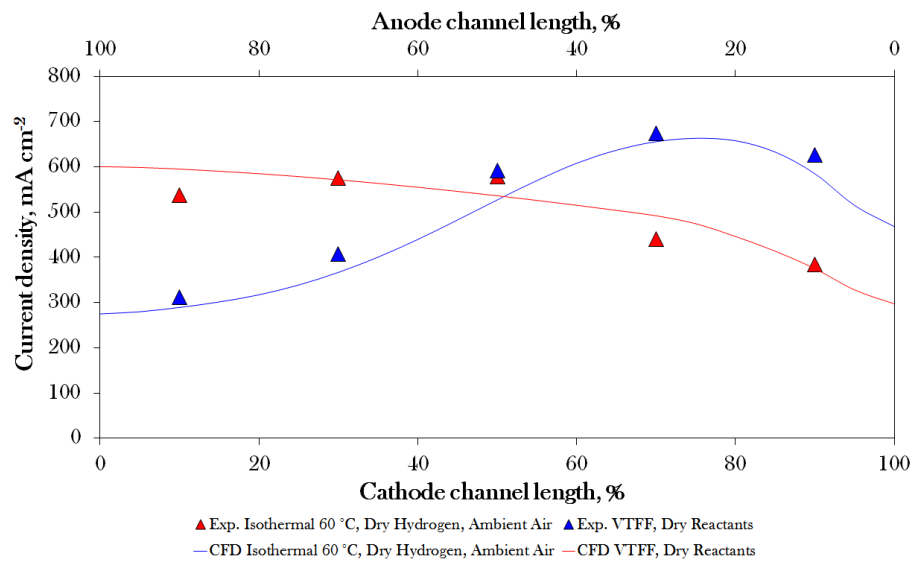
Figure 48. Comparison of CFD vs. exp. current density distributions along the cell, isothermal 60 °C vs. variable temperature flow field.

There is a good agreement of the CFD results with the experimentally obtained data for both cases, giving evidence that the Zawodzinski [18] membrane water content equation is validated.

The relative humidity profiles along the anode and cathode channels show good agreement with the experimentally obtained data for the isothermal case, as shown in Figure 49.
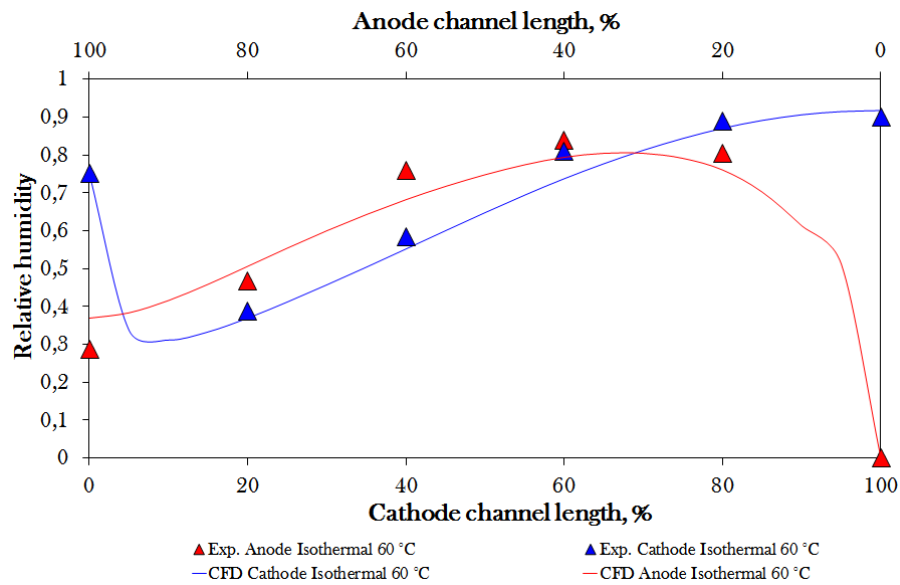
Figure 49. Comparison of relative humidity profiles along the anode and cathode channels, isothermal 60 °C, current density 500 mA cm^{-2}, exp. vs. CFD.

The relative humidity profiles along the anode and cathode channels also show good agreement with the experimentally obtained data for the variable temperature flow field case, as shown in Figure 50.
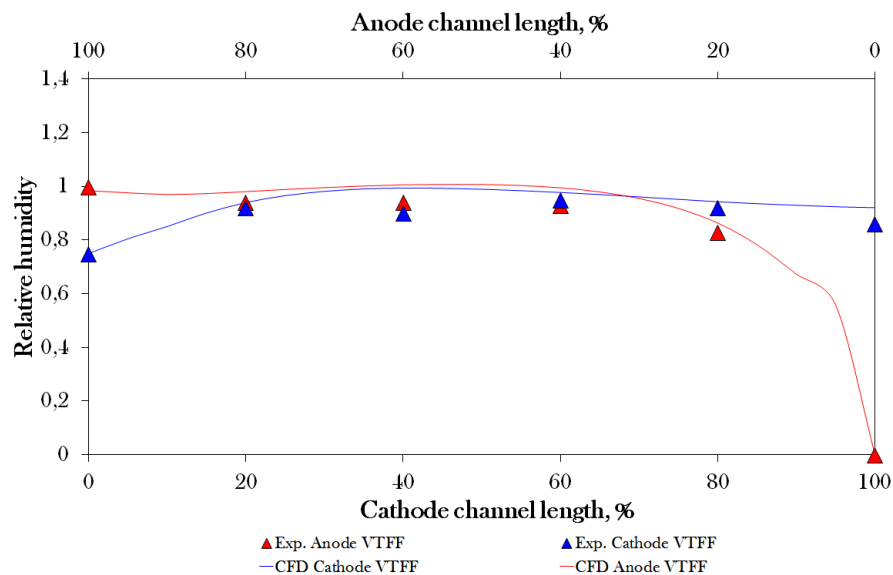
Figure 50. Comparison of relative humidity profiles along the anode and cathode channels, variable temperature flow field, current density 500 mA cm^{-2}, exp. vs. CFD.

8.3 Conclusions

The results obtained with Fluent 16.2 show very high level of agreement with the experimentally obtained data in all aspects. Therefore it can be concluded that the Zawodzinski [18] membrane water content model, coupled with Motupally [43] back-diffusion model and Springer [15] electro-osmotic drag coefficient model show the highest accuracy. The mentioned models will be used for analysis of five cell stack with coolant induced variable temperature flow field, in order to determine the influence of the coolant induced variable temperature flow field on the overall temperature distribution inside the stack and thereby gain insight in the performance of each cell.

9 COMPUTATIONAL FLUID DYNAMICS MODEL OF COOLANT INDUCED VARIABLE TEMPERATURE FLOW FIELD FOR PEM FUEL CELL STACK

9.1 Introduction

This chapter represents CFD analysis of a PEM fuel cell stack with coolant prescribed desired variable temperature flow field for the first time. The simulations are carried out for a five-cell short stack only for one operating point, due to very difficult convergence of the simulations. The difficult convergence is a consequence of setup of the fixed operating potential boundary condition (potentiostatic approach) which results in the operating current density close to the experimental one from study of Tolj et al. [8]. The polarization curve for single cell with coolant prescribed variable temperature flow field can be seen in the previous chapters. The problematic convergence of potentiostatic boundary conditions on the cathode current collector terminal is not quite clear. Since the temperature of the cell is highly inhomogeneous (temperature gradient of ca. 30 K along the 25 mm cell length), the inability for prescribing the galvanostatic boundary conditions, *i.e.* fixed current density, resulted in highly unstable convergence. This is due to the fact that the software calculates sink and source terms based on the current density, and since the current density is slowly converging to a stable value, the change in the current density during the convergence period leads to a change in the amount of generated heat inside the cell. The generated heat inside the cell directly influences the temperature profile of the coolant, since the coolant is heated up by the generated heat, and the temperature field directly affects the reactant relative humidity profile along the cell, *i.e.* the membrane water content. The solution for this problem was found by prescribing higher mass flow rate of the coolant in the beginning, with the initial temperature gradient of around 5 K along the cell. After the solution is converged, the mass flow rate of the coolant was increased by ca. 5 K by decreasing the coolant mass flow rate in a step like fashion, with full convergence achieved after each step. Increase in the temperature gradient during one step higher than 5 K led to divergence issues, but not in a classical manner, *i.e.* by divergence in the solver, but rather in the starvation-like behavior of the cell. The starvation-like behavior was apparent in the consumption of the hydrogen in the first half of the cell (in respect to the

anode inlet), and while the area-weighted average current density being monitored during the simulations was close to the experimental one, *i.e.* 500 mA cm^{-2}, the actual current density was very high in the area where the reactant was rapidly consumed, and zero in the rest of the cell length. This led to high reactant depletion, while the rest of the cell was starved. Even though the averaged value of current density was close to the experimental one, the distribution of the current density along the cell was quite different. Therefore, the above specified methodology for achieving convergence had to be introduced.

9.1 Methodology

9.1.1 Domains

The geometry of the model is based on the geometry of the experimental investigation of the variable temperature flow field concept from the single cell design from work of Tolj et al. [8]. Similar geometry is investigated in previous chapter, however the main difference in this work is further reduction in the monopolar plate thickness, and introduction of the coolant channels between the neighboring reactant channels, as well as the fact that this work deals with CFD analysis of the stack and the previous have been done for single cells. The geometry of the five cell short-stack is shown in Figure 51.
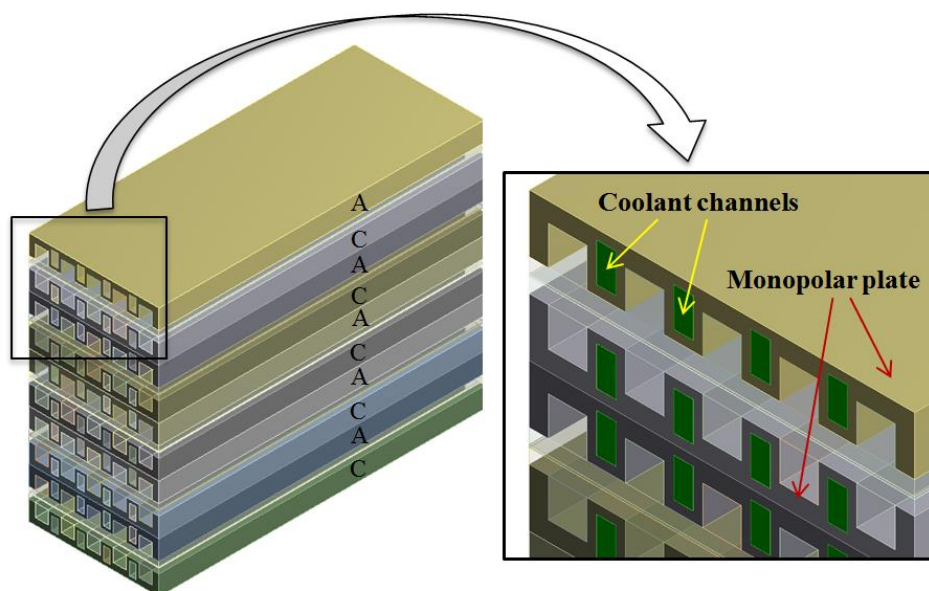
Figure 51. Modeling domains; annotation A represents the anode monopolar plate, while C represents the cathode monopolar plate

The design of the monopolar plates represents a simplified version of the industrially produced flow fields from sheet metal, where the channel geometry is pressed inside the sheet metal, and the back plate, *i.e.* the flat plate for the closure of the coolant channels is laser welded onto the flow field plate. The thickness of simulated sheet metal is chosen to be 0.25 mm. This design is beneficial for several reasons:

i) The stack monopolar plates can be mass produced without the necessity for machining

ii) The coolant channels are in close proximity to the reactant channels, and due to this reason the heat transfer is high even when low thermal conductivity materials are used (in this case stainless steel with thermal conductivity of 13 W m^{-1} K^{-1}), explained in detail in previous chapters

iii) The total stack height and weight are significantly reduced when compared to the original design with 10 mm end plate thickness

Geometry simplifications are evident in 90° angles of the reactant channels, while the industrially produced sheet metal end plates have different angles due to the fact that the sheet metal matrix must be easily pulled out of the work piece.

9.1.2 Mesh

The introduced simplifications are also beneficial during the mesh setup, and enable simple setup of a structured mesh with the highest attainable cell orthogonal quality, as seen in Figure 52.
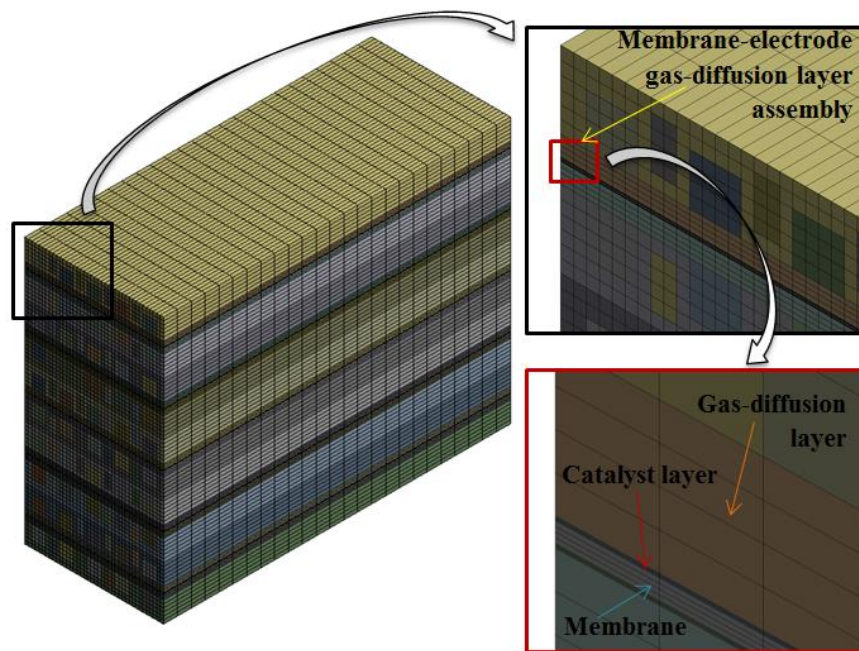
Figure 52. Mesh with annotated details

The membrane-electrode assembly, gas-diffusion layer, and reactant channel cross-sections geometry parameters are identical to the geometry specifications from the work of Tolj et al. [8] to enable validation of the model and comparison of the simulation results with the experimental data, however the cell total length was reduced to 25 mm (vs. the original single cell length of 200 mm) to reduce the computational requirements. The geometry details are shown in the following chapter in Table 3. The mesh setup is very similar to the one used in the previous chapters, with the difference in the coolant channel number of cells across the channel width. The dimensions of the coolant channels are 0.5 mm × 1 mm, and the edge sizing is set to 0.25 mm.

9.2   Governing equations and boundary conditions

For the governing equations, please see the previous chapters. The operating parameters are shown in Table 4.

Table 4. Operating parameters.

Parameter	Values
Cathode stream abs. pressure	1.01325 bar
Anode stream abs. pressure	1.01325 bar
Cathode stream inlet temperature	30 °C
Anode stream inlet temperature	25 °C
Coolant inlet temperature	30°C
Fuel cell temperature	60°C vs. coolant prescribed variable
Relative humidity of cathode stream inlet	0.75
Relative humidity of anode stream inlet	dry
Current density	Close to 500 mA cm^{-2} (potentiostatic)
Stoichiometry, cathode	2.15
Stoichiometry, anode	1.2
Flow configuration anode vs. cathode	Counter-flow
Flow configuration cathode vs. coolant	Co-flow
End plate thickness	Two sheets of metal, each 0.25 mm thick,
Channel length	25 mm
Reactant channel width at anode and cathode	1 mm
Channel height at anode and cathode	1 mm
Coolant channel width	0.5 mm
Coolant channel height	1 mm
Membrane thickness (Nafion 212)	0.05 mm
Catalyst layer thickness	0.01 mm
Platinum loading	0.5 mg cm^{-2}
Gas-diffusion layer thickness	0.38 mm
Effective area	250 mm^2
Membrane dry density	2 g cm^{-3}
Membrane molecular weight	1100 g mol^{-1}

9.2.1 Domain boundary conditions

The domain type for all domains is defined as fluid bodies, except for current collectors which are defined as solid bodies. As already mentioned, in the work of Tolj et al. [8] the current collector material was stainless steel 316L, therefore this material was selected in this study as well.

9.2.2 Inlet boundary conditions

The mass flow inlet boundary condition is defined for the anode and cathode inlets. The anode inlet dry hydrogen temperature was set to 25 °C. Cathode inlet air temperature was set to 30 °C, with a relative humidity of 0.75. The anode mixture of gases consisted of hydrogen and water vapor (while the mass fraction of water vapor was set to zero on the anode inlet). The cathode mixture of gases consisted of nitrogen, oxygen and water vapor. The mass flow rate of the coolant is prescribed to result in a temperature profile close to the water vapor saturation profile. The coolant is deionized water, and the mass flow rate of the coolant was calculated to result in the desired temperature profile for each current density separately.

9.2.3 Outlet boundary conditions

On the anode and cathode reactant and coolant channel outlets, the pressure outlet boundary condition is applied with a zero gauge pressure and backflow total temperature set according to the temperature field setup.

9.2.4 Wall boundary conditions

Non-slip boundary conditions were applied to the walls. The temperature was fixed on the terminals of the anode and cathode current collectors for isothermal temperature field study. For coolant induced variable temperature field case, the walls are defined as adiabatic surfaces, and the resulting temperature profile is defined by the coolant mass flow rate. The electric potential on the anode terminals was set to zero. On the cathode terminals different values of electric potential are defined in order to extract the polarization curve point depending on the temperature profile prescribed by the coolant, *i.e.* isothermal vs. variable temperature flow field. The remaining surfaces are defined as walls by default.

9.2.5 Prescribing the desired temperature profile

Prescribing the desired temperature profile is done by controlling the mass flow rate of the coolant liquid − deionized water, which is in the co-flow direction with the cathode air. The mass flow rate $\dot{m}$ of the coolant is determined by expression

$$\dot{m} = \frac{\dot{Q}}{c_{\mathrm{w}} \Delta T} \tag{39}$$

where $\dot{Q}$ represents generated heat and water phase change enthalpy, c_{w} represents specific heat of the coolant, and ΔT represents the desired temperature difference between the outlet and inlet of the coolant liquid, respectively.

The generated heat is defined by a heat source term S_{h} inside the software by expression

$$S_{\mathrm{h}} = h_{\mathrm{react}} - R_{\mathrm{an,cat}} \eta_{\mathrm{an,cat}} + I^2 R_{\mathrm{ohm}} + h_{\mathrm{L}} \tag{40}$$

where h_{react} is the amount of heat released from the electrochemical reaction of hydrogen and oxygen on the triple-phase boundaries inside the cathode catalyst layer, while $R_{\mathrm{an,cat}}$ represent the anode/cathode over-potential, $\eta_{\mathrm{an,cat}}$ transition current, I is the total electrical current, R_{ohm} are ohmic losses, and h_{L} is the phase change enthalpy of water evaporation/condensation. The term h_{L} is neglected during the simulations, since the CFD model is single-phase. Nomenclature and symbols are adopted from the software manual [12].

9.3 Results and discussion

Two separate case studies have been carried out, isothermal and variable temperature flow field, established by coolant mass flow rate control.

9.3.1 Temperature

The isothermal case study was done by prescribing high mass flow rate of the coolant set at the inlet temperature of 60 °C, *i.e.* 333 K. The variable temperature flow field was prescribed by determining the required mass flow rate of the coolant to result in the desired temperature profile extracted from Mollier's *h-x* chart, as seen the previous chapters. The temperature contours of the outer walls of the stack are shown in Figure 53.
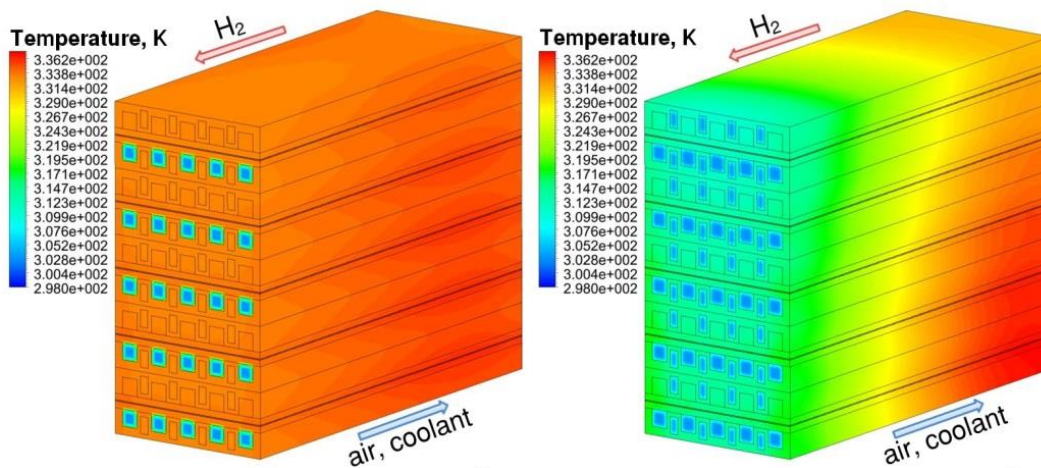
Figure 53. Temperature contours on the outer walls of the stack for isothermal (left) and variable temperature flow field (right) case at averaged current density close to 500 mA cm^{-2}.

It can be seen that the temperature field is not very homogeneous even for the isothermal case study with the prescribed high mass flow rate of the coolant, evident from the slight increase in the temperature from the top (cell #1) to the bottom (cell #5). This is more pronounced in the variable temperature flow field case Figure 53. (right). The reason for temperature inhomogeneity is simply caused by defining adiabatic outer walls. The coolant channels are placed between each of the neighboring reactant channels, as previously seen in Figure 51. Since the heat is generated inside the cathode catalyst layer, the cathode side of cell #1 causes the rise in temperature along the anode side of the neighboring cell, *i.e.* cell #2. This is also evident in the isothermal case, but it is far less pronounced since the mass flow rate of the coolant is quite high. Quite similar temperature inhomogeneity for the isothermal case can be seen in work of Liu et al. [52], even though the mentioned work represents quite simplified PEM fuel cell stack model due to the computational limits of the time when the work was published.

In Figure 54. the temperature distributions are shown along the reactant channels for each cell. The temperature is extracted from a symmetry line passing through the middle channel of each cell for the anode and cathode side. It can be seen that closer placement of the coolant channels to the reactant channels results in very uniform temperature distribution along the reactant channels, and the operating temperature of 333 K is reached very quickly upon entry of the reactant gases, unlike the case in the previous chapters

where 10 mm thick current collector plates have been used, and resulted in a difficult temperature boundary condition setup at the current collector terminals.
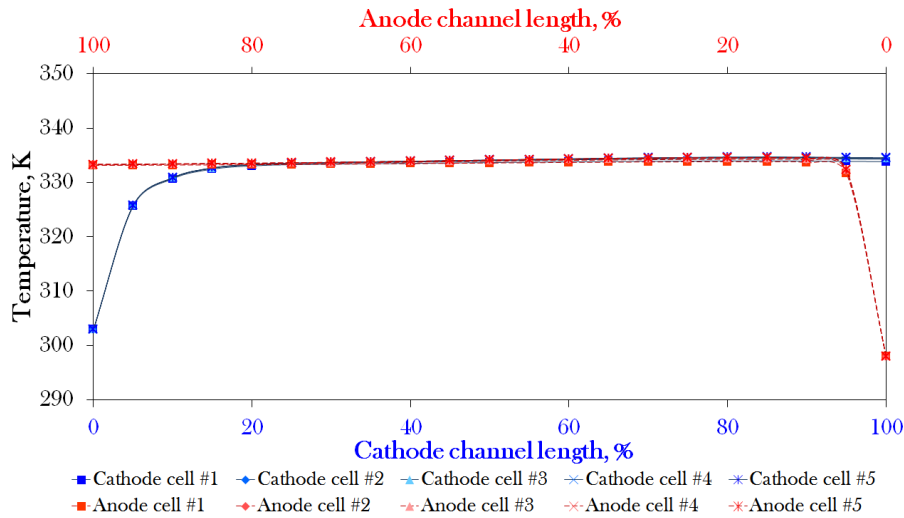
Figure 54. Temperature distribution along the anode and cathode channels of each cell in the stack for variable temperature flow field case at electric potential of 3.1 V and current density close to 500 mA cm⁻².

Thick current collector plates resulted in higher temperature profile along the reactant channels by up to 5 K for similar current density (500-550 mA cm^{-2}) and the boundary conditions in that case has to be adjusted to establish the desired temperature profile along the reactant channels. Therefore, it is easier and more accurate to prescribe the isothermal boundary conditions with the coolant channels in close proximity to the reactant channels. Even though, in Figure 54., it has been shown that there is a minor degree of temperature increase towards the cell #5, this is hardly noticeable in the temperature distributions in Figure 54.

In Figure 55. the temperature distributions are shown along the middle channels of the anode and cathode of each cell for the variable temperature flow field case.
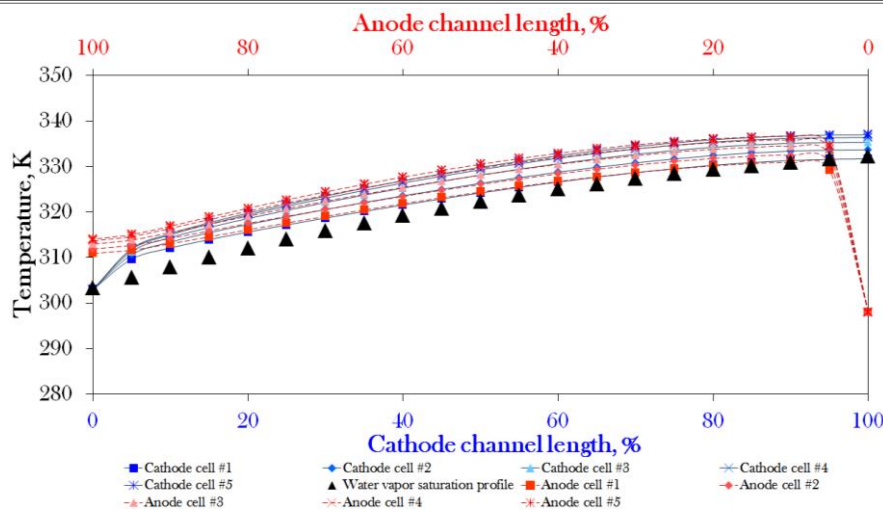
Figure 55. Temperature distribution along the anode and cathode channels of each cell in the stack for variable temperature flow field case at electric potential of 3.3 V and current density close to 500 mA cm^{-2}.

Unlike the uniform temperature distribution seen in Figure 54., the temperature inside the reactant channels tends to increase from cell #1 (top cell) to cell #5 (bottom cell), for the reasons specified in the previous chapter. Previously carried out numerical simulations with thicker current collector plates have shown that there is additionally a significant difference between the temperature profiles along the anode and cathode channels, due to high difference in mass flow rates of the reactants. The cathode air in the previous study was heating up slower when compared to the anode hydrogen. But, in this case, this is not pronounced due to very close proximity of the coolant channels to the reactant channels. The temperature profiles along different cells show similarity with the desired temperature profile – water vapor saturation profile extracted from Mollier's *h-x* chart. In order to reduce the difference in the temperature of the adjacent cells, a simple manifold design with variable cross-section could be introduced. Introduction of such system would lead to the notion that every cell in the stack would have the temperature profile very similar to the one investigated in a previous study for a single cell, therefore this was not introduced in this work.

9.3.2 Relative humidity

In Figure 56. the relative humidity distributions are shown along the membrane mid-planes for each cell. It can be seen that the variable temperature flow field case results in close to 100% relative humidity along the entire flow field.
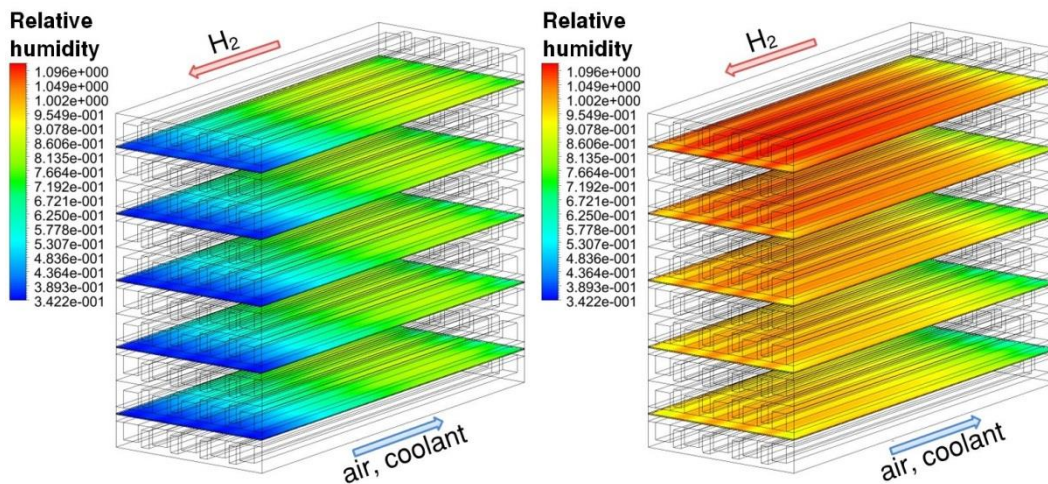
Figure 56. Relative humidity contours on membrane mid planes for isothermal (left) and variable temperature flow field (right) case at current density close to 500 mA cm^{-2}, the top cell is cell #1.

It can also be observed that the relative humidity exceeds the value of 1 (100% relative humidity) even though the model is multiphase, however this is not relevant for this study. The relative humidity distributions for the isothermal case, Figure 56. (left), show a region of low relative humidity near the air inlet. This happens due to the sudden increase in the temperature of the reactants upon entry to the cell, *i.e.* the rise in temperature from 298 K for the anode and 303 K for the cathode to 333 K, and insufficient amount of generated water to achieve high relative humidity of the reactants upon entering the cell, even though the relative humidity reaches a value close to 1 at the cathode outlet. The result is a dehydrated membrane with poor ionic conductivity in most part of the cell length.

In Figure 57. The relative humidity profiles are shown for the anode and cathode channels of each cell, extracted from the mid channel symmetry line.
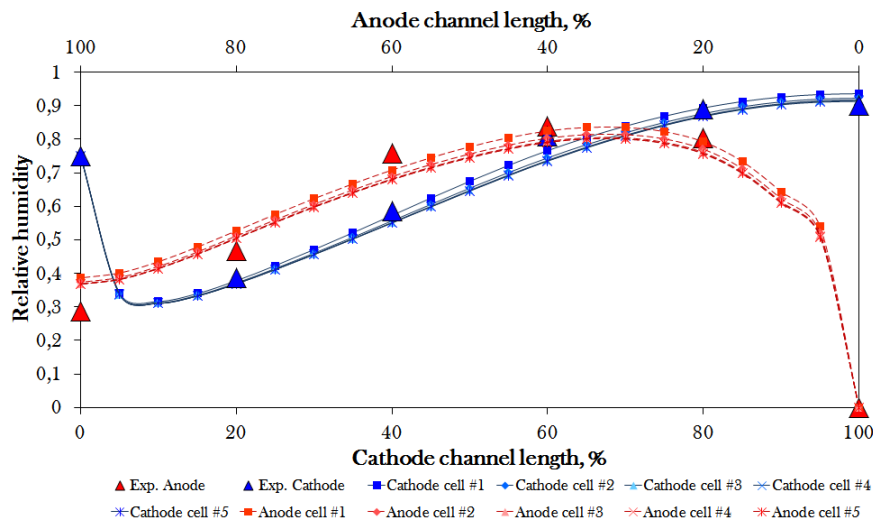
Figure 57. Relative humidity distribution along the anode and cathode channels of each cell in the stack for isothermal case at electric potential of 3.1 V and current density close to 500 mA cm^{-2}.

The comparison between the cathode relative humidity profiles with the experimental data shows very good agreement for all cells in the stack.

In Figure 58. the relative humidity profiles are shown along the reactant channels for the variable temperature flow field case. It can be seen that the relative humidity along the reactant channels increases from the bottom (cell #5) to the top (cell #1) of the stack.
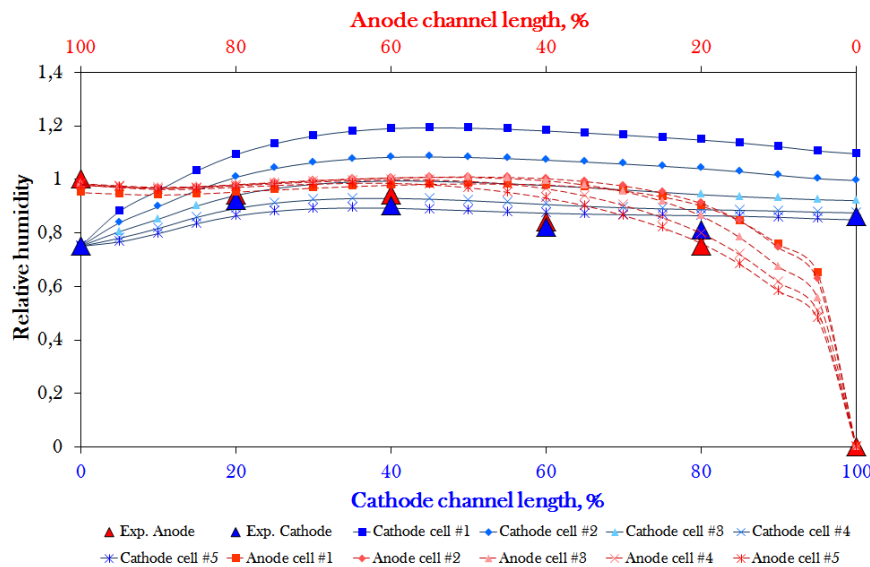
Figure 58. Relative humidity distribution along the anode and cathode channels of each cell in the stack for variable temperature flow field case at electric potential of 3.3 V and current density close to 500 mA cm^{-2}.

This is simply caused by slightly different temperature profiles along the reactant channels, as seen previously in Figure 55., *i.e.* for the equal amount of generated water, lower temperature along the channel results in higher relative humidity, since the water vapor saturation profile is dominantly temperature dependent parameter (since the change in the operating pressure is very low – the stack is only 25 mm long). It is interesting to see that the anode side hydration is quite high, since the relative humidity profile along the anode side (fed at the inlet with dry hydrogen) reaches relative humidity of 1 along the most part of the cell length. This is caused by back diffusion, which can be manipulated by changing the membrane thickness. The overall relative humidity profiles show high level of agreement with the experimentally obtained data, especially for the middle cells of the stack. However the temperature distributions along each cell are slightly different and therefore the relative humidity profiles are also different for each cell.

9.3.3 Membrane water content

High relative humidity along both sides of each cell results in high ionic conductivity of the membrane, *i.e.* high membrane water content, as previously mentioned and seen in

Figure 59., and consequently high performance of the stack without the necessity for external humidification.
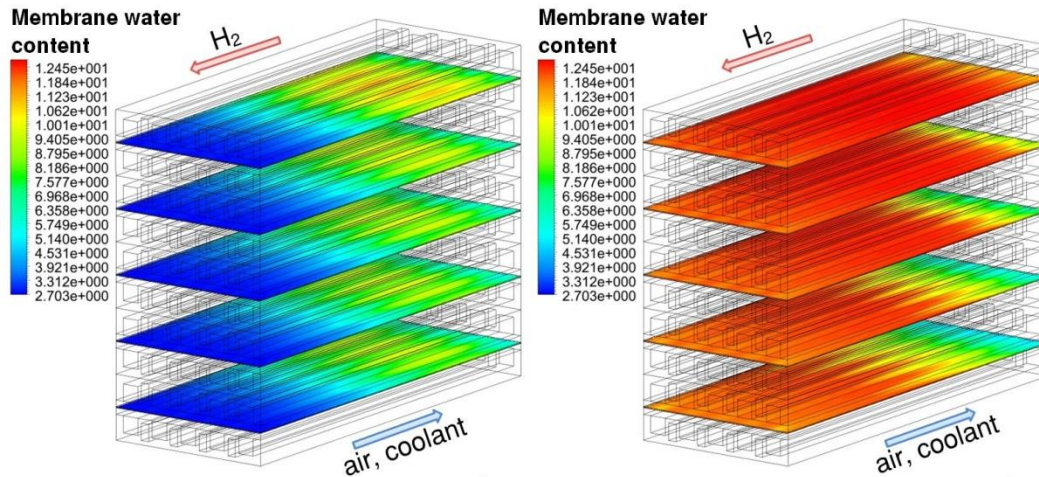
Figure 59. Membrane water content contours on membrane mid planes for isothermal (left) and variable temperature flow field (right) case at current density close to 500 mA cm^{-2}, the top cell is cell #1.

High membrane water content is achieved by manipulating the temperature profiles along the reactant channels to result in high relative humidity along the entire flow field. The membrane water content for the isothermal case, Figure 60., is very low in most part of the flow field, while the membrane water content in the variable temperature flow field case is quite high along the entire flow field. To further increase the membrane water content profiles of the bottom cells, a previously mentioned variable cross-section manifold can be used.
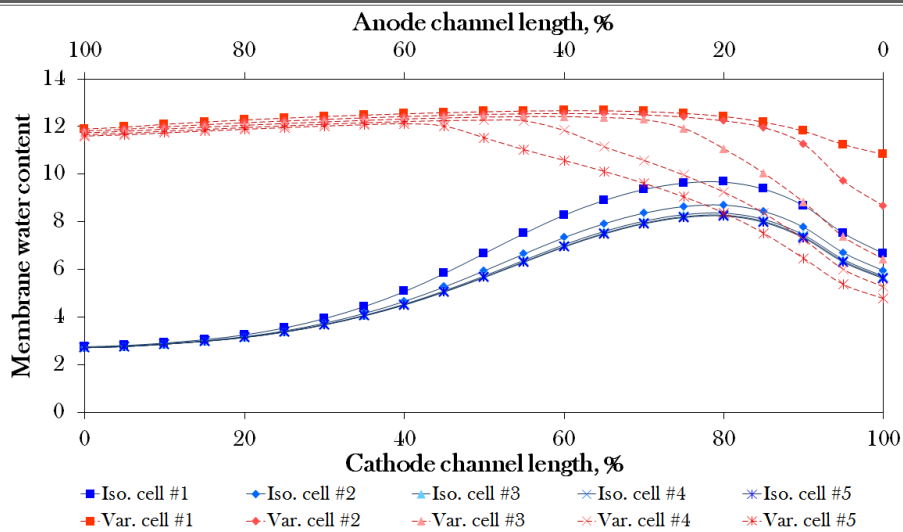
Figure 60. Membrane water content distributions along the membrane symmetry lines for each cell for isothermal (electric potential 3.1 V) and variable temperature flow field (electric potential 3.3 V) case at current density close to 500 mA cm^{-2}.

9.3.4 Current density

The current density contours are shown in Figure 61. It can be seen that the highest local current density is evident in the isothermal case (left) beneath the lands in the region with the highest relative humidity, *i.e.* the highest membrane water content, as seen previously in Figure 60.
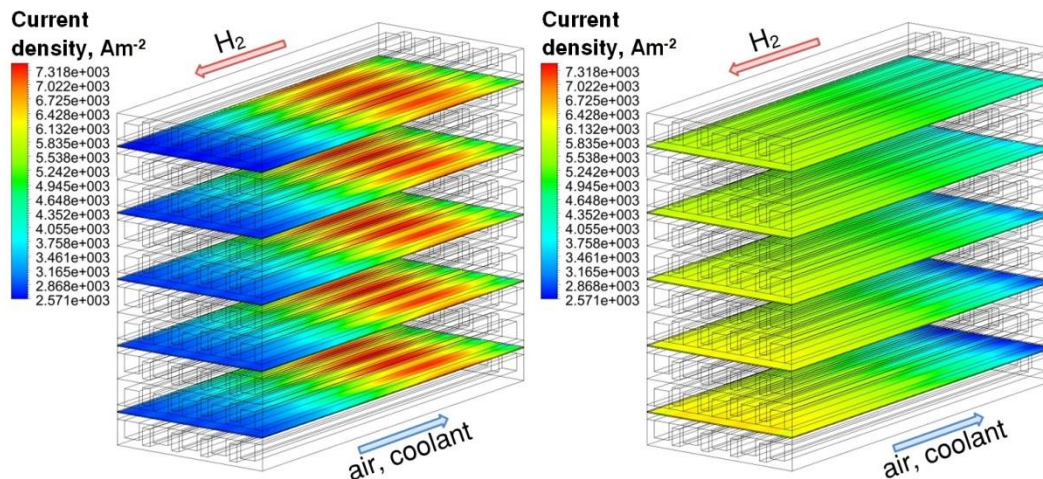
Figure 61. Current density contours on membrane mid planes for isothermal (left) and variable temperature flow field (right) case at current density close to 500 mA cm^{-2}, the top cell is cell #1.

This results in non-uniform heat and water generation along the cell, and results in higher degradation rates. The variable temperature field case shows more uniform current density distribution, with the lowest current density at the anode hydrogen inlet of the bottom cells. This is caused by an increase in the overall temperature of the cells from the top to the bottom of the stack, as previously explained, resulting in lower relative humidity and membrane water content in the specified regions.

In Figure 62. the current density distributions are shown along the membrane symmetry line for each cell for isothermal and variable temperature flow field case with quite good agreement with the experimentally obtained data. It can be observed that for the isothermal case setup, the top cell (cell #1) shows slightly higher performance when compared to other cells in the stack.
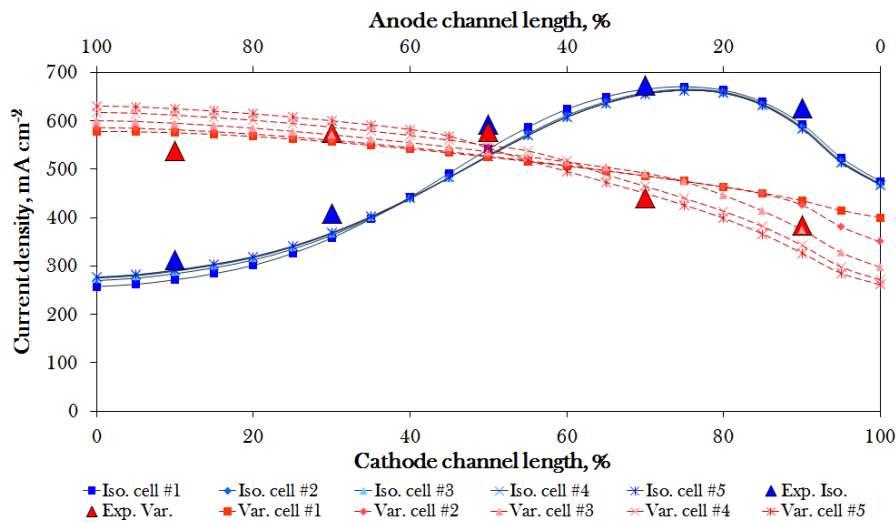
Figure 62. Current density distributions along the membrane symmetry lines for each cell for isothermal (electric potential 3.1 V) and variable temperature flow field (electric potential 3.3 V) case at current density close to 500 mA cm^{-2}.

Similar observation is seen in the work of Shimpalee et al. [53], where the highest performance for the case setup is seen for the top and bottom cell. The reason for higher performance of the bottom cell in the mentioned work is the fact that the bottom of the stack was mounted on a thick metal plate, which results in higher heat transfer of the bottom cell and consequently the lower temperature of the bottom cell. Performance of each cell in the mentioned work has higher difference due to the fact that the resulting mass flow rate of the coolant established a slight temperature gradient across the stack, while in this work, the mass flow rate of the coolant is much higher and the difference between the performance of the neighboring cells is less obvious, except for the cell #1.

9.4   Conclusions

Isothermal and variable temperature field operation of a 2.5 cm^2 active area five cell short PEM fuel cell stack has been modeled with very good agreement of the relative humidity profiles with the new experimental data. It was noted that the non-uniform temperature distribution along the stack height is considerable in the variable temperature flow field case. In order to further improve the performance of the stack, without excessive water accumulation, especially for higher number of cells, a manifold with variable cross-section may be required introduced. The introduced thinner monopolar plates and the coolant channels between the adjacent cells of the anode and cathode side result in much better control of the temperature profile along the channel length, and reduce the material costs and the overall volume of the stack.

The overall conclusions are that CFD modeling gives quite detailed insight in the stack parameters which could hardly be observed experimentally. The model shows good agreement of the trends of individual cell performance in regard to their position in the stack, which show good agreement with the trends of the experimental measurements and numerical analysis results from other works dealing with CFD analysis of PEM fuel cell stacks [52-54] with the corresponding explanations of the observed phenomena in the previous chapters of this work. Since this is the first CFD model of a stack with a prescribed variable temperature flow field, the results are useful for development of the experimental stack setup.

However, since there are many interesting phenomena observed in the CFD analysis so far even for simple flow field geometry modeled in this work, a more complex flow field will be studied in the future. The main contribution of this thesis is the development of the method for application of the variable temperature flow field on a stack level, successfully demonstrated numerically in this chapter, with high level of agreement with the new experimental data in all aspects. The application of the variable temperature flow field on a PEM fuel cell stack will enable wider operating range and minimization of the mass transport losses at higher currents (due to the fact that the generated water is evaporated in the stream of reactants) without the necessity for external humidification.

10   SIGNIFICANT CONTRIBUTIONS

Contributions of this thesis in the field of PEM fuel cell research and development are:

1. Development of innovative and reliable 3D CFD model of PEM fuel cell and interactive application of the model for the research of the variable temperature flow field concept applied on single cell and stack level under different operating conditions.

2. Development of original and unique experimental installation of a segmented PEM fuel cell with capability of individual control of temperature on each segment along the anode and cathode side of the cell, measurement of current density distribution on each segment and measurement of temperature and relative humidity between the neighboring segments, which enables calibration and thorough validation of the developed 3D CFD models.

3. Novel capability of application of the variable temperature flow field on an operating PEM fuel cell with simultaneous, in-situ and operando, monitoring and data acquisition of the relative humidity profiles along the anode and cathode channels, current density distribution along the entire flow field, and temperature distributions along the reactant channels and current collector terminals, in real time.

4. Development of an innovative method for establishing and maintaining the desired variable temperature profile along the entire flow field by coolant mass flow rate control, applicable on a PEM fuel cell single cell and stack level, in such manner that the relative humidity of the reactants is close to 100% along the entire flow field without the requirement for external humidification, applicable for different operating conditions and operating currents.

11   CONCLUSIONS

This thesis shows that the coolant induced variable temperature flow field can be established and maintained for the PEM fuel cell stack for the first time. Operation under variable temperature flow field on the newly developed experimental setup has shown higher performance than the conventional fully humidified isothermal operation for the first time as well.

This is a result of synergy by using both products of the electrochemical reaction inside PEM fuel cells, internally generated water and heat, for improvement of the PEM fuel cell efficiency. Close to 100% relative humidity can be established along the entire flow field even with completely dry reactants. The cathode side close to 100% relative humidity is established and maintained by gradually heating up the cathode air, and humidifying the stream with the generated water. The anode side close to 100% relative humidity is established and maintained by using the back-diffusion water transport mechanism which results in the anode side hydration, and by gradually decreasing the temperature profile in the anode downstream direction. Simply by prescribing variable temperature flow field and by choosing the appropriate membrane thickness, this concept can be applied for PEM fuel cell stack operation, as demonstrated by CFD analysis of a PEM fuel cell stack with coolant induced variable temperature flow field.

The coolant induced variable temperature flow field is elegantly established by gradually heating up the coolant fluid, and it can be established and maintained for any current density. The limitations of the coolant induced variable temperature flow field are the minimal mass flow rate of the circulation pump, and insufficient amount of generated heat inside the cell at low current densities, but these are only encountered on relatively small active area cells and the cells rarely operate on low current densities due to increased membrane degradation during such operation.

The CFD analysis has shown to be a tool of paramount importance for determining the required temperature profile by gradually increasing the temperature of the coolant in the cathode downstream direction. The CFD analysis results have shown very high level of agreement with the experimentally obtained data due to the incorporated robust models of membrane water content and membrane water transport. The newly developed experimental setup can be used for determining the water transport and membrane water

content models best suited for membranes of different manufacturers and full-scale validation of the developed CFD models.

The goal of the future studies is to develop a commercial PEM fuel cell stack with incorporated coolant induced variable temperature flow field. The developed stack will be characterized by high performance, lower price and maintenance requirements when compared to other commercial cells, wider operating range, and minimal mass transport losses.

For a more detailed insight in the discussed topics, please refer to the conclusions of each previously presented chapter.

BIBLIOGRAPHY

[1] Barbir F. PEM fuel cells, 2nd edition: theory and practice. Academic Press 2012.

[2] EG&G Technical Services, Inc. Fuel cell handbook. U.S. Department of Energy; 2004.

[3] Zheng CH, Oh CE, Park YI, Cha SW. Fuel economy evaluation of fuel cell hybrid vehicles based on equivalent fuel consumption. Int J Hydrogen Energy 2012;37:1790-6.

[4] Hwang J, Chen Y, Kuo J. The study on the power management system in a fuel cell hybrid vehicle. Int J Hydrogen Energy 2012;37:4476-89.

[5] Simons A, Bauer C. A life-cycle perspective on automotive fuel cells. Appl Energy 2015;157:884-96.

[6] Larminie J. Fuel cell systems explained. West Sussex: Wiley; 2002.

[7] Konno N., Mizuno S., Nakaji H., Ishikawa Y. Development of Compact and High-Performance Fuel Cell Stack. SAE Int. J. Alt. Power 2015;4(1):123-129.

[8] Tolj I, Bezmalinovic D, Barbir F. Maintaining desired level of relative humidity throughout a fuel cell with spatially variable heat removal rates. J Hydrogen Energy 2011;36:13105-13.

[9] Kulikovsky AA, Divisek J, Kornyshev AA. Modeling the cathode compartment of polymer electrolyte fuel cells: Dead and active reaction zones. J Electrochem Soc 1999;146(11):3981-91.

[10] Mazumder S, Cole JV. Rigorous 3-D mathematical modeling of PEM fuel cells II. Model predictions with liquid water transport. J Electrochem Soc 1999;150(11):A1510-17.

[11] Sukkee U, Wang CY, Chen KS. Computational fluid dynamics modeling of proton exchange membrane fuel cells. J Electrochem Soc 1991;147(12):4485-93.

[12] ANSYS, Inc. ANSYS Fluent 12.0 Fuel Cells Module Manual. ANSYS, Inc. 2009.

[13] Nam JH, Karviany M. Effective diffusivity and water-saturation distribution in single- and two-layer PEM FUEL CELL diffusion medium. I Journal Heat Mass Transfer 2003;46(24):4595-11.

[14] Nguyen TV. Modeling two-phase flow in the porous electrodes of proton exchange membrane fuel cells using the interdigitated flow fields. Tutorials in electrochemical engineering mathematical modeling 1999;99(14):222-41.

[15] Springer TE, Zawodzinski TA, Gottesfeld S. Polymer electrolyte fuel cell model. J Electrochem Soc 1991;138(8):2334-41.

[16] Brandon ME. One-dimensional, transient model of heat, mass, and charge transfer in proton exchange membranes 2001. M.S. Thesis.

[17] Yousfi-Steiner N, Mocoteguy Ph, Candusso D, Hissel D, Hernandez A, Aslaindes A. A review on PEM degradation associated with water management: Impacts, influent factors and characterization. J Power Sources 2008;183:260-74.

[18] Zawodzinski TA, Derouin C, Radzinski S, Sherman RJ, Smith VT, Springer TE, et al. Water uptake by and transport through Nafion 117 membranes. J Electrochem Soc 1993;140:1041-7.

[19] Zhang J, Tang Y, Song C, Cheng X, Zhang J, Wang H. PEM fuel cells operated at 0% relative humidity in the temperature range of 23–120°C. Electrochimica Acta 2007;52:5095-101.

[20] Guvelioglu GH, Stenger HG. Flow rate and humidification effects on a PEM fuel cell performance and operation. J Power Sources 2007;163:882-91.

[21] Song C, Chua JC, Tang Y, Zhang J, Zhang J, Li J et al. Voltage jump during polarization of a PEM fuel cell operated at low relative humidities. J Hydrogen Energy 2008;33:2802-07.

[22] Saleh MM, Okajima T, Hayase M, Kitamura F, Ohsaka T. Exploring the effects of symmetrical and asymmetrical relative humidity on the performance of H2/air PEM fuel cell at different temperatures. J Power Sources 2007;164:503-09.

[23] Jeon DH, Kim KN, Baek SM, Nam JH. The effect of relative humidity of the cathode on the performance and the uniformity of PEM fuel cells, J Hydrogen Energy 2011;36:12499-511.

[24] Bi W, Sun Q, Deng Y, Fuller TF. The effect of humidity and oxygen partial pressure on degradation of Pt/C catalyst in PEM fuel cell. Electrochimica Acta 2009;54:1826-33.

[25] Huang X, Solasi R, Zou Y, Feshler M, Reifsnider K, Condit D et al. Mechanical endurance of polymer electrolyte membrane and PEM fuel cell durability. J Polymer Science 2006;16:2346–57.

[26] Yin C, Gao J, Wen X, Xie G, Yang C, Fang H, Tang H. In situ investigation of proton exchange membrane fuel cell performance with novel segmented cell design and a two-phase flow model. Energy 2016;113:1071-89.

[27] Weng FB, Jou BS, Li CW, Su Ay, Chan SH. The effect of low humidity on the uniformity and stability of segmented PEM fuel cells. J Power Sources 2008;181:251–8.

[28] Chen YS, Peng H. A segmented model for studying water transport in a PEM FUEL CELL. J Power Sources 2008;185:1179-92.

[29] Weng FB, Hsu CY, Li CW. Experimental investigation of PEM fuel cell aging under current cycling using segmented fuel cell. J Hydrogen Energy 2010;35:3664-75.

[30] Abdullah AM, Okajima T, Mohammad AM, Kitamura F, Ohsaka T. Temperature gradients measurements within a segmented H_2/air PEM fuel cell. J Power Sources 2007;172:209-14.

[31] Berg P, Promislow K, Stumper J. Discharge of a segmented polymer electrolyte membrane fuel cell. J Fuel Cell Science and Technology 2005;2:111-21.

[32] Zhang G, Kandlikar SG. A critical review of cooling techniques in proton exchange membrane fuel cell stacks. J Hydrogen Energy 2012;37:2412-29.

[33] Chen FG, Gao Z, Loutfy RO, Hecht M. Analysis of optimal heat transfer in a PEM fuel cell cooling plate. Fuel Cells 2003;3(4):181-8.

[34] Mench MM. Fuel cell engines. Hoboken: John Wiley & Sons; 2008.

[35] Wilkinson DP, Voss HH, Fletcher NJ, Johnson MC, Pow EG. Electrochemical fuel cell stack with concurrent flow of coolant and oxidant streams and countercurrent flow of fuel and oxidant streams. US Patent 5773160; 1998.

[36] Kang S, Min K, Mueller F, Brouwer J. Configuration effects of air, fuel, and coolant inlets on the performance of a proton exchange membrane fuel cell for automotive applications. J Hydrogen Energy 2009;34:6749-64.

[37] Ozden E, Tolj I, Barbir F. Designing heat exchanger with spatially variable surface area for passive cooling of PEM fuel cell. Applied Therm Eng 2013;51(1-2):1339-44.

[38] Hinatsu JT, Mizuhata M, Takenaka H. Water uptake of perfluorosulfonic acid membranes from liquid water and water vapor. J Electrochem Soc 1994;141:1493-8.

[39] Yang C, Srinivasan S, Bocarsly AB, Tulyani S, Benziger JB. A comparison of physical properties and fuel cell performance of Nafion and zirconium phosphate/Nafion composite membranes. J Membrane Science 2004;237:145-61.

[40] Husar A, Higier A, Liu H. In situ measurements of water transfer due to different mechanisms in a proton exchange membrane fuel cell. J Power Sources 2008;183:240-6.

[41] Jinnouchi R, Yamada H, Morimoto Y. Measurement of electro-osmotic drag coefficient of Nafion using a concentration cell. 14th International Conference on the Properties of Steam in Kyoto 2004;32:403-406.

[42] Olesen AC; Berning T, Kaer SK. On the diffusion coefficient of water in poylmer electrolyte membranes. ECS Transactions 2012;50(2):979-91.

[43] Motupally S, Becker AJ, Weidner JW. Diffusion of water through Nafion 115 membranes. J Electrochem Soc 2000;147:3171-7.

[44] Hussaini IS, Wang CY. Visualization and quantification of cathode channel flooding in PEM fuel cells. J Power Sources 2009;187:444-51.

[45] Perrin JC, Lyonnard S, Guillermo A, Levitz P. Water dynamics in ionomer membranes by field-cycling NMR relaxometry. Magnetic Resonance Imaging 2007;25:501-04.

[46] Mosdale R, Gebel G, Pineri M. Water profile determination in a running proton exchange membrane fuel cell using small-angle neutron scattering. J Membrane Science 1996;118:269-77.

[47] Turhan A, Kim S, Hatzell M, Mench MM. Impact of channel wall hydrophobicity on through-plane water distribution and flooding behavior in a polymer electrolyte fuel cell. Electrochimica Acta 2010;55:2734-45.

[48] Gurau V, Liu HT, Kakac S. Two-dimensional model for proton exchange membrane fuel cells. AIChE J. 1998;44:2410-22.

[49] Shimpalee S, Greenway S, Spuckler D, Van Zee JW. Predicting water and current distributions in a commercial-size PEM fuel cell. J Power Sources 2004;135:79-87.

[50] Berning T, Djilali N.Three-dimensional computational analysis of transport phenomena in a PEM fuel cell – a parametric study. J Power Sources 2003;124:440-52.

[51] Lum KW, McGuirk JJ. Three-dimensional model of a complete polymer electrolyte membrane fuel cell – model formulation, validation and parametric studies. J Power Sources 2005;143:103-24.

[52] Liu Z, Mao Z, Wang C, Zhuge W, Zhang Y. Numerical simulation of a mini PEM fuel cell stack. J Power Sources 2006;160:1111-21.

[53] Shimpalee S, Ohashi M, VanZee JW, Ziegler C, Stoeckmann C, Sadeler C, Hebling C. Experimental and numerical studies of portable PEM fuel cell stack. Electrochimica Acta 2009;54:2899-911.

[54] Macedo-Valencia J, Sierra JM, Figueroa-Ramirez SJ, Diaz SE, Meza M. 3D CFD modeling of a PEM fuel cell stack. J Hydrogen Energy 2016;41:23425-33.

[55] LaConti AB, Fragala AR, Boyack JR. Electrode materials and processes for energy conversion and storage. Electrochem Soc Proceedings Series, Princeton 1997; 77(6):354.

[56] Zawodzinski TA, Springer TE, Davey J, Jestel R, Lopez C, Valerio J, Gottesfeld S. A comparative-study of water-uptake by and transport through ionomeric fuel-cell membranes. J Electrochem Soc 1993;140(7):1981-85.

[57] Pivovar BS, Smyrl WH, Cussler EL. Nafion, Polystyrene sulfonic acid and polybenzimidazole as direct methanol fuel cell electrolytes. J Electrochem Soc 2005;152:A53-60.

[58] Xie G, Okada T. Water transport behavior in Nafion 117 membranes. J Electrochem Soc 1995;142(9):3057-62.

[59] Ren X, Henderson W, Gottesfeld S. Electro-osmotic drag of water in ionomeric membranes. J Electrochem Soc 1997;144:267-70.

[60] Ise M, Kreuer KD, Maier J. Aspects of the formation and mobility of ionic charge carriers and the stability of perovskite-type oxides. Solid State Ionics 1999;125(1):285-302.

[61] Fuller TF, Newman J. Experimental determination of the transport number of water in Nafion 117 membrane. J Electrochem Soc 1992;139:1332-37.

[62] Zawodzinski TA, Davey J, Valerio J, Gottesfeld S. The water content dependence of electro-osmotic drag in proton-conducting polymer electrolytes. Electrochim Acta 1995;40(3):297-02.

[63] Weng D, Wainright JS, Landau U, Savinell RF. Electro-osmotic drag coefficient of water and methanol in polymer electrolytes at elevated temperatures. J Electrochem Soc 1996;143(4):1260-63.

[64] Ye X, Wang CY. Measurement of water transport properties through membrane-electrode assemblies. J Electrochem Soc 2007;154(7):B676-82.

[65] Zelsmann HR, Pineri M, Thomas M, Escoubes M. Water self-diffusion coefficient determination in an ion exchange membrane by optical measurement. J Applied Polymer Sci 1990;41(7-8):1673-84.

[66] Gong X, Bandis A, Tao A, Meresi G, Wang Y, Inglefield PT, Jones AA, Wen WY. Self-diffusion of water, ethanol and decafluoropentane in perfluorosulfonate ionomer by pulse field gradient NMR. Polymer 2001;42:6485-92.

[67] Morris DR, Sun XD. Water sorption and transport properties of Nafion 117. J Appl Polym Sci 1993;50:1445-52

[68] Yeo SC, Eisenberg A. Physical properties and supermolecular structure of perfluorinated ion-containing (nafion) polymers. J Applied Polymer Sci 1997;21(4):875-98.

[69] Rivin D, Kendrick CE, Gibson PW, Schneider NS. Solubility and transport behavior of water and alcohols in Nafion. Polymer 2001;42(2):623-635.

[70] Ye X, LeVan MD. Water transport properties of Nafion membranes. J Membrane Sci 2003;221(1):163-173.

[71] Vishnyakov A, Ravikovich PI, Neimark AV. Characterization of micro-and mesoporosity in SBA-15 materials from adsorption data by the NLDFT method. J Phys Chem 2001;B105(29):6817-23.

[72] Arvay A. Proton exchange membrane fuel cell modeling and simulation using ANSYS Fluent. Arizona State University 2011, Master Thesis.

[73] Gasteiger H., Mathias M. Fundamental research and development chalenges in polymer electrolyte fuel cell technology, in: Materials for high temperature PEM fuel cells. The Energy Institute. Penn State University, USA 2003.

[74] Guerrero Moreno N., Cisneros Molina M., Gervasio D., Francisco Perez Robles J. Approach to polymer electrolyte membrane fuel cells (PEM fuel cells) and their cost. Renewable and Sustainable Energy Reviews. 2015;52:897-906.

[75] Nakagaki N. The newly developed components for the fuel cell vehicle, Mirai. SAE Technical Paper 2015;01:1174.

[76] Jian Q, Ma G, Qiu X. Influences of gas relative humidity on the temperature of membrane in PEM fuel cell with interdigitated flow field. Renewable Energy 2014;62:129-36.

[77] Ramya K, Sreenivas J, Dhathathereyan KS. Study of porous membrane humidification method in polymer electrolyte fuel cells. J Hydrogen Energy 2011;36(22):14866-72.

[78] Wan ZM, Wan JH, Liu J, Tu ZK, Pan M, Liu ZC, et al. Water recovery and air humidification by condensing the moisture in the outlet gas of a proton exchange membrane fuel cell stack. Appl Therm Eng 2012;42:173-78.

[79] Kong IM, Choi JW, Kim SI, Lee ES, Kim MS. Experimental study on the self-humidification effect in proton exchange membrane fuel cells containing double gas diffusion backing layer. Appl Energy 2015;145:345-53.

[80] Pei P, Chen H. Main factors affecting the lifetime of proton exchange membrane fuel cells in vehicle applications: a review. Appl Energy 2014;125:60-75.

[81] Kandlikar SG, Lu Z. Thermal management issues in a PEM fuel cell stack – a brief review of current status. Appl Therm Eng 2009;29(7):1276-80.

[82] Hosseinzadeh E, Rokni M, Rabbani A, Mortensen HH. Thermal and water management of low temperature proton exchange membrane fuel cells in fork-lift truck power system. Appl Energy 2013;104:434-44.

[83] Hwang SH, Kim MS. An experimental study on the cathode humidification and evaporative cooling of polymer electrolyte membrane fuel cells using direct water injection method at high current densities 2016;99:635-44.

[84] Dadda B, Abboudi S, Zarrit R, Ghezal A. Heat and mass transfer influence on potential variation in a PEM fuel cell membrane. J Hydrogen Energy 2014;39(27):15238-45.

[85] Chandan A, Hattenberger M, El-Kharouf A, Du S. Dhir A, Self V, et al. High temperature (HT) polymer electrolyte membrane fuel cells (PEM fuel cell) – a review. J Power Sources 2013;1:264-78.

[86] Markötter H, Manke I, Kuhn R, Arlt T, Kardjilov N, Hentschel MP, Kupsch A, Lange A, Hartnig C, Scholta J, Banhart J. Neutron tomographic investigations of water distributions in polymer electrolyte membrane fuel cell stacks. J Power Sources 2012;219:120-25.

[87] Tötzke C, Manke I, Hilger A, Choinka G, Kardjilov N, Arlt H, Markotter H, Schroder A, Wippermann K, Stolten D, Hartnig C, Kruger P, Kuhn R, Banhart J.Large area high resolution neutron imaging deterctor for fuel cell research. J Power Sources 2011;196:4631-37.

[88] Hussey DS, Jacobson DL, Arif M, Owejan JP, Gagliardo JJ, Trabold TA. Neutron imaging of the through-plane water distribution of an operating PEM fuel cell. J Power Sources 2007;172(1):225-28.

[89] Cho KT, Mench MM. Investigation of the role of micro-porous layer in polymer electrolyte fuel cells with hydrogen deuterium contrast neutron radiography. Phys Chem Cem Phys 2012;14:4296-02.

[90] Kätzel J, Markötter H, Artl T, Klages M, Haußmann J, Messerschmidt M, Kardjilov N, Scholta J, Banhart J, Manke I. Effect of ageing of gas diffusion layers on the water distribution in flow field channels of polymer electrolyte membrane fuel cells. J Power Sources 2016;301:386-91.

[91] Alrwashdeh SS, Markötter H, Haußmann J, Arlt T, Klages M, Scholta J, Banhart J, Manke I. Investigation of water transport dynamics in polymer electrolyte membrane fuel cells based on high porous micro porous layers. Energy 2016;102:161-65.

[92] Gößling S, Klages M, Haußmann J, Beckhaus P, Messerschmidt M, Arlt T, Kardjilov N, Manke I, Scholta J, Heinyel A. Analysis of liquid water formation in poylmer electrolyte membrane (PEM) fuel cell flow fields with a dry cathode supply. J Power Sources 2016;306:658-65.

[93] Bellows RJ, Lin MY, Arif M, Thompson AK, Jacobson D. Neutron imaging techniques for in situ measurement of water transport gradients within Nafion in polymer electrolyte membrane fuel cells. J Electrochem Soc 1999;146:1099-03.

[94] Hickner MA, Siegel NP, Chen KS, Hussey DS, Jacobson DL, Arif M. J Electrochem Soc 2008;155:B427-34.

[95] Scholz H. Modellierung und Untersuchung des Wärme- und Stofftransports und von Flutungsphänomenen. PhD Thesis. 2015.

[96] Wu H, Li X, Berg P. On the modeling of water transport in polymer electrolyte membrane fuel cells. Electrochimica Acta 2009;54(27):6913-27.

CURRICULUM VITAE

Željko Penga

Željko Penga, born April 7th 1989. in Split, Croatia, graduated Mechanical Engineering, Process and Construction Engineering on Faculty of Mechanical Engineering, Mechanical Engineering and Naval Architecture (FESB), University of Split, Croatia in 2013.

Immediately after the graduation he has enrolled in the Postraduate School of Mechanical Engineering on FESB with the main focus on Computational Fluid Dynamics analysis and experimental verification of the developed models. Over the years Željko has carried out numerous numerical research studies ranging from turbulent and laminar fluid dynamics problems, two-way-coupled fluid-structure-interaction analysis, solidification an melting, hydroabrasion, cavitation, heat and mass transfer and electrochemistry modeling, for various international and national research projects and various industrial partners in Croatia, Germany and Austria.

Željko has so far conducted research on 3 highly regarded international reasearch institutions during his carrer regarding the Computational Fluid Dynamics analysis: IVW in Kaiserslautern, and ZSW in Ulm, Germany and AVL LIST GMBH in Graz, Austria with high success rate and an ongoing cooperation with ZSW and AVL.

Željko is currently employed on FESB as Assisstant, he also works in parallel on international and national research projects dealing with PEM fuel cell diagnostics. He has so far published 2 original research articles and 10 conference papers during his Postgraduate Studies.